TEL AVIV UNIVERSITY
אוניברסיטת תל-אביב
RAYMOND AND BEVERLY SACKLER
FACULTY OF EXACT SCIENCES
SCHOOL OF PHYSICS & ASTRONOMY
הפקולטה למדעים מדוייקים
ע"ש ריימונד ובברלי סאקלר
בית הספר לפיסיקה ואסטרונומיה

# Study of short-range correlation in nuclei via measurement of the $^4$He(*e,e'pp*) and $^4$He(*e,e'pn*) reactions

Thesis submitted towards the degree of
Doctor of Philosophy

By
Igor Korover

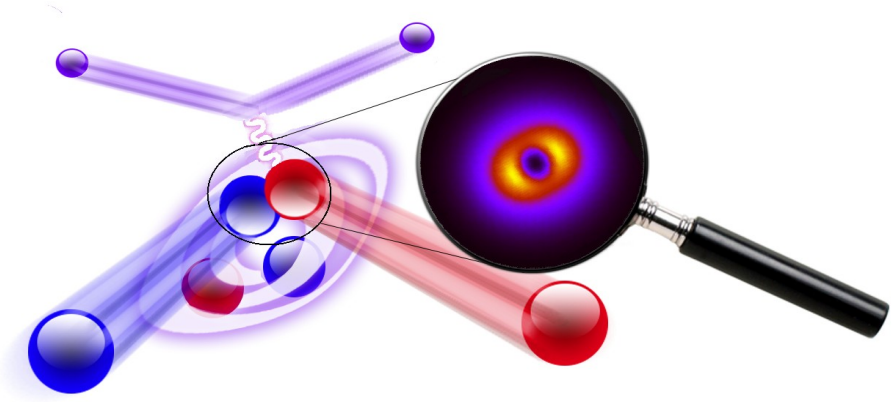

Submitted to the senate of Tel-Aviv University
April 2015

This work was carried under the supervision of
**Professor Eli Piasetzky**

*“Per aspera ad astra.”*

# Acknowledgment

I want to thank the many people who assisted in making this work possible and helped pave the way towards this enlightening achievement.

First and foremost, I want to thank my advisor, Prof. Eli Piasetzky, that gave me a great opportunity to enter this exciting field of nuclear physics. During this journey, I tried to absorb as much knowledge, enthusiasm, and experience from Eli. I value his attitude and patience with his students. His dedication to us shined in his ability to always share his wisdom and his time.

I wish to thank Douglas Higinbotham for his hospitality at Jefferson Laboratory, and for his help during the experiment and analysis. I want to thank our collaborators, Shalev Gilad and John Watson that also helped guide this research with their critical thinking and valuable input.

Furthermore, I want to thank the many wonderful people that I had the pleasure working with and learning from: Ran Shneor, Steve Wood, Brad Sawatzky, Vince Sulkosky, Peter Monaghan.

Special thanks to my family, for their love and encouragement. I would like to thank my parents that raised me with love for science and enthusiasm for knowledge. I wish that my father was here to see my graduation and experience this monumental achievement with me.

Finally, I owe an enourmous thanks to my beloved wife. I would have been lost without her love and support. I am grateful for her patience during my countless hours of work. Thank you, my dearly beloved.

**Abstract**

Describing nuclear forces, particularly the nucleon-nucleon ($NN$) interaction, is a continuing endeavor. In 1953, Hans A. Bethe stated that it was probably the most investigated physical problem in the history of mankind. Nevertheless, even today this topic presents a formidable challenge. Maybe the most mysterious part of the $NN$ force is the very strong repulsion at short distances. There are no measurements that are sensitive to the details of the short range interaction, which can also constrain the various phenomenological potentials. The recent progress in Lattice QCD still cannot supply precise quantitative predictions.

A two-nucleon short-range correlated pair ($2N$-SRC) is two nucleons in the nuclear ground state with large relative momentum and a small center-of-mass (CM) momentum, where large and small are relative to the Fermi momentum of the nucleus. In the missing-momentum range of 300–600 MeV/c, these pairs were found to dominate the high-momentum tails of the nuclear wave functions, with neutron-proton ($np$) pairs nearly 20 times more prevalent than proton-proton ($pp$) pairs, and by inference neutron-neutron ($nn$) pairs. This is due to the dominance of the $NN$ tensor interaction at the probed distances. The association of $2N$-SRC with missing momenta of 300–600 MeV/c, with dominance of the $NN$ tensor force, leads naturally to the quest for increasing missing momenta. This allows us to look for pairs that are even closer to each other at distances in which the nuclear force changes from being predominantly tensor to the essentially unexplored repulsive.

This thesis reports on a simultaneous measurement of the $^4$He$(e,e'p)$, $^4$He$(e,e'pp)$, and $^4$He$(e,e'pn)$ reactions at $Q^2 \approx 2$ (GeV/c)$^2$ and $x_B > 1$, for an $(e,e'p)$ missing-momentum range of 400 to 830 MeV/c. The knocked-out proton was detected in coincidence with a proton or neutron recoiling almost back to back to the missing momentum, leaving the residual $A = 2$ system at low excitation energy. These data were used to identify two-nucleon short-range correlated pairs and to deduce their isospin structure as a function of missing momentum, in a region where the $NN$ force is expected to change from predominantly tensor to repulsive. We found that the abundance of neutron-proton pairs is reduced as the nucleon momentum increases beyond $\sim 500$ MeV/c. The extracted fraction of proton-proton pairs is small and almost independent of the missing momentum. Our data are compared with calculations of two-nucleon momentum distributions in $^4$He and discussed in the context of probing the elusive repulsive component of the $NN$ force.

# Contents

**Contents** 1

**List of Figures** 3

**List of Tables** 11

**1 Scientific Background** 14
- 1.1 Introduction . . . 14
- 1.2 Terminology . . . 16
  - 1.2.1 2N – SRC . . . 16
  - 1.2.2 High momentum tail . . . 16
  - 1.2.3 Scaling . . . 17
  - 1.2.4 Quasi-Elastic Scattering (QE) . . . 18
  - 1.2.5 The Plane Wave Impulse Approximation (PWIA) . . . 19
  - 1.2.6 Final State Interactions (FSI) . . . 20
  - 1.2.7 Competing processes . . . 21
- 1.3 Inclusive Measurements . . . 22
- 1.4 Semi inclusive measurements . . . 25
- 1.5 Triple coincidence measurements . . . 28
- 1.6 Dominance of the tensor force . . . 31
- 1.7 New Experiment on $^4$He . . . 33

**2 Experimental setup** 35
- 2.1 The accelerator and the experimental hall . . . 35
  - 2.1.1 Experimental Hall A – CEBAF . . . 36
  - 2.1.2 Beam line . . . 36
  - 2.1.3 Target . . . 37
- 2.2 High Resolution Spectrometers . . . 39
  - 2.2.1 Vertical Drift Chambers (VDCs) . . . 41
  - 2.2.2 Scintillators . . . 41
  - 2.2.3 Pion Rejector . . . 42
  - 2.2.4 Gas Cherenkov . . . 42
- 2.3 The BigBite Spectrometer . . . 42
  - 2.3.1 MWDC . . . 43
  - 2.3.2 Trigger Plane . . . 44
- 2.4 The Neutron Detector . . . 46
- 2.5 The Data Acquisition System (DAQ) and the off-line analysis. . . . 47
- 2.6 Selecting events by the trigger setup. . . . 47
- 2.7 Kinematics . . . 49

**3 Data Analysis** **51**
3.1 Data Analysis . . . 51
3.2 HRSs . . . 51
3.2.1 TDCs . . . 51
3.2.2 VDCs, optics, and momentum reconstruction. . . . 53
3.3 BigBite . . . 56
3.3.1 ADC/QDC . . . 56
3.3.2 TDC . . . 57
3.3.3 Wire Chambers . . . 58
3.3.4 Momentum / optics . . . 59
3.3.5 Proton ID . . . 60
3.3.6 Multi hits and hits matching . . . 61
3.3.7 The proton detection efficiency in BigBite . . . 63
3.4 HAND . . . 65
3.4.1 ADC calibration and threshold determination . . . 65
3.4.2 TOF calibration. . . . 68
3.4.3 Time Walk correction . . . 69
3.4.4 Position Calibration. . . . 71
3.4.5 Neutron ID . . . 72
3.4.6 Neutron Detection Efficiency . . . 74
3.4.7 Absolute timing and momentum calibration . . . 78
3.4.8 Neutron Momentum reconstruction . . . 82
3.4.9 Event Mixing / background . . . 83

**4 Results** **86**
4.1 $^4$He$(e,e'p)$ Event selection . . . 86
4.2 The semi-inclusive $(e,e'p)$ reaction. . . . 89
4.3 $^4$He$(e,e'pn)$ Triple coincidence events. . . . 94
4.4 CM motion of the pairs . . . 95
4.5 Opening angle . . . 99
4.6 Missing mass . . . 100
4.7 Triple coincidence events $^4$He$(e,e'pp)$ . . . 102
4.8 Triple to double ratios $^4$He$(e,e'pN)$ to $^4$He$(e,e'p)$ . . . 104
4.9 Triple to triple ratio $^4$He$(e,e'pp)/^4$He$(e,e'pn)$ . . . 107
4.10 Experimental Uncertainties . . . 109

**5 Summary and conclusion** **112**

**Appendix** **115**
Appendix A . . . 115
Appendix B . . . 117

**Bibliography** **121**

# List of Figures


1.1 The spectroscopic strength for protons knocked out of well defined shells versus the target mass (A). The red line represents the IPSM prediction. . . . . 15
1.2 Calculation of momentum distribution in $^{12}$C with correlations (solid line) and without correlations (doted line). See Ref [18] for details. . . . . 17
1.3 Momentum distributions for different nuclei compared to the deuteron Ref. [18]. . . . . 18
1.4 Schematic presentation of cross-section for (a) electron-nucleon and (b) electron-nucleus scattering versus the energy transfer in the reaction. . . . . 19
1.5 Feynman diagram presenting a QE A$(e,e'p)$A-1 reaction in a PWIA approximation. . 20
1.6 Diagrams showing FSI. (a) Between the nucleons in the $2N$-SRC, (b) between the knocked-out nucleon and the A-2 system. . . . . 21
1.7 Feynman diagrams for competing processes: left (MEC), right (IC). . . . . 21
1.8 The minimum recoil momentum as a function of $x_B$. Top panel: For deuterium at several $Q^2$, Bottom panel: For different nuclei at $Q^2 = 2$ (GeV/c)$^2$. Horizontal lines represent an example of minimal momentum of 300 MeV/c. This figure was adapted from Ref [6]. . . . . 22
1.9 SRC model predictions for the normalized inclusive cross section ratio as a function of $x_B$ for several values of $Q^2$. a) for $^{12}$C/$^3$He b) for $^{56}$Fe/$^3$He. . . . . 23
1.10 Inclusive cross section ratios,$^{56}$Fe over deuteron at different $Q^2$ values [5]. The solid lines are calculations of Ref [29]. . . . . 24
1.11 Inclusive cross section ratios of a) $^{12}$C/$^3$He, and b) $^{56}$Fe/$^3$He as a function of $x_B$ for $Q^2 > 1.5$ (GeV/c)$^2$ [7]. Curves are SRC model predictions for different $Q^2$ in the range 1.4 GeV$^2$ (curve 1) to 2.6 GeV$^2$ (curve 4). . . . . 24
1.12 Inclusive cross section ratios of recent inclusive measurements from JLab [8]. . . . . 25
1.13 Cross-section for the $^3$He$(e,e'p)pn$ reaction versus missing energy $E_m$. The vertical arrow gives the peak position expected for disintegration of correlated pairs (except for highest energy, where the prediction fails). The dotted curve presents a PWIA calculation using Salme's spectral function and $\sigma_{cc1}$ electron-proton off shell cross-section. Other curves are recent theoretical predictions of Laget [38]: PWIA (dash dotted line), PWIA + FSI (long dashed line), full calculation (solid line) including meson-exchange current and final-state interactions. In the 620 MeV/c panel, the additional short-dashed curve is a calculation with PWIA + FSI only within the correlated pair. This Figure is reproduced from Ref. [9]. . . . . 28
1.14 The cosine of the opening angle between the struck proton in the quasi-elastic $^{12}$C$(p,2p)$ reaction and the recoil neutron. Data labeled by 94 and 98 are from [11,12] respectively. The vertical line corresponds $p_n = 275$ MeV/c. . . . . 29

1.15 The fractions of correlated pair combinations in carbon as obtained from the $^{12}$C$(e,e'pp)$ and $^{12}$C$(e,e'pn)$ reactions at JLab (E01-015) [14,15] as well as from previous, $^{12}$C$(p,2pn)$ data from BNL [11–13]. . . . . 30
1.16 Ratio of $pp$ to $pn$ spectator pair cross sections, integrated over $0.3 < p_{rel} < 0.5$ GeV/c. The points show the data, the solid histogram shows the Golak one-body calculation [49], and the dashed histogram shows the ratio of the Golak $pp$ and $pn$ bound state momentum distributions. The dotted line at 0.5 shows the simple-minded pair counting result. The data and the one-body calculation have been multiplied by 1.5 to approximately account for the ratio of the average $ep$ and $en$ elementary cross section. . . . . 31
1.17 The momentum distribution ($\rho_{NN}$) for $np$ (lines) and $pp$ (symbols) pairs in various nuclei as a function of the relative momentum of the nucleons in the pair ($q_{\rm rel}$) from Ref. [50]. The calculations assume pairs at rest ($Q_{\rm CM} = 0$). . . . . 32
1.18 The main figure shows the central part of nucleon-nucleon potential. The insert present the tensor part of the potential. The potential is taken from AV18 [50]. Its clearly seen that generally a much weaker tensor part, becomes dominant in the region probed by the E01-015 experiment ($300 - 600$ MeV/c). . . . . 33
1.19 The density distribution for $np$ (red) and $pp$ (blue) pairs in $^3$He. The figure shows the $pp/np$ ratio with/without three nucleon forces (dashed/solid lines) included for V18 (red) and Bonne (blue) potentials. Figure adapted from [51]. . . . . 34

2.1 Schematic layout of JLab accelerator site (before the 12 GeV upgrade). . . . . 35
2.2 Schematic layout of the experimental hall A showing the approximate location of the detectors and indicating various beam line diagnostic instrumentation. . . . . 36
2.3 Picture of scattering chamber. In the center of the chamber various targets on the ladder are seen. See text for details. . . . . 37
2.4 Schematic view of the target ladder used for the production runs. . . . . 39
2.5 Schematic layout of the HRS spectrometer, showing the geometrical configuration of the three quadrupole and the dipole magnets. Also shown is the location of the detector hut. Dimensions are given in meters. . . . . 40
2.6 Side view of the detector stacks in each spectrometer. The left / right sketch shows the detectors in the left / right HRS. In this experiment the left HRS was used to detect electrons and the right HRS detected protons. . . . . 41
2.7 Schematic layout of the Hall A VDCs. Left: the orientation of the wires planes relative to the central ray is shown. Right: side view of the VDC is presented. . . . . 41
2.8 Layout of lead glass blocks of the pion rejector. . . . . 42
2.9 The BigBite spectrometer. Shown are the Detectors package and the magnet. In front of the BigBite magnet is shown a sieve slit collimator that can be lowered for calibration purposes. . . . . 43
2.10 On the left side a schematic view of BigBite's first MWDC, size of active area, orientations of the wires, and the read out electronics are shown. A particle tracking through the MWDC is shown on the right. . . . . 44
2.11 A 3D rendering of the trigger plane, showing the $\Delta$E and E planes. Each scintillator bar in both planes has two PMTs attached, one at each end. . . . . 45
2.12 A schematic view of the trigger plane scintillators E (top) and $\Delta$E (bottom) plane. The side and lateral view of the trigger plane are shown below. . . . . 45

2.13 Schematic side view of HAND. The scintillators of different sized are shown with different colors. . . . 46
2.14 Front view of the veto bars and their arrangement. These are the detectors marked as "V" in Figure 2.13. . . . 47
2.15 The electronic layout for the formation of the single L-HRSs trigger T3. Similar logic is applied for R-HRS. . . . 48
2.16 Electronic layout for BigBite spectrometer. The trigger is generated using the E plane bars. . . . 49
2.17 Electronic layout for each bar in HAND spectrometer. . . . 49
2.18 A diagram of the layout of the experiment. The electron kinematics were fixed and the proton angle and momentum were varied. In the background, the various detectors with their magnets and their main systems are shown. . . . 50

3.1 TOF of electrons between s1 and s2m in L-HRS corrected for the path length. The TOF shown is before the TDCs offset calibration. . . . 52
3.2 TOF between s1 and s2m planes after the TDCs calibration. . . . 52
3.3 The resolution of the TOF after the calibration. . . . 53
3.4 The reconstructed position of the 13 thin Carbon foils of the optical target. The expected position of each foil is marked by a red triangle. . . . 53
3.5 Example of reconstruction with a sieve slit in the L-HRS. The intersections of the red lines represent the expected positions as measured by the survey group. . . . 54
3.6 Reconstruction of the in-plane scattering angle versus electron momentum for elastic scattering events. The gap between the two strips is due to the momentum coverage of the HRS settings. . . . 55
3.7 A typical TOF (time-of-flight between s1 and s2m planes corrected to proton mass and path length) distribution in R-HRS as obtained during the calibration runs. . . . 55
3.8 Number of reconstructed tracks in LHRS after applying all $(e, e'p)$ cuts (see chapter 4.2 for details). . . . 56
3.9 Energy deposit in $\Delta$E plane vs E plane. Protons are clearly identified by their energy deposit. With the increase of the protons momenta the energy deposited in $\Delta$E plane decrease while the energy deposit in E plane is increase up to the punch through point, point were protons have enough energy to penetrate both planes. For protons with higher energy deposit in both plane gradually decrease with the increase of the protons momentum. . . . 57
3.10 Reconstructed position distribution of charged particles in an E plane bar (left) and TOF of elastic protons (right) after the TDC calibration. . . . 58
3.11 A typical distribution of the drift time. . . . 58
3.12 Photograph of the BigBite magnet, taken from its back side (left) and the simulated magnetic field of BigBite in the mid-plane of the magnet (Right). . . . 59
3.13 Reconstructed momentum in BigBite vs expected momentum (elastic scattering on Hydrogen). . . . 60
3.14 The difference between the momentum transfer in H$(e, e'p)$ and the measured momentum in BigBite. Momentum resolution determined by elastic scattering with protons having momentum of 450 MeV/c (left) and 650 MeV/c (right). . . . 60

3.15 Energy deposited in the E counters vs reconstructed momentum in BigBite. Below the horizontal dashed line minimum ionizing particles and bad momentum reconstructed tracks are located. . . . 61
3.16 Number of E counter hits per event during the elastic scattering run. . . . 61
3.17 Number of hits per event in each E counter. . . . 62
3.18 Difference between hit position on the E plane as reconstructed based on the MWDC and as reconstructed based on the E plane information. The left figure is for the dispersive direction and the right figure is along the scintillator bar. . . . 62
3.19 Number of reconstructed tracks with a matching hit in the E plane (data is from the 750 GeV/c settings). . . . 63
3.20 Background subtracted TOF distributions for protons in BigBite. Left figure represents TOF with track in the MWDC and right figure represent the TOF without requesting a track in the MWDC. . . . 64
3.21 Proton detection efficiency of the MWDC during the production period. The run period was divided into groups of 20-25 runs (presented in chronological order). . . . 64
3.22 Pedestal distribution of HAND's first layer scintillators. Left: before pedestal alignment, Right: after. . . . 65
3.23 ADC distributions for elastic protons in layer 1 (left) and in the fourth layer (right). Shift in the ADC peak position is clearly seen in agreement with the expected value. . 66
3.24 Hardware threshold. Ratio between number of events with TDC requirement to total number of events, plotted vs ADC channel number. . . . 67
3.25 Example of the hardware thresholds values for the scintillator bars in the second layer. Red points represent the left side PMTs and black represent right side. . . . 67
3.26 TOF distribution of a single bar from layer 5. . . . 69
3.27 Dependence of the TOF on the energy deposition in the scintillator. . . . 70
3.28 TOF distributions for elastic protons. Left side for single bar (same as for Figure 3.26) and Right side all bars combined. . . . 70
3.29 Difference between measured TOF and expected TOF for neutrons in HAND. Data is from the d$(e, e'pn)$ reaction. The impact of the pulse height correction, an increase in the signal to background ratio due to a narrower peak. Red line before time walk correction and black after. . . . 71
3.30 Position distributions for different bars. Red histogram represent the simulation. . . . 72
3.31 Example of blocking bars algorithm. Horizontal red line represent the center of the detector aligned with the target center. Rays pointing from the target to extreme corner of the scintillator bar are marked in green. These rays define the maximal and minimal angles in which the investigated bar can be seen from the target. Based on these angles blocking bars that are in line of sight between the target and the investigated bar are defined. . . . 73
3.32 Number of multiple neutrons per event at the 500 MeV/c kinematics. . . . 74
3.33 Number of multiple neutrons per event at the 750 MeV/c kinematics. . . . 74
3.34 Missing mass for d$(e, e'p)$ channel during the LD2 measurements. . . . 75
3.35 Corrected TOF spectra for low (left) and high (right) settings for the HAND efficiency measurements. . . . 76

3.36 The in-plane angle based on the reconstructed neutron in HAND versus the recoil angle based on the HRSs reconstruction (d$(e, e'pn)$ exclusive scattering). . . . . 76
3.37 The out-of-plane angle based on the reconstructed neutron in HAND and the recoil angle based on the HRSs reconstruction (LD2 exclusive scattering). . . . . 77
3.38 The absolute neutron detection efficiency. . . . . 77
3.39 Normalized background level versus run number. Runs from 500 MeV/c are on the left and runs from 750 MeV/c setting are on the right side. The arrows represent the change between different kinematical settings. The runs within the average ±20% are taken for the analysis. These data already exclude corrupted runs, such as with no signal. . . . . 78
3.40 The TOF distribution measured in HAND from Deuterium target. The red circle marks the gamma peak and the blue represents recoil neutrons. . . . . 79
3.41 Difference between measured and expected TOF of neutrons for scattering from deuterium target after changing to $x_B > 1$ kinematics. This measurement used for absolute time determination for HAND. . . . . 80
3.42 Absolute TOF spectra measured in HAND in respect to reaction time. The gamma peak identified for the three production kinematics. Top plane is for 500 MeV/c settings, middle for 625 MeV/c and bottom for 750 MeV/c. The peak positions with their uncertainties are shown near the peaks. . . . . 81
3.43 Gamma peak position in [ns/meter] vs. run number. The arrows represent the change between different kinematical settings. . . . . 82
3.44 The neutron momentum reconstructed from TOF vs. the expected momentum based on the HRSs (left). The difference between $p_{\text{miss}}$ and reconstructed neutron momentum, $\Delta p$ (right). Scattering is from a liquid Deuterium target. . . . . 82
3.45 Simulated TOF distribution in HAND. Background (red dashed line), SRC recoil neutrons generated using $(e, e'p)$ data for 750 MeV/c (blue dashed line) and the combine distribution (black line). . . . . 84
3.46 Distribution of the simulated CM of the pair in the $y$ direction in Lab coordinate system ($y$ direction is almost aligned with the direction of the detected particle in HAND). Black histogram – pure neutrons signal simulated based on the $(e, e'p)$ events from 750 MeV/c kinematics, Red – pure BG distribution, Blue – mixed events. See text for more details. 85

4.1 In plane angle vs out of plane angle for R-HRS. Acceptance are marked with the black lines. . . . . 86
4.2 Momentum acceptance of the R-HRS. Vertical lines represent the applied cuts (identical to the nominal acceptance cut). Similar cuts were applied to the L-HRS. . . . . 87
4.3 Coincidence time after the correction between HRSs. Left figure results from scattering from a Deuterium target and right figure is coincidence time for the 750 MeV/c $^4$He production data (no additional cut applied). The 2 ns beam structure is clearly seen in both figures. . . . . 87
4.4 Vertex reconstruction based on the L-HRS. Target walls are identified and a software cut removed their contribution. . . . . 88
4.5 The difference between the vertex reconstructed by the L-HRS and the R-HRS. The cut shown was used to remove random background. . . . . 88

4.6 Beta distribution for 750 MeV/c. Left figure show the spectrum before the cuts on coincidence time and vertex were applied. Right figure show the events after the cuts were applied. . . . 89
4.7 A plot of energy transfer versus the $y$ scaling variable. Example from 500 MeV/c, a cut that separates the nucleon and the possible $\Delta$ regions. Positive values of $y$ scaling corresponds to $x_B < 1$, where the $\Delta$ production is not suppressed. . . . 90
4.8 $(e, e'p)$ Missing energy distribution for 500 MeV/c. Red distribution represents the events with $\omega - y$ cut. Dashed line represents all events. . . . 90
4.9 Same as Figure 4.8 for 625 MeV/c. . . . 91
4.10 Same as Figure 4.8 for 750 MeV/c. . . . 91
4.11 Number of events versus $x_B$. The histograms shows the distributions with/without (Red/Black) cut on $\omega - y$. The $\omega - y$ cut is as shown in Figure 4.7. . . . 92
4.12 $Q^2$distribution. Red/Black with/without cut on $\omega - y$ as shown in Figure 4.7. . . . 92
4.13 $(e, e'p)$ Missing mass distribution. Dashed line represent all $(e, e'p)$ events. Red are events coming from the $(e, e'p)$ region in the $\omega - y$ scaling plane. Blue is from the excluded region in the $\omega - y$ plane. . . . 93
4.14 Missing momentum distribution for three kinematical setups of the experiment. Total number of $(e, e'p)$ event for each kinematics are presented with the cuts listed below. . 93
4.15 TOF distribution and reconstructed background subtracted momentum distribution for neutrons at 500 MeV/c. . . . 94
4.16 Same as Figure 4.15 for 625 MeV/c. . . . 94
4.17 Same as Figure 4.15 for 750 MeV/c. . . . 94
4.18 Two examples how a high momentum nucleon can be produced. (a) High relative momentum (b) Lower relative momentum (black arrow) plus contribution from CM momentum (red arrow). . . . 96
4.19 The number of events as a function of the $x$, $y$ and $z$ components of $\vec{p}_{\rm cm}$ distributions. $x$ and $y$ directions (top left and right respectively) are orthogonal directions to $\vec{p}_{\rm miss}$ and $z$ (bottom) along $\vec{p}_{\rm miss}$. The distributions shown here are for the 750 MeV/c kinematics. 96
4.20 The measured width as a function of simulated width in the $y$ direction. The horizontal lines show the measured width of the $\vec{p}_{cm}$ distribution with its uncertainty band, $\pm\sigma$, (see text below for details). The solid curve corresponds to the simulation without applying the cut on the TOF. The different colors and shapes of the points are explained in the text below. . . . 97
4.21 Same as Figure 4.20 but for the $x$ direction. . . . 97
4.22 Same as Figure 4.20 for the $z$ direction (along $\vec{p}_{\rm miss}$). . . . 98
4.23 Different colors represent different spatial directions; Red points – $x$ direction. Blue points – $y$ direction. Green points – $z$ direction. Different symbols are for three kinematical setups; squares are for 500 MeV/c, circles for 625, and triangles for 750 MeV/c. 98
4.24 Opening angle distribution measured during the 625 MeV/c setting. Black histogram: signal and background. Blue histogram: opening angle for events in the off coincidence time region. Red: opening angle for events obtained using event mixing. . . . 99
4.25 Opening angle for 625 and 750 MeV/c setups. Red line represent the random background from mixed events. Solid line is the opening angle based on the simulation with $\sigma = 100$ MeV/c in each direction with a mixture of flat random background. . . . 100

4.26 Missing mass distribution for $^4$He$(e,e'pn)$ reaction at 500 MeV/c. . . . . 101
4.27 Same as Figure 4.26 for 625 MeV/c. . . . . 101
4.28 Same as Figure 4.26 for 750 MeV/c. . . . . 102
4.29 $(e,e'pn)$ missing mass versus $(e,e'p)$ missing mass for 750 MeV/c kinematics. Vertical red line represents the cut on $(e,e'p)$ missing mass in order to suppress the pion production channel in the triple coincidence events. . . . . 102
4.30 Energy deposit vs momentum in BigBite. Black circles are events that also pass the cut under the TOF peak. . . . . 103
4.31 Difference between expected TOF and measured for protons in BigBite. Correction is made by assuming that the particle has a proton mass. . . . . 103
4.32 Missing mass for the $^4$He$(e,e'pp)$ reaction for $p_{\rm miss}$ 625 and 750 MeV/c. . . . . 104
4.33 $(e,e'pN)$ to $(e,e'p)$ Correction factor as a function of $p_{\rm miss}$ [MeV/c], assuming CM momentum with widths of 90, 100 and 110 MeV/c. The correction factors are summarized in Table 4.3. . . . . 105
4.34 $^4$He$(e,e'pn)/^4$He$(e,e'p)$ ratio as function of missing momentum. The horizontal error bars indicate the acceptance range. The shaded area represents the ratio corrected for transparency and single charge exchange (see details on these calculations in appendix B). . . . . 106
4.35 ($^4$He$(e,e'pp)/2)/^4$He$(e,e'p)$ ratio as function of missing momentum (see text about the factor 2). The shaded area represents the ratio corrected for transparency and single charge exchange (see calculation in appendix B). . . . . 107
4.36 ($^4$He$(e,e'pp)/2)/^4$He$(e,e'pn)$ ratio as function of missing momentum (see text about the factor 2). The shaded area represents the ratio corrected for transparency and single charge exchange (appendix B). Lines represent theoretical predictions of the ratio, see text. . . . . 108
4.37 Simulated CM momentum distribution. . . . . 109
4.38 The $\omega$ versus $y$ scaling parameter cut (solid line). The dashed diagonal lines represent the sensitivity test for this cut. The data is for the 750 MeV/c kinematics. . . . . 110
4.39 BigBite acceptance for in-plane scattering angle $\theta$ versus the momentum of the detected particle. Horizontal red lines represent the angular cuts that were used, while the vertical represent the minimum and maximum possible momentum. The missing area correspond to less than 1.5% for the 500 MeV/c settings. For 625 and 750 MeV/c kinematics we did not expect events lost from this region due to the small acceptance of the HRSs. To be conservative we estimated BB acceptance uncertainties of 1.5% for all setups. . . . . 111

5.1 Bottom panel: The measured ratios $^4$He$(e,e'pp)/^4$He$(e,e'pn)$, shown as solid symbols, as a function of the $^4$He$(e,e'p)$ missing momentum. Each point is the result of a different setting of the detectors. The bands represent the data corrected for FSI to obtain the pair ratios, see text for details. Also shown are calculations using the momentum distribution of Ref. [68] for pairs with weighted-average CM momentum assuming arbitrary angles between the CM and the relative momenta in the pair (solid black line). The middle panel shows the measured $^4$He$(e,e'pp)/^4$He$(e,e'p)$ and extracted $\#pp/\#p$ ratios. The top panel shows the measured $^4$He$(e,e'pn)/^4$He$(e,e'p)$ and extracted $\#pn/\#p$ ratios. The unphysical region above 100% obtained due to systematic uncertainties and statistical fluctuations is marked by white strips. Ratios for $^{12}$C are shown as empty symbols with dashed bars. The empty star in the top panel is the BNL result [13] for $^{12}$C$(p,ppn)/^{12}$C$(p,pp)$. . . . . 113

A.1 Retiming circuit diagram for BigBite. The original L1A signal (top line) is retimed by the signal from the E plane bars generate retimed L1A'. If there was no signal in the E plane, the delayed L1A serves as fail safe that make the retimed L1A to be a delayed L1A (this is needed to clear the front end electronics). . . . . 115

A.2 Recorded retimed T3 signal (arbitrary channels). Two sharps peaks on both ends of the distribution represent cases without T3 signal (right peak) and when the retiming is done on L1A (left peak). . . . . 116

B.1 Corrected ratios for $(e,e'pp)/(e,e'pn)$. From top to bottom: 500, 625 and 750 MeV/c settings. . . . . 119

B.2 Corrected ratios for $(e,e'pp)/(e,e'p)$ on the left side and $(e,e'pn)/(e,e'p)$ on the right. From top to bottom: 500, 625 and 750 MeV/c settings. . . . . 120

# List of Tables


2.1 General characteristics of HRSs . . . . . 40
2.2 Main characteristics of the BigBite spectrometer . . . . . 43

3.1 Energy loss in HAND counters . . . . . 66
3.2 Absolute time measurement kinematics. . . . . 78

4.1 Number of triple coincidence $^4$He$(e, e'pn)$ events. . . . . 95
4.2 Number of triple $^4$He$(e, e'pp)$ coincidence events. . . . . 104
4.3 Acceptance correction factor for the $(e, e'pN)$ to $(e, e'p)$ ratio. . . . . 105
4.4 The number of events in all measured reaction channels. . . . . 105
4.5 The triple to double ratios. The uncertainties include statistical uncertainty and systematic uncertainty (see section 4.10). . . . . 106
4.6 Statistical uncertainties. . . . . 107
4.7 Summary of triple to triple ratios. . . . . 107
4.8 Summary of the systematic uncertainties in the experiment. Total systematic uncertainty for each ratio is presented. . . . . 111

B.1 Transparency values . . . . . 118
B.2 The $\#np/\#pp$ ratios. Measured and corrected . . . . . 118
B.3 $\#np/\#p$ $(p > p_{miss})$ Values in [%] . . . . . 119
B.4 $\#pp/\#p$ $(p > p_{\mathrm{miss}})$ Values in [%] . . . . . 119

# Nomenclature

| | |
|---|---|
| ADC | Analog to Digital Converter |
| BNL | Brookhaven National Laboratory |
| BNL | Brookhaven National Laboratory |
| CEBAF | Continuous Electron Beam Accelerating Facility |
| CM | Center of Mass |
| CODA | CEBAF online data acquisition |
| FASTBUS | a computer standard for high-speed, large-scale data acquisition. |
| FSI | Final State Interaction |
| FSI | Final State Interaction |
| HAND | Hall A Neutron Detector |
| HRS | High Resolution Spectrometer |
| IC | Isobar current / configuration |
| IPSM | Independent Particle Shell Model |
| IPSM | Independent Particle Shell Model |
| JLab | Thomas Jefferson Laboratory |
| LD2 | Liquid Deuterium |
| MAMI | Mainzer Mikrotron |
| MEC | Meson Exchange Current |
| MWDC | Multi Wire Drift Chamber |
| NIKHEF | National Institute for Nuclear Physics and High Energy Physics in Amsterdam |
| PMT | Photo Multiplier Tube |
| PWIA | Plane Wave Impulse Approximation |
| QE | Quasi-Elastic |
| QE | Quasi-Elastic |

| | |
|---|---|
| ROC | Read Out Control |
| ROOT | An object oriented framework for large scale data analysis |
| SCX | Single Charge Exchange |
| SLAC | Stanford Linear Accelerator Center |
| SRC | Short-Range Correlation |
| TDC | Time to Digital Converter |
| TOF | Time of Flight |
| VDC | Vertical Drift Chamber |
| VME | Virtual Machine Environment |

# Chapter 1

# Scientific Background

## 1.1 Introduction

The building blocks of nuclei are positively charged protons and neutral neutrons, collectively called nucleons. The discovery of the neutron was made by James Chadwick in 1932 [1] paving the way to the modern picture of the atomic nucleus and the underlying nucleon – nucleon interaction. The fact that we have stable nuclei means that the repulsive electromagnetic interaction is weaker than the nucleon-nucleon interaction, which is attractive at distances of a few fermi and repulsive at shorter distances. The most general non relativistic Hamiltonian for nuclei with $A$ nucleons assuming two nucleon interaction is given by:

$$H = T + \sum_{i<j=1}^{A} \nu(i,j) \tag{1.1}$$

where $T$ is the kinetic energy and $\nu(i,j)$ is the two body potential.

Even for the light nuclei, calculations of the two body potential present a formidable challenge. The general Hamiltonian can be simplified and rewritten by introducing a one body potential $V(i)$ mean field, in which the i-th nucleon is moving:

$$H = T + \sum_{i=1}^{A} V(i) + [\sum_{i<j=1}^{A} \nu(i,j) - \sum_{i=1}^{A} V(i)] \tag{1.2}$$

The equation can be divided into two parts, the independent particle shell model part:

$$H = T + \sum_{i=1}^{A} V(i) \tag{1.3}$$

and the residual interaction part:

$$V_{\text{res}}(i) = \sum_{i<j=1}^{A} \nu(i,j) - \sum_{i=1}^{A} V(i) \tag{1.4}$$

In the 1950s the standard nuclear model was the independent particle shell model (IPSM). In this model, each neutron and proton is moving independently in well defined quantum orbits in the attractive mean field created by all other $(A-1)$ nucleons. The quantum orbits (shells) are populated sequentially according to the Pauli Exclusion Principle that prevents identical fermions from occupying

the same single particle state. Nucleon transitions are allowed only to the non occupied shells. For the low level states in the odd-$A$ nuclei, IPSM gave reasonable agreement with the experimental data. The Nobel Prize in Physics in 1963 was given to M. Goeppert-Mayer, H. D. Jensen, and E. P. Wigner on their discoveries of the shell model [2].

Although there is a reasonable agreement between the IPSM and experimental data, it can not fully explain nuclei due to existence of correlations between the nucleons. Therefore, the results of proton removal experiments using electron beams of several hundred MeV completed during the 1980s and 1990s did not surprise anyone. These experiments showed that the yield of the protons knocked-out from well defined shells (Figure 1.1) are only $60-70\%$ of the strength predicted by the IPSM [26].

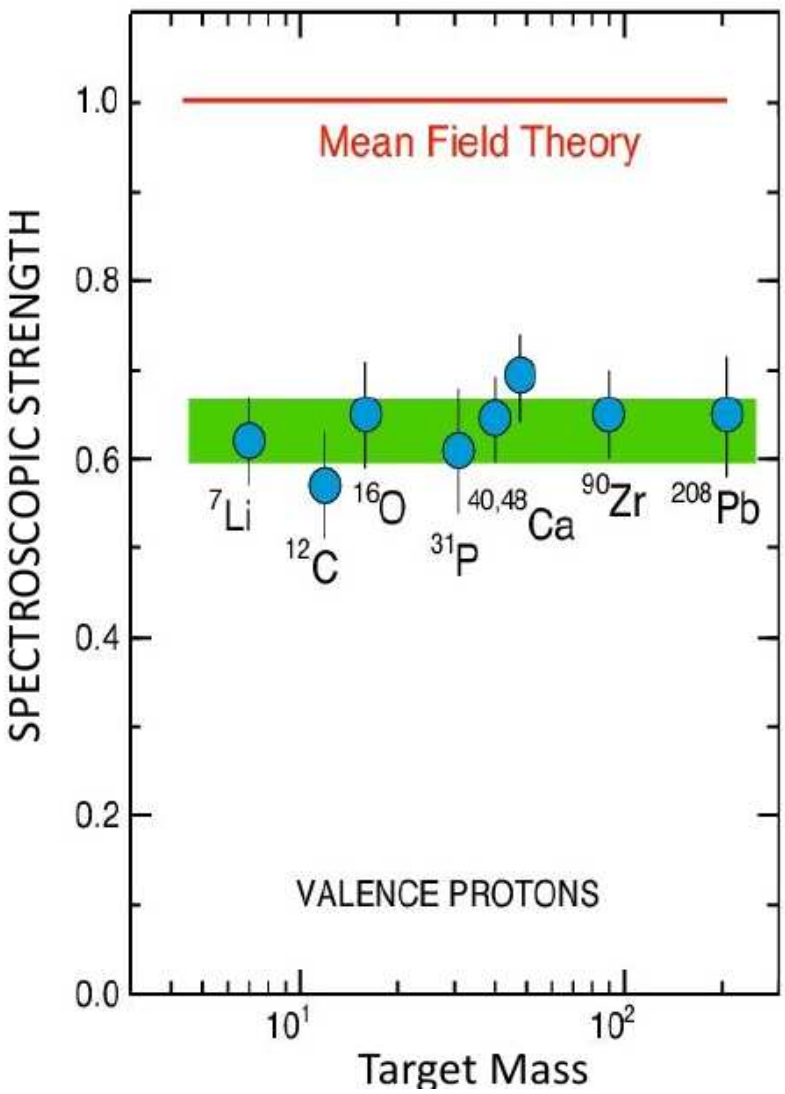


Figure 1.1: The spectroscopic strength for protons knocked out of well defined shells versus the target mass (A). The red line represents the IPSM prediction.

The missing strength is due to the correlations between the nucleons. Long range correlations between nucleons can explain less than half of the missing strength. The rest of the missing strength was attributed to short range correlations (SRC). For many years SRCs were hard to study [4] due to using low energy probes which cause SRCs to be screened by other competing processes.

With advances in accelerator technology, high energy, large momentum transfer reactions have been applied to the study of SRC in nuclei [5]. These high energy/large momentum transfer studies include inclusive A$(e, e')$ experiments at the Stanford Linear Accelerator (SLAC) [5] and more recent measurements at the Thomas Jefferson National Accelerator Facility (JLab) [6–8], semi-inclusive A$(e, e'p)$ experiments [9, 10, 26], and exclusive triple coincidence A$(p, 2pN)$ and A$(e, e'NN)$ measurements performed at Brookhaven National Laboratory (BNL) [11–13] and at JLab [14–16].

This thesis reports on an exclusive triple coincidence experiment performed at JLab to measure the $^4$He$(e, e'p)$, $^4$He$(e, e'pp)$ and $^4$He$(e, e'pn)$ reactions at high energy and large momentum transfers. This experiment (E07-006) was performed in Hall A.

In what follows, we briefly review the results of the high energy/ large momentum transfer studies that preceded the measurements reported here.

## 1.2 Terminology

Some basic terms to be used in this thesis are presented briefly below.

### 1.2.1 2N – SRC

The nucleons in the nucleus have an average separation of $\sim 1.7$ fm, however they are in constant motion and sometimes two (or more) nucleons approach each other to substantially shorter distances than average. The distance between two nucleons can not be too small due to the very strong repulsion of the nucleon-nucleon force at short distances [17]. We define a pair of close nucleons with typical distances of $\sim 1$ fm between their centers as a $2N$-SRC. Such a correlation can also be defined in momentum space. In the later case, we define $2N$-SRC as two nucleons with a large relative momentum and a small center-of-mass momentum, where large and small are relative to the Fermi momentum, which is about $\sim 250$ MeV/c in medium and heavy nuclei.

### 1.2.2 High momentum tail

Calculations of momentum distributions of the nucleons in nuclei using independent particle models show a sharp decrease as the momentum increases above the Fermi level. If correlations between nucleons are included in calculations, the momentum distribution is extended to much larger nucleon momentum. In Figure 1.2, a comparison between the momentum distributions for $^{12}$C, with and without correlations, is shown. We define the high momentum tail of nucleons in nuclei as the nucleons with momentum that exceed the Fermi momentum.

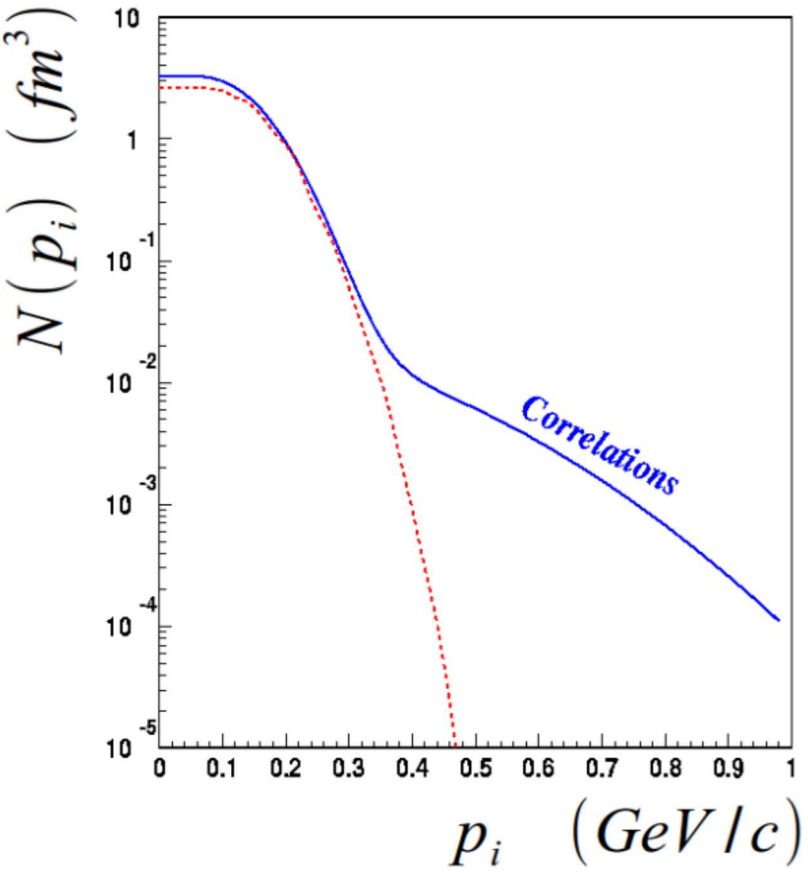


Figure 1.2: Calculation of momentum distribution in $^{12}$C with correlations (solid line) and without correlations (doted line). See Ref [18] for details.

### 1.2.3 Scaling

The dominant mechanism for generating high momenta in nucleon-nucleon interactions at short distances involve both tensor and short-range repulsive forces. The momentum distribution produced by these forces result in a universal shape for all nuclei at $p_i > k_F$, where $k_F$ is the Fermi momentum and $p_i$ the nucleon momentum, see Figure 1.3.

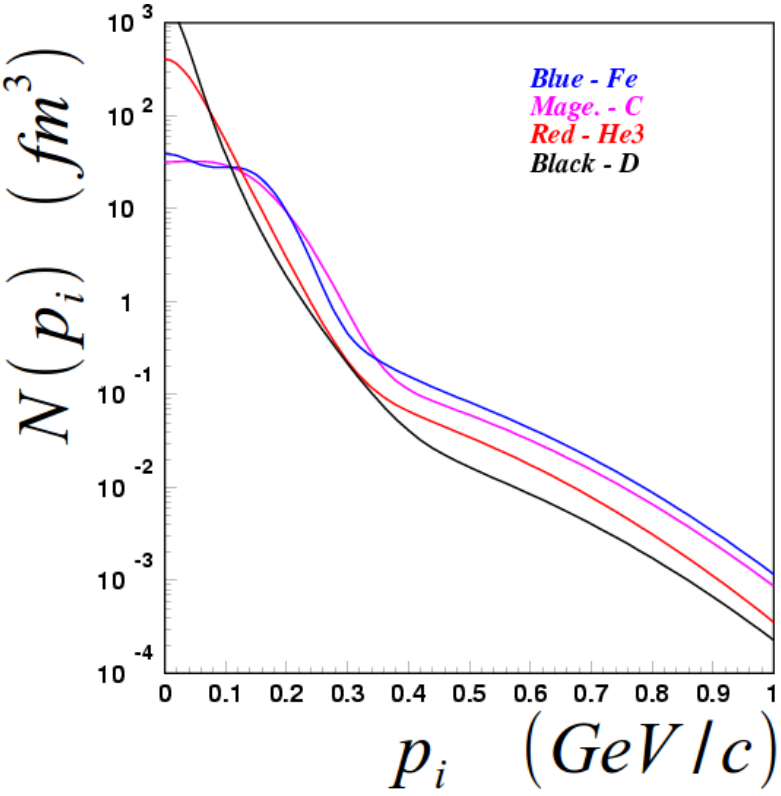


Figure 1.3: Momentum distributions for different nuclei compared to the deuteron Ref. [18].

In Figure 1.3, we see that, for low momentum, the shape of the momentum distributions in different nuclei are very different. The high momentum distributions are similar in shape for all nuclei, i.e., there is scaling.

As a result of this scaling for $p \gtrsim 1.5 \cdot k_F$, the momentum distribution for any nucleus can be written in terms of the deuteron momentum distribution:

$$n_A(k) = C_A \cdot n_D(k) \tag{1.5}$$

where $n_A(k)$, $n_D(k)$ are the momentum distributions for a nucleus with atomic mass $A$ and the deuteron, respectively.

### 1.2.4 Quasi-Elastic Scattering (QE)

Unpolarized electron beam with incident energy $E$ scattered off an unpolarized nucleon yields at a fixed scattered angle electrons with a spectrum of energies ($E'$). Lying lowest in the energy transfer $\omega \equiv E - E'$ is the elastic peak, followed by the resonance excitation region, and beyond that the pion production threshold. At greater energy transfer deep inelastic scattering is the dominant process. See Figure 1.4a.

For an unpolarized electron beam scattering off an unpolarized nucleus (beam energy $E$) the energy transfer spectrum is more complicated (Figure 1.4b). The lowest energy transfer sharp peak corresponds to elastic scattering off the nucleus as a whole, followed by exciting the nuclear resonances. The peak corresponding to energy transfer near $\frac{Q^2}{2M_N}$, where $M_N$ is the nucleon mass and $Q^2$ is the four-momenta transfer, can be identified as scattering off single nucleon in the nucleus and is called

quasi-elastic scattering (QE). The peak is slightly shifted to higher energy transfer with respect to pure elastic scattering from a free nucleon. This is due to the energy needed to remove the bound nucleon from the nucleus. The width of the QE peak is determined by the Fermi momentum of the nucleons in the nucleus.

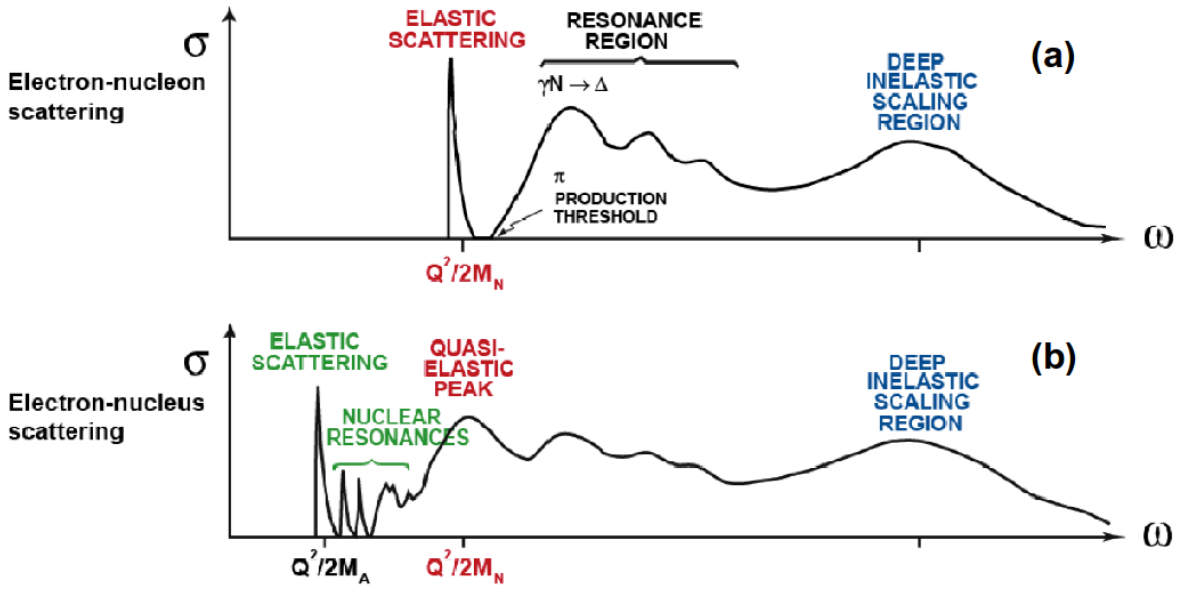


Figure 1.4: Schematic presentation of cross-section for (a) electron-nucleon and (b) electron-nucleus scattering versus the energy transfer in the reaction.

### 1.2.5 The Plane Wave Impulse Approximation (PWIA)

In this approximation, a virtual photon knocks out a bound nucleon, which propagates out of the nucleus without further interactions (such as rescattering of the struck proton by another nucleon). The remaining (A-1) system does not participate in the scattering process, see Figure 1.5. If the knocked-out nucleon was in a $2N$-SRC, its correlated partner will be ejected in the opposite direction of the missing momentum ($\vec{p}_{\rm miss}$). The missing momentum is defined by Eq 1.6:

$$\vec{p}_{\rm miss} \equiv \vec{p}_f - \vec{q} \tag{1.6}$$

where $\vec{p}_f$ is the final momentum of the knocked-out proton, and $\vec{q}$ is the momentum of the virtual photon. In PWIA :

$$-\vec{p}_{\rm rec} = \vec{p}_{\rm miss} = \vec{p}_i \tag{1.7}$$

where $p_{\rm rec}$ is the momentum of recoil nucleon, $p_i$ is the initial momentum of the nucleon before absorption of the photon.

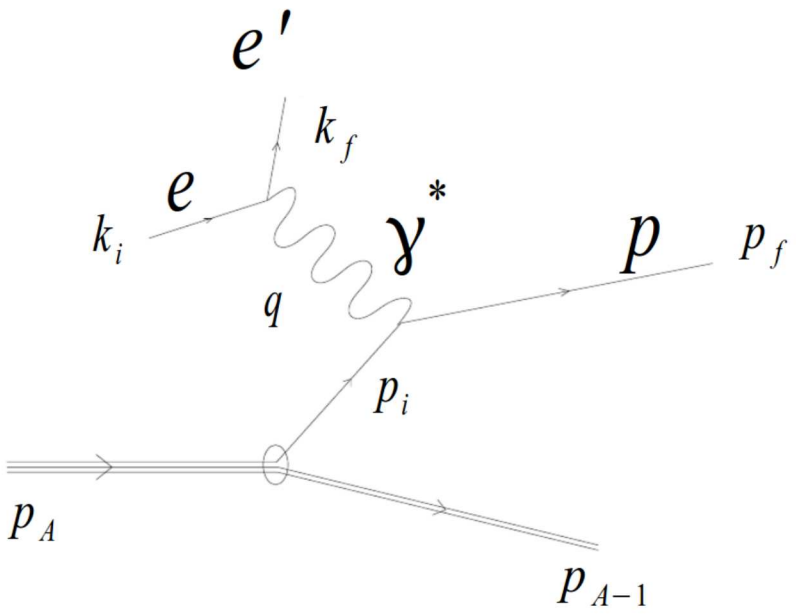


Figure 1.5: Feynman diagram presenting a QE A$(e, e'p)$A-1 reaction in a PWIA approximation.

### 1.2.6 Final State Interactions (FSI)

If we remove a nucleon from a $2N$-SRC within the QE process, this nucleon as well as its SRC partner can interact with the other nucleons as they exit the nucleus. We call these interactions Final State Interactions (FSI).

The FSI can be divided into two types. The first are interactions between the nucleons in the SRC pair itself (see Figure 1.6a) [19]. After absorption of the virtual photon the virtuality of the struck nucleon can be expressed by:

$$\Delta E = -q_0 - M_{\mathrm{A}} + \sqrt{m^2 + (p_i + q)^2} + \sqrt{M_{\mathrm{A\text{-}1}}^2 + p_i^2} \tag{1.8}$$

where $q_0$ and $q$ are the energy and momentum transfer, respectively, $M_A$ the mass of the target nucleus, $m$ the nucleon mass, and $p_i$ the initial momentum of the struck nucleon.

For initial momentum above $\sim$ 275 MeV/c, the interaction distances, based on the uncertainty principal, are less than 1 fm.

$$r \approx \frac{1}{\Delta E \cdot \nu} < 1 \text{ fm} \tag{1.9}$$

This type of FSI between members of $2N$-SRC does not change the isospin structure and the center-of-mass (CM) momentum of the SRC.

FSI between the knocked-out nucleon and the A-2 system is shown in Figure 1.6b. The main contribution to this type of FSI comes from single-charge-exchange and (SCX) and elastic or inelastic scattering described by nuclear transparency (T).

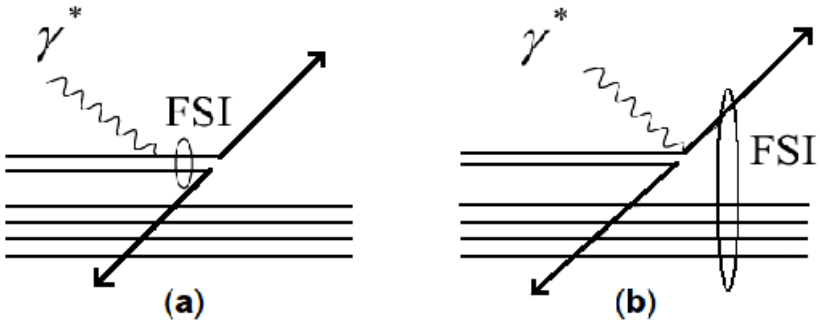


Figure 1.6: Diagrams showing FSI. (a) Between the nucleons in the $2N$-SRC, (b) between the knocked-out nucleon and the A-2 system.

Nuclear transparency, $T$(A), is defined as the ratio of cross section per nucleon for a process on a bound nucleon in the nucleus to that from a free nucleon [20]. Single-charge-exchange is a process that alters the nucleon isospin in the final state. For example, the $(e, e'n)$ events can be measured in the final state as $(e, e'p)$ events due to elastic n-p scattering of the emerging neutron with a proton in the A-2 residual nucleus [21].

### 1.2.7 Competing processes

The major challenge of triple coincidence experiments is to identify the real $2N$-SRC process from the competing channels that mask the signal and complicate the interpretation of the experimental data. The Feynman diagrams of such processes: Meson Exchange Current (MEC), and Isobar Configuration (IC) [22, 23], are shown on Figure 1.7.

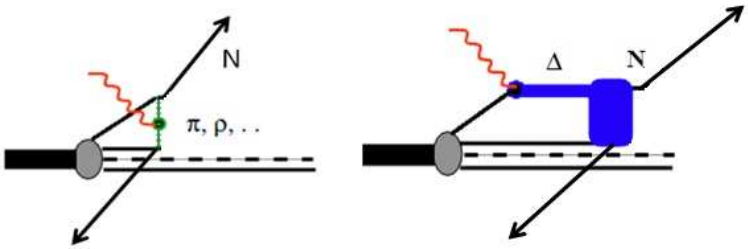


Figure 1.7: Feynman diagrams for competing processes: left (MEC), right (IC).

We can not distinguish the MEC, delta excitations, and other non FSI effects from the real $2N$-SRC, thus we have to measure the SRC in the regime where these competing processes are suppressed. This can be achieved by performing the measurement at large $Q^2$ and $x_B > 1$. Selecting anti-parallel kinematics, that correspond to $x_B = \frac{Q^2}{2m\omega} > 1$, is favorable in suppressing the contribution from the IC diagrams because $m_\Delta > m_p$, so most of the IC strength is in $x_B < 1$ [24]. This condition ($x_B > 1$) also indicates that more than one nucleon participates in the reaction. Large $x_B$ defines a minimal missing momentum ($p_i$) as will be discussed later in this thesis. Large momentum transfer is needed to probe small distances. In addition, the requirement for large $Q^2$ is used to reduce the contributions from MEC. The contribution of MEC diagrams diminishes by $1/Q^4$ as compared to $1/Q^2$ for the SRC process. It is a small correction in the kinematics relevant to SRC studies i.e. $Q^2 \geq 1$ GeV$^2$ [24]. For moderate momentum transfers, 1 (GeV/c)$^2 \leq Q^2 \leq 4$ (GeV/c)$^2$, where the contribution from $\gamma N \to \Delta$ transition is comparable with $\gamma N \to N$ [25, 26], the suppression of the IC contribution is done by

selecting events with low energy transfer (larger $x_B$), away from the inelastic threshold.

The Eikonal approximation for the description of the rescattering is applicable at large $Q^2$ and large nucleon momentum in the final state ($> 1$ GeV/c). In the Eikonal approximation, small angle rescattering for 1 GeV/c nucleons mainly causes transfer of momentum in the plane transverse to the direction of their high momentum Ref. [19].

## 1.3 Inclusive Measurements

In quasi elastic A$(e,e')$ scattering with unpolarized incident electrons and an unpolarized target, two independent kinematical variables are required to describe the reaction. We choose these to be $x_B$, and $Q^2$. The momentum of the recoil A-1 system can be obtained from energy and momentum conservation:

$$(q + p_A - p_{A-1})^2 = p_f^2 = m_N^2 \tag{1.10}$$

where $q$ , $p_{\rm A}$ , $p_{\rm A\text{-}1}$, and $p_f$ are the four-momenta of the virtual photon, target nucleus, residual $A-1$ system, and knocked-out nucleon, respectively. From the equation above we obtain:

$$\Delta M^2 - Q^2 + \frac{Q^2}{m_N x_B}\left(M_{\rm A} - \sqrt{M_{\rm A\text{-}1}^2 + \vec{p}_m^{\,2}}\right) - 2\vec{q}\cdot\vec{p}_m - 2M_{\rm A}\sqrt{M_{\rm A\text{-}1}^2 + \vec{p}_m^{\,2}} = 0 \tag{1.11}$$

where $\Delta M^2 = M_{\rm A}^2 + M_{\rm A\text{-}1}^2 - m_N^2$ and $\vec{p}_m \equiv \vec{p}_f - \vec{q} = -\vec{p}_{\rm A\text{-}1}$, is the missing momentum of the $(e,e'p)$ reaction.

This equation defines a simple relation between the minimal initial momentum of the knocked-out nucleon ($p_m^{\rm min}$) and $x_B$ at fixed $Q^2$. Following Ref. [6] this relation is presented graphically in Figure 1.8.

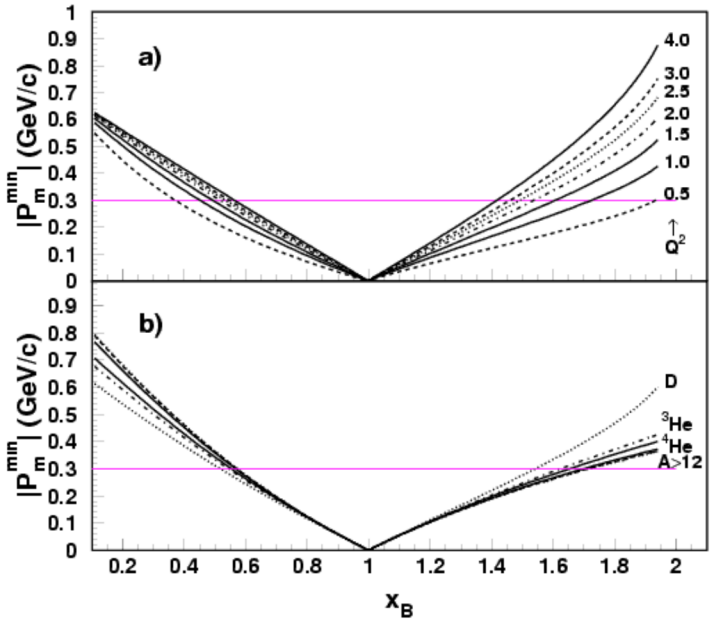


Figure 1.8: The minimum recoil momentum as a function of $x_B$. Top panel: For deuterium at several $Q^2$, Bottom panel: For different nuclei at $Q^2 = 2$ (GeV/c)$^2$. Horizontal lines represent an example of minimal momentum of 300 MeV/c. This figure was adapted from Ref [6].

Based on the above relation, the minimum momentum $|\vec{p}_m^{\,\rm min}|$ above the Fermi momentum can be

chosen by requiring $x_B^0$ to be large enough.

We define the per nucleon cross section ratio as a function of $A$, $Q^2$ and $x_B$ :

$$R\left(\mathrm{A}_1, \mathrm{A}_2, Q^2\right) = \frac{\sigma\left(\mathrm{A}_1, Q^2, x_B\right)/\mathrm{A}_1}{\sigma\left(\mathrm{A}_2, Q^2, x_B\right)/\mathrm{A}_2} \tag{1.12}$$

where $\sigma\left(\mathrm{A}_1, Q^2, x_B\right)/\mathrm{A}_1$ and $\sigma\left(\mathrm{A}_2, Q^2, x_B\right)/\mathrm{A}_2$ are the inclusive electron scattering cross sections per nucleon for nuclei with atomic numbers $A_1$ and $A_2$ respectively. If the high momentum component of the nuclear wave function for different nuclei scales, this leads to a scaling of this ratio as predicted in [27] and can be seen on Figure 1.9. In the scaling region ($x_B > x_B^0$, and $Q^2$ large enough), $R$ is a very weak function of $Q^2$ and $x_B$.

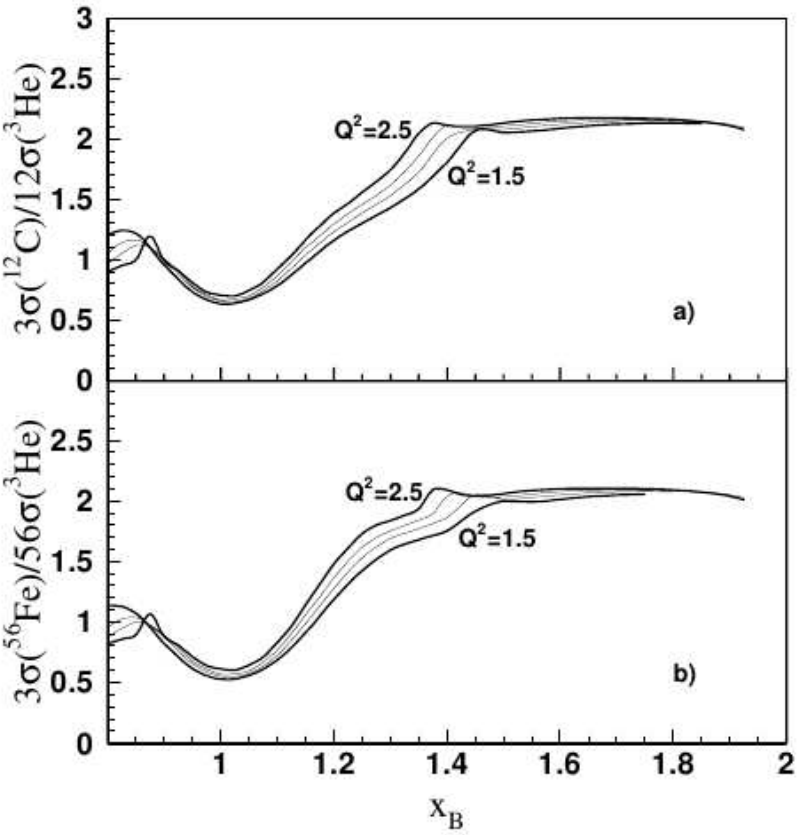


Figure 1.9: SRC model predictions for the normalized inclusive cross section ratio as a function of $x_B$ for several values of $Q^2$. a) for $^{12}$C/$^3$He b) for $^{56}$Fe/$^3$He.

Such inclusive measurements were performed at SLAC [5, 28] and later at JLab [6–8] confirming the scaling of the inclusive cross section for large $x_B$ (see Figures 1.10, 1.11 and 1.12)

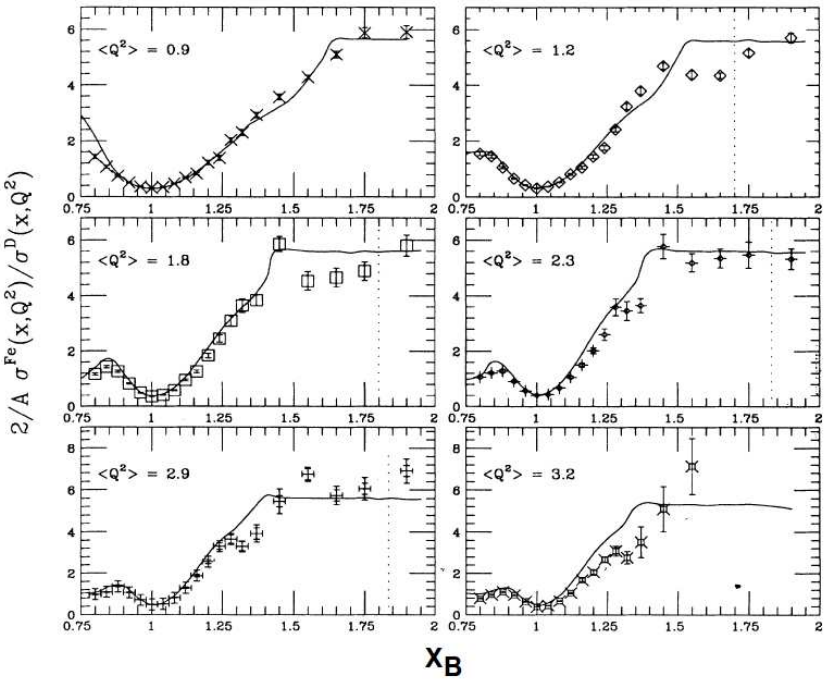


Figure 1.10: Inclusive cross section ratios,$^{56}$Fe over deuteron at different $Q^2$ values [5]. The solid lines are calculations of Ref [29].

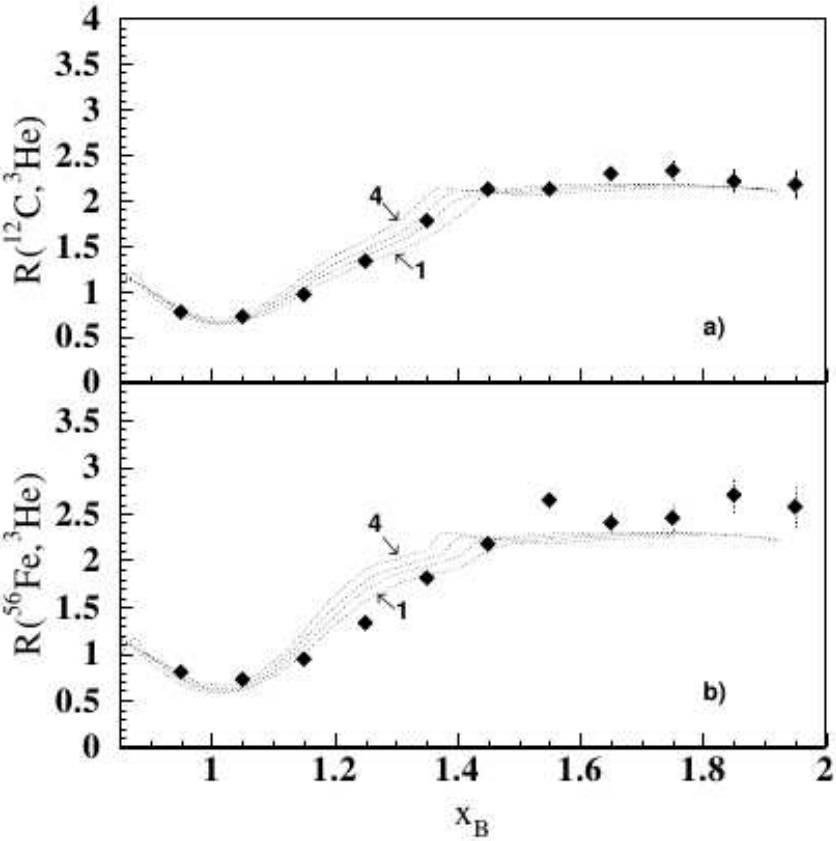


Figure 1.11: Inclusive cross section ratios of a) $^{12}$C/$^3$He, and b) $^{56}$Fe/$^3$He as a function of $x_B$ for $Q^2 > 1.5$ (GeV/c)$^2$ [7]. Curves are SRC model predictions for different $Q^2$ in the range 1.4 GeV$^2$ (curve 1) to 2.6 GeV$^2$ (curve 4).

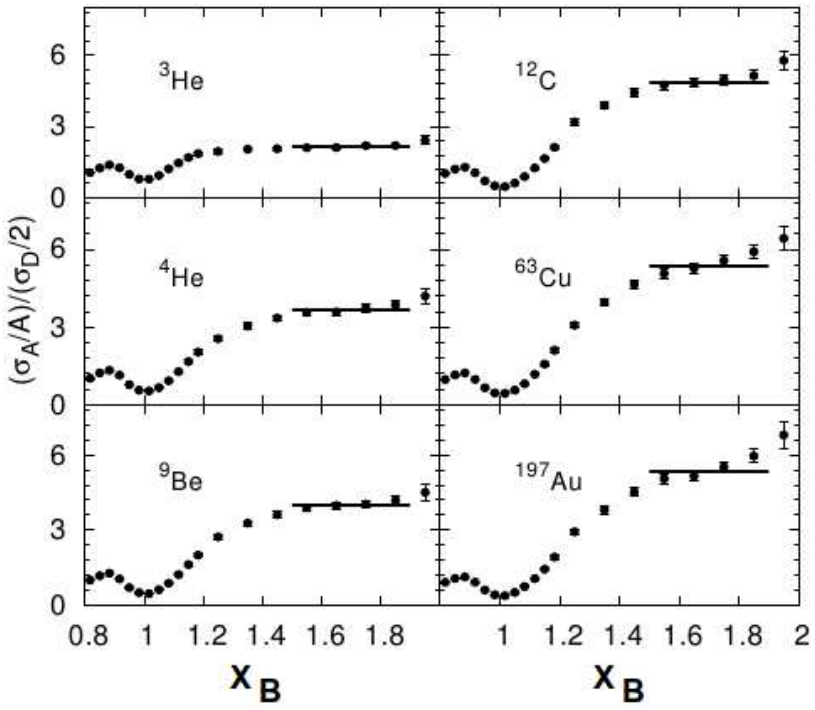


Figure 1.12: Inclusive cross section ratios of recent inclusive measurements from JLab [8].

Scaling means that the high momentum tails of all nuclei are the same up to a constant factor. A natural explanation for this scaling ($1.4 < x_B < 2$) is the dominance of the high momentum tail by $2N$-SRC, as will be discussed below. In PWIA, $x_B > 1.4$, corresponds to hitting a proton with momentum above 275 MeV/c. The scaling factor counts the number of SRC pairs and for carbon it was estimated that the probability for a proton to be a member of a $2N$-SRC is $20 \pm 5\%$. In these inclusive measurements, the electrons can scatter from $pp$, $nn$ and $np$ pairs, and therefore they do not give us information about the isospin structure of the SRC.

## 1.4 Semi inclusive measurements

Semi inclusive A$(e, e'p)$ experiments have also been used to investigate SRC. By measuring the momenta and energies of the scattered electron and knocked out proton assuming only nucleonic contributions, the initial state of the knocked out proton can be reconstructed in Plane Wave Impulse Approximation. If the knockout proton was part of a SRC pair, then the missing momentum and missing energy will be large.

The scaling behavior in A$(e, e'p)$ reactions can be derived from the analysis of the spectral function $P(k,\, E)$ [30]. The spectral function is the joint probability to find a nucleon with momentum $k$ and removal energy $E$ in the nucleus.

In a nonrelativistic Schrödinger description of nuclei, the nucleon spectral function is defined as:

$$P(k,\, E) = \frac{1}{2J_0+1} \sum_{M_o\sigma} \left\langle \Psi_A^0 \left| a^\dagger_{\vec{k},\sigma}\, \delta\left[E - (H - E_A)\right] a_{\vec{k},\sigma} \right| \Psi_A^0 \right\rangle \tag{1.13}$$

where $a^\dagger_{\vec{k},\sigma}(a_{\vec{k},\sigma})$ is the creation (annihilation) operator of a nucleon with momentum $\vec{k}$ and spin projection $\sigma$; $\Psi_A^0$ is the intrinsic eigenfunction of the ground state of the nuclear Hamiltonian $H$ with

eigenvalue $E_A$ and total angular momentum $J_0$.

Many theoretical investigations of the semi-exclusive $A(e,e'p)$ processes, have adopted a factorized approach in which the electronuclear part and the information on the energy and momentum distributions of nucleons in nucleus are separated [31]. Assuming factorization and only one proton absorbing a single virtual photon leads to the general six-fold differential cross-section for the A$(e,e'p)$ reaction given by:

$$\sigma\left(E_m,k\right)=\frac{d^6\sigma}{d\Omega_{E'}dE'd\Omega_p dT_p}\left(e,e'p\right)=K_c\sigma_{ep}P_D\left(E_m,k\right) \tag{1.14}$$

$K_c=\frac{p_pE_p}{(2\pi)^3}$ is a kinematic factor determined by the detected proton, $\sigma_{ep}$ is the off-shell (bound) electron-proton cross section that contain the electronuclear part. $\sigma_{ep}$ is obtained from Dirac equation for relativistic scattering interaction off an on-shell nucleon extrapolated for the off-shell case [32]. $P_D(E_m,k)$ is the distorted spectral function that corrects the $P(E_m,k)$ defined above for final-state interactions which affect the knock out proton. One of the latest experimental studies of the spectral function in the context of the SRC can be found in reference [33].

In simple way the spectral function can be divided in to two region, $P_0\left(k,\,E\right)$ which includes only final states of the residual system that correspond to the discrete spectrum, whereas all final states belonging to continuum spectrum contribute to $P_1\left(k,\,E\right)$.

The scaling measured in the inclusive scattering experiments is seen in the nucleon momentum distributions $n(k)$:

$$n\left(k\right)\equiv\frac{1}{2\pi^2}\int d\vec{z}d\vec{z}'e^{ik\cdot\left(\vec{z}-\vec{z}'\right)}\rho\left(\vec{z},\vec{z}'\right) \tag{1.15}$$

where (omitting spin indexes)

$$\rho\left(\vec{z},\vec{z}'\right)\equiv\int d\vec{x}\ldots d\vec{y}\left[\Psi_A^0\left(\vec{x}\ldots\vec{y},\vec{z}\right)\right]^\star\Psi_A^0\left(\vec{x}\ldots\vec{y},\vec{z}'\right) \tag{1.16}$$

The normalization of the nucleon momentum distribution $n\left(k\right)$ is chosen to be:

$$\int_0^\infty dk\;k^2n\left(k\right)=1 \tag{1.17}$$

The relation between $n(k)$ and spectral function $P(k,E)$ is:

$$n\left(k\right)=4\pi\int_{E_{\min}}^\infty dE\,P\left(k,\,E\right) \tag{1.18}$$

The momentum distribution can be separated the same way as the spectral function:

$$n\left(k\right)=n_0\left(k\right)+n_1\left(k\right) \tag{1.19}$$

where the first term corresponds to the case where the extracted nucleon leaves the A-1 system in the discrete spectrum of the $H_{\text{A-1}}$. The second term includes all final states that belong to the continuum spectrum of $H_{\text{A-1}}$.

Integrating each term over the nucleon momentum yields the occupation probability $S_0$ and $S_1$, with $S_0+S_1=1$.

$$S_0\equiv\int_0^\infty dk\,k^2n_0\left(k\right) \tag{1.20}$$

$$S_1 \equiv \int_0^\infty dk\, k^2 n_1(k) \tag{1.21}$$

In the mean field IPM picture $S_0 = 1$ and $S_1 = 0$. However nucleon-nucleon correlations alter this result. For example, a calculation shows that ground to ground transition in the nucleus yields $S_0 \approx 0.65$ and $S_0 \approx 0.8$ for $^3$He and $^4$He respectively [34–36]. In the case of the infinite nuclear matter the calculation of [37] obtain $S_0 \approx 0.75$. For most of the heavy nuclei the strength is similar to the $^4$He value [37].

$^3$He is a relatively simple system used to study $2N$-SRC with one additional nucleon being a spectator. A $^3$He$(e, e'p)$ quasi-elastic measurement was carried out in Hall A at JLab with a large momentum transfer [9, 10]. The simple reaction mechanism assumed a knocked-out proton which is a part of an SRC pair with relative momentum $\vec{p}_r$ in the center-of-mass of the SRC pair and with the other nucleons assumed to be spectators. The struck proton is knocked-out with momentum $\vec{q} - \vec{p}_r$ and the partner recoils with momentum $\vec{p}_r$. The undetected spectators constitute a residual system with a mass:

$$M_{\text{recoil}}^2 = \left[M_{\text{spec}} + \sqrt{m_N^2 + p_r^2}\right]^2 - p_r^2 \tag{1.22}$$

where $M_{\text{spec}}$ is the mass of the spectator (A-2) system (only one nucleon in the $^3$He case) and $m_N$ is the mass of the recoiling partner in the SRC pair. The missing energy is simply defined as:

$$E_m = M_{\text{recoil}} + m_p - M_{\text{target}} \tag{1.23}$$

thus the cross-section peak position as a function of missing energy strongly depends on the nucleon relative momentum $\vec{p}_r$, see Figure 1.13. This simple picture provides a clear signature for processes involving two nucleons and a spectator system. However, this picture fails to reproduce the experimental result for the highest momentum due to large three body break up processes [9].

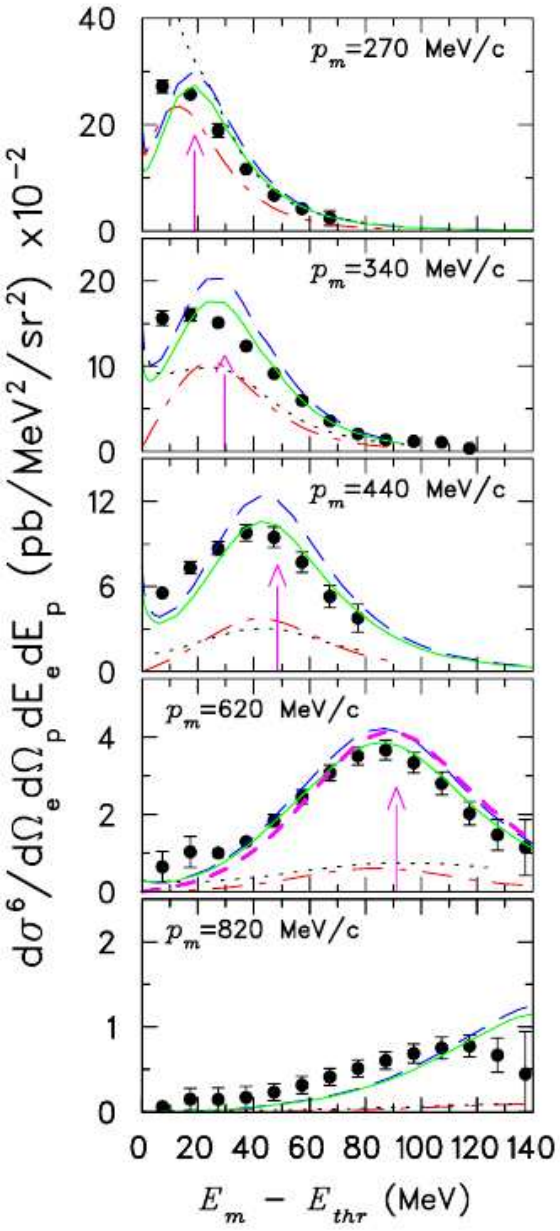


Figure 1.13: Cross-section for the $^3$He$(e,e'p)pn$ reaction versus missing energy $E_m$. The vertical arrow gives the peak position expected for disintegration of correlated pairs (except for highest energy, where the prediction fails). The dotted curve presents a PWIA calculation using Salme's spectral function and $\sigma_{cc1}$ electron-proton off shell cross-section. Other curves are recent theoretical predictions of Laget [38]: PWIA (dash dotted line), PWIA + FSI (long dashed line), full calculation (solid line) including meson-exchange current and final-state interactions. In the 620 MeV/c panel, the additional short-dashed curve is a calculation with PWIA + FSI only within the correlated pair. This Figure is reproduced from Ref. [9].

## 1.5 Triple coincidence measurements

In multi-nucleon knockout experiments, more than one outgoing nucleon is detected in coincidence. Measurements of this category include $(e,e'pp)$ measurements from MAMI and NIKHEF [39–46], and $(\gamma,NN)$ from TAGX and LEGS [47, 48]. In these experiments, the energy resolution allowed the

identification of the shells from which the proton pair was knocked-out. However, these experiments were performed at low $Q^2$ and $x_B < 1$ limiting their ability to separate the contribution from $2N$-SRC.

The first high $Q^2$ triple coincidence measurement was performed at Brookhaven National Laboratory (BNL) by the Eva collaboration using the $^{12}\mathrm{C}(p, 2pn)$ reaction [11–13]. This experiment looked for a correlation between the knocked-out proton and a recoiling neutron. The scattering was done at 90° in the CM. Two outgoing protons with high transverse momentum, $p_T$, were detected in coincidence with a recoil neutron having a momentum larger than 320 MeV/c. In this experiment the directional correlation between the knocked-out proton and recoiled neutron indicates the existence of short-range correlations above the Fermi level, see Figure 1.14. Moreover, the analysis of the data demonstrated that if a nucleon with high momentum (300 – 550 MeV/c) is removed from the nucleus at least 74% of the time it originates from $np$-SRC. In addition, from this experiment the amount of $pp$-SRC pair was estimated to be below 13%. The large difference in the $np$-SRC and $pp$-SRC abundances indicates that in this momentum region the nucleon-nucleon force is sensitive to the isospin composition of the pair and dominated by the tensor part.

From the experimental data, the CM momentum of the correlated $pn$ pair was extracted to be $\sigma = 143 \pm 17$ MeV/c. The measured CM momentum is in good agreement with theoretical, 139 MeV/c, estimate by Ciofi degli Atti *et al.* [18].

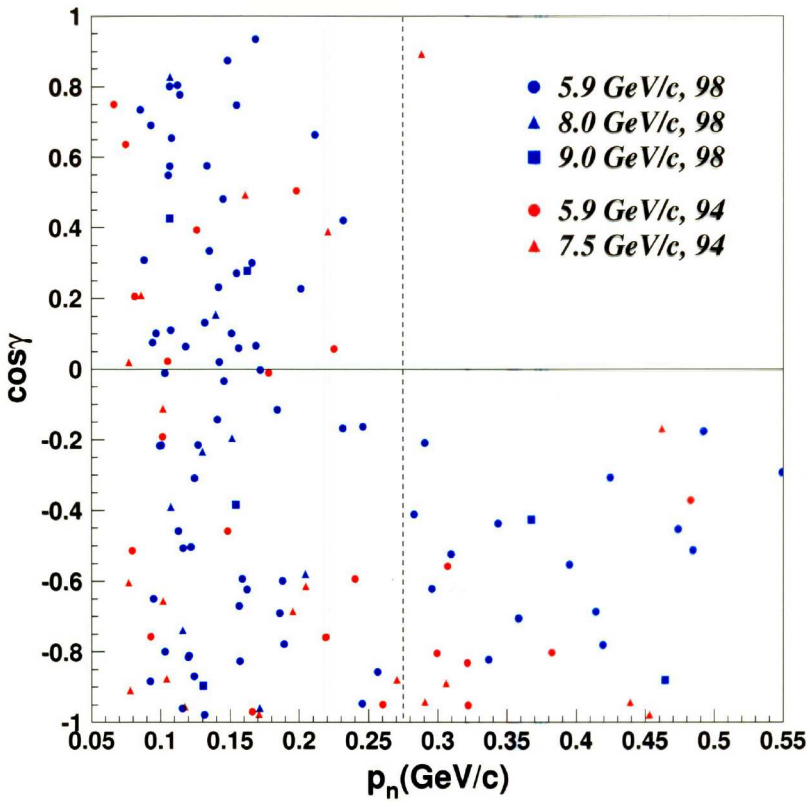


Figure 1.14: The cosine of the opening angle between the struck proton in the quasi-elastic $^{12}\mathrm{C}(p, 2p)$ reaction and the recoil neutron. Data labeled by 94 and 98 are from [11, 12] respectively. The vertical line corresponds $p_n = 275$ MeV/c.

Following the BNL experiment, another triple coincidence experiment with high momentum transfer, $Q^2 \approx 2$ (GeV/c)$^2$, was conducted at JLab in Hall A. In this experiment, energetic electrons were

scattered from a carbon target, and the $^{12}\mathrm{C}(e, e'pp)$ and $^{12}\mathrm{C}(e, e'pn)$ reactions were studied.

The advantage of a leptonic probe over the proton is that the QED vertex is very well understood.

Analysis of this experiment was consistent with the BNL results and confirmed the result of $pn$-SRC dominance by measuring the number of $np$-SRC and $pp$-SRC pairs. They found that in $^{12}\mathrm{C}$ out of the $20 \pm 5\%$ nucleons in SRC, $18 \pm 5\%$ are $np$-SRC, and $pp$-SRCs and $nn$-SRCs are only $1 \pm 0.3\%$ each. The results of this experiment are presented on Figure 1.15, adopted from [15].

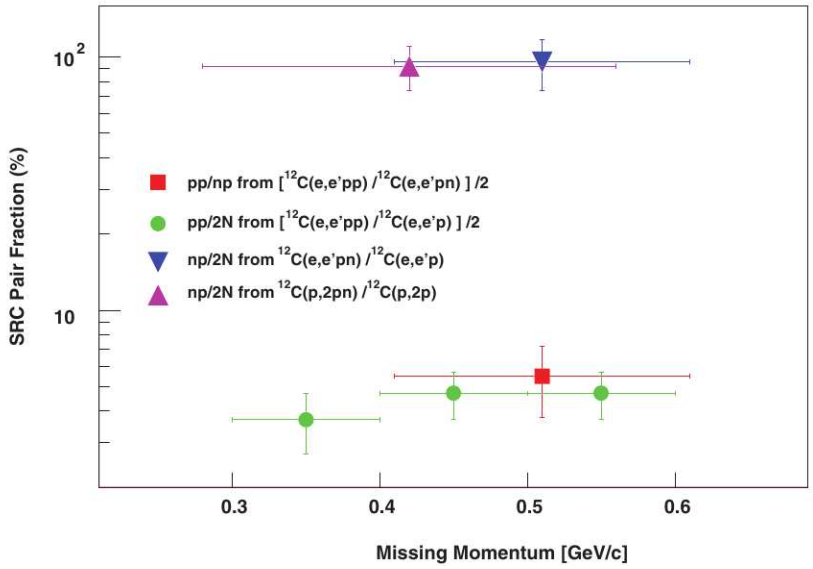


Figure 1.15: The fractions of correlated pair combinations in carbon as obtained from the $^{12}\mathrm{C}(e, e'pp)$ and $^{12}\mathrm{C}(e, e'pn)$ reactions at JLab (E01-015) [14, 15] as well as from previous, $^{12}\mathrm{C}(p, 2pn)$ data from BNL [11–13].

In addition to the BNL and Jefferson Lab Hall A exclusive measurements on Carbon target, another exclusive SRC experiment was conducted in Jefferson Lab Hall B. The $^{3}He(e, e'pp)n$ reaction was studied with 4.7 GeV incident electron beam [16]. In this experiment the detected knocked-out nucleon was a spectator that did not take part in the SRC pair. The ratio between the number of $pp$ to $pn$ pairs as a function of the total momentum ($\vec{p}_{tot} = \vec{p}_1 + \vec{p}_2$) of the SRC pair was extracted, see Figure 1.16.

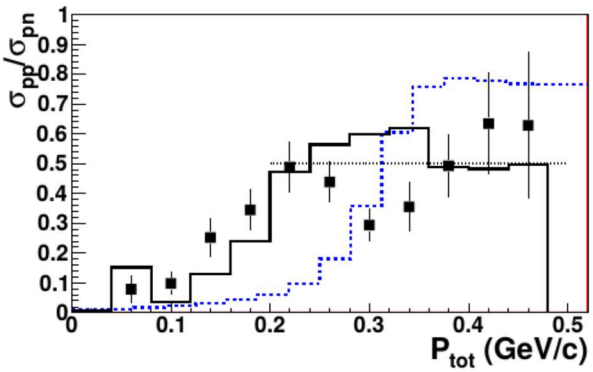


Figure 1.16: Ratio of $pp$ to $pn$ spectator pair cross sections, integrated over $0.3 < p_{rel} < 0.5$ GeV/c. The points show the data, the solid histogram shows the Golak one-body calculation [49], and the dashed histogram shows the ratio of the Golak $pp$ and $pn$ bound state momentum distributions. The dotted line at 0.5 shows the simple-minded pair counting result. The data and the one-body calculation have been multiplied by 1.5 to approximately account for the ratio of the average $ep$ and $en$ elementary cross section.

The measured ratio is very small for $p_{tot} < 0.1$ GeV/c and consistent with the BNL and Hall A results. The increase in the number of $pp$ to $pn$ pairs with $p_{tot}$ is a signal for the dominance of tensor correlations. At low $p_{tot}$, where the angular momentum of the pair with respect to the rest of the nucleus must be zero, the $pp$ pairs predominantly have (isospin, spin) $(T, S) = (1, 0)$ [50]. They are in an $s$-state, which has a minimum at $p_{rel} \sim 0.4$ GeV/c. The $pn$ pair is predominantly in a deuteron like $(T, S) = (0, 1)$ state. As $p_{tot}$ increases, the minimum in the $pp$ momentum distribution fills in, increasing the $pp$ to $pn$ ratio [16].

## 1.6 Dominance of the tensor force

The dominance of the number of $np$ pairs over the $pp$ pairs in the momentum range of the recent experiment (300 – 600 MeV/c) is understood to be caused by the tensor part of the nucleon-nucleon potential.

By looking at the pair momentum distribution functions for different nuclei as a function of the relative momentum between the nucleons in the pair, $q = 0.5 \cdot (k_1 - k_2)$, the $np$ dominance is clearly seen. See Figure 1.17.

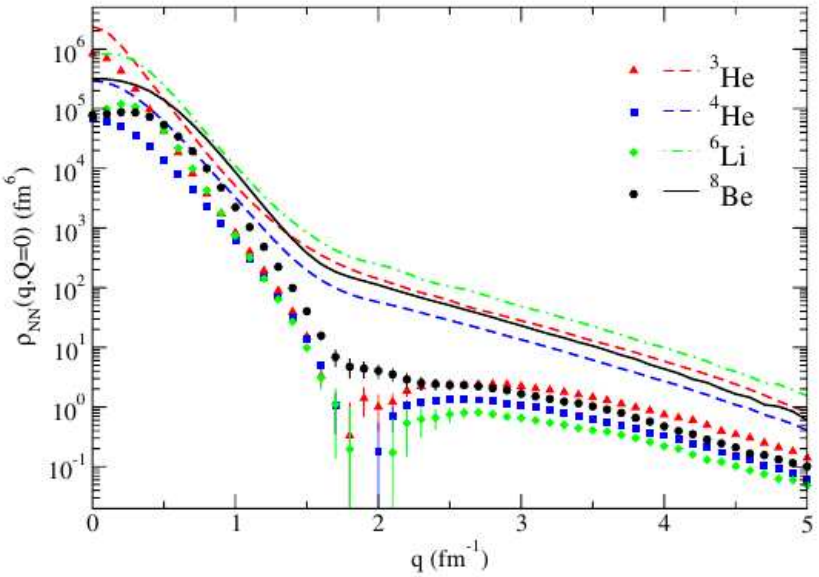


Figure 1.17: The momentum distribution ($\rho_{NN}$) for $np$ (lines) and $pp$ (symbols) pairs in various nuclei as a function of the relative momentum of the nucleons in the pair ($q_{\rm rel}$) from Ref. [50]. The calculations assume pairs at rest ($Q_{\rm CM} = 0$).

The tensor part of the nucleon-nucleon force is proportional to $S$ (total spin of the pair) term. The tensor force prefers the $S = 1$ state (symmetric spin state having two spins in the same direction) over the $S = 0$ (antisymmetric). Because the short range correlation pairs are mainly in even $L$ (0,2; symmetric space configuration) their isospin must be $T = 0$ (antisymmetric) due to Pauli's principle. As a result the tensor force will affect $np$-SRC, while the $pp$-SRC (or $nn$-SRC) pairs will not be affected, because they are at $T = 1$ and for even $L$ they must be in $S = 0$ state.

Normally the tensor part of the $NN$ interaction is small but it becomes important in the momentum range where the scalar force approaches zero ($\sim 0.75$ fm). In Figure 1.18 the central part of the nucleon-nucleon potential with an insert of the tensor potential are presented.

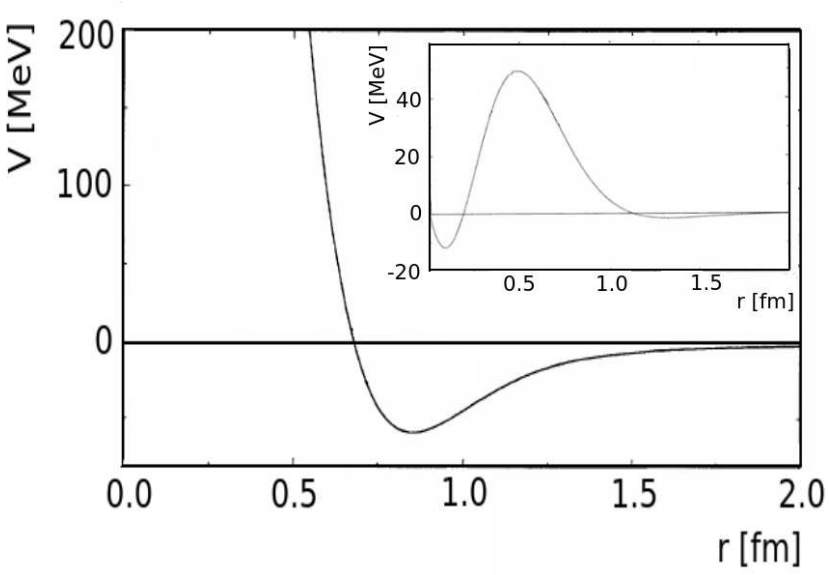


Figure 1.18: The main figure shows the central part of nucleon-nucleon potential. The insert present the tensor part of the potential. The potential is taken from AV18 [50]. Its clearly seen that generally a much weaker tensor part, becomes dominant in the region probed by the E01-015 experiment (300−600 MeV/c).

## 1.7 New Experiment on $^4$He

Previous SRC experiments showed dominance of the tensor force by looking on the ratios between number of *np*-SRC to *pp*-SRC pairs. Following the results of previous triple coincidence experiments and theoretical predictions, a new exclusive scattering measurement was proposed and conducted. The main goal of this new experiment is to increase the missing momentum and to look for pairs which are even closer to each other, at such distances that the interaction between them is dominated by the repulsive core. In the transition to the repulsive force dominance we expect an increase in the *pp*/*np* ratio, see for example Figure 1.19. This experiment provides the first insight into the nature of the essentially unexplored repulsive core, which is considered to be a scalar.

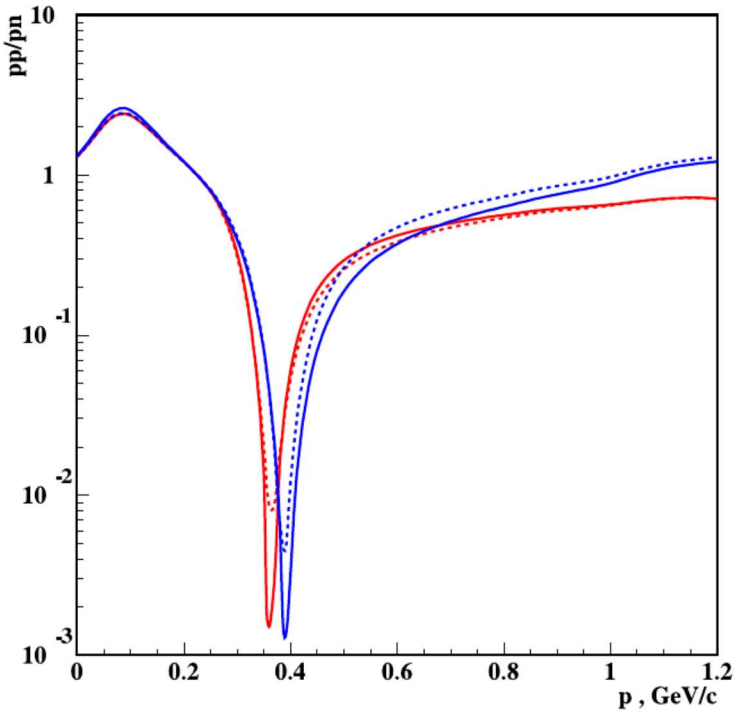


Figure 1.19: The density distribution for $np$ (red) and $pp$ (blue) pairs in $^3$He. The figure shows the $pp/np$ ratio with/without three nucleon forces (dashed/solid lines) included for V18 (red) and Bonne (blue) potentials. Figure adapted from [51].

In the reported experiment here, electrons were scattered from a $^4$He target. We performed simultaneous measurement of the $^4\mathrm{He}(e,e'pp)/^4\mathrm{He}(e,e'p)$, $^4\mathrm{He}(e,e'pn)/^4\mathrm{He}(e,e'p)$ and $^4\mathrm{He}(e,e'pp)/^4\mathrm{He}(e,e'pn)$ ratios. The choice of $^4$He target was due to the fact that this is the smallest dense nucleus. The small number of spectator nucleons reduce background from competing processes and FSI. Moreover, theoretical groups from Perugia and Argonne and others recently calculated nucleon-pair momentum distributions for light nuclei (A$\leq$12) so that the experimental results can be compared to these calculations.

# Chapter 2

# Experimental setup

## 2.1 The accelerator and the experimental hall

JLab operates the Continuous Electron Beam Accelerator Facility (CEBAF) which is capable of supplying a continuous high current (200 $\mu$A) electron beam with a maximum energy of about 6 GeV (the accelerator is being upgraded now to 12 GeV). The electrons are pre-accelerated to 45 MeV by the injector and injected into the accelerator from either a thermionic or a polarized electron gun. In the latter case, the source can supply up to 80% polarized electrons. After the injector, electrons are accelerated by two superconducting LINACs connected by two bending arcs. Each LINAC consists of three cryo modules with eight units inside. The cryo modules are made from Niobium and are cooled to 2 K. In each LINAC pass, the electrons gain roughly 1 GeV. The acceleration is done using radio frequency (RF) cavities. The accelerator supplies a continuous electron beam with a high duty factor. The electron beam can be supplied to three experimental Halls A, B and C simultaneously (additional experimental Hall D is under construction and will be operational with the 12 GeV upgraded machine). The current and the beam energy can be controlled separately for each hall, it can be split arbitrarily between three interleaved 499 MHz bunch trains. One such bunch train can be peeled after each linac pass to any one of the Halls using RF separators and septa. On Figure 2.1, the schematic layout of JLab accelerator is shown.

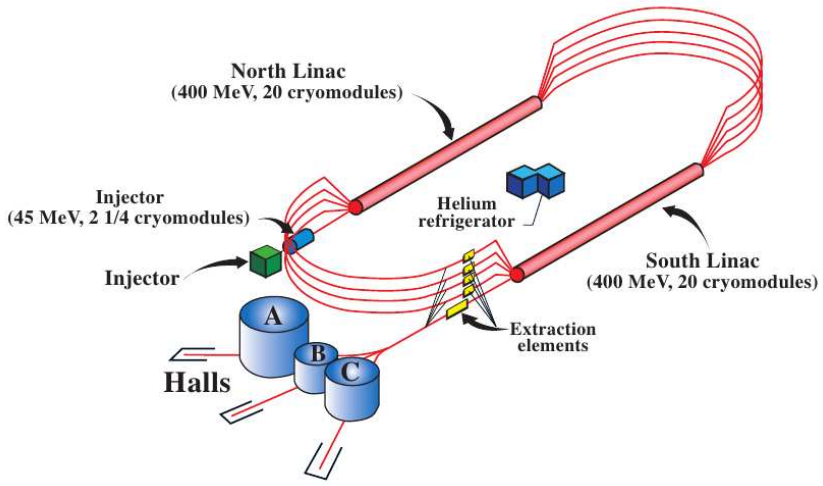


Figure 2.1: Schematic layout of JLab accelerator site (before the 12 GeV upgrade).

### 2.1.1 Experimental Hall A – CEBAF

Hall A is the largest of the experimental halls at JLab [52]. The shape of the hall floor is circular with the diameter of 53 m. The layout of the hall for this experiment is shown in Figure 2.2.

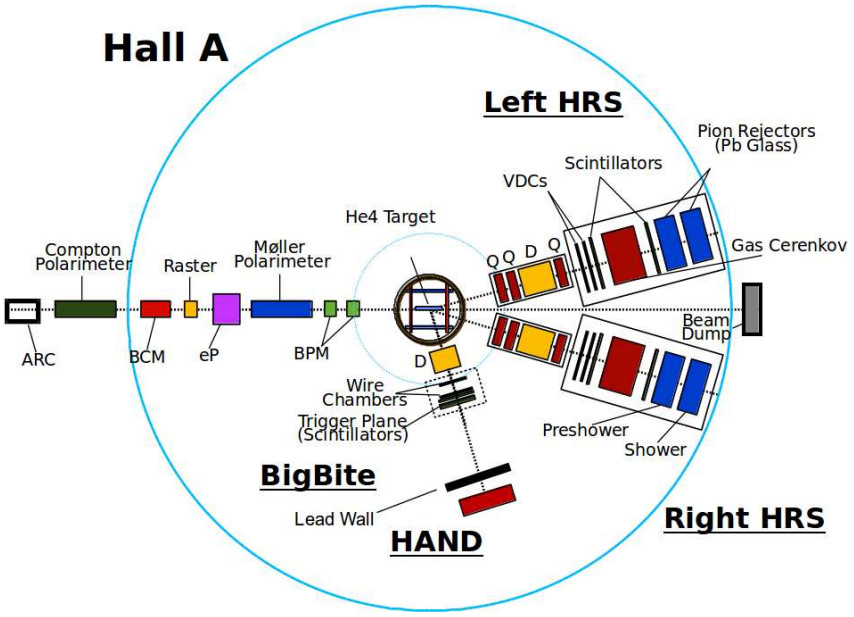


Figure 2.2: Schematic layout of the experimental hall A showing the approximate location of the detectors and indicating various beam line diagnostic instrumentation.

The beam entering the hall is monitored by various beam line instrumentation such as position monitors (BPM) and current monitors (BCM) as shown in Figure 2.2. Downstream in the center of hall there is a scattering chamber. This chamber can contain different targets including cryogenic targets at about 20 K with different pressures, various solid targets, and optic targets. Changing targets is possible remotely and the target information is recorded in the data stream. At the end of beam line, there is a beam dump.

The standard measuring equipment of Hall A are two High Resolution Spectrometers (HRS) [52]. These spectrometers with a momentum resolution $\Delta p/p = 2 \cdot 10^{-4}$ were designed to study nuclear structure with high precision. The HRSs can measure the scattered particles from 12.5° to 165°.

### 2.1.2 Beam line

In order to measure the electron beam, various instrumentation is located along the beam line (see Figure 2.2). Multiple parameters are measured simultaneously to allow correction and recording of the beam data.

One of the crucial beam diagnostic elements are the beam position monitors (BPM). It is important to monitor beam position and to keep the beam position on target stable. The BPMs are centered at the nominal beam position and have four antennas with parallel orientation. The BPMs measure the current that induced on these antennas by the passing electrons. This current is recorded using an Analog to Digital Converter (ADC) and with an appropriate scaling factor converted to the position in the $x - y$ direction (perpendicular to the beam direction, $z$).

The high current requires careful monitoring to prevent damage of the targets. In order to prevent possible damage, the beam is rastered on the target to a few mm spot instead of its natural spot size

of $\sim 100$ micrometer. When the current is less than $\sim 5\,\mu$A, there is no need for rastering even for the cryogenic targets. Precise measurement of the beam current is done by two RF Beam Cavity Monitors (BCM) placed 24.5 m upstream of the target. The output of these BCMs is proportional to the beam current.

Both the BCM and the BPM are non – invasive continuous measurements of the beam properties.

An additional important measurement is the absolute beam energy. For this purpose there are two techniques, one non invasive, arc energy method, and second invasive, $ep$ scattering method. The non invasive technique determines the electron momentum by measuring the bend angle of the electron in a known magnetic field. The invasive method is used to measure the angles of elastic scattering $\mathrm{H}(e, e'p)$ reaction. The precision of the beam energy measurement is of the order of 1 MeV for a 4 GeV beam.

### 2.1.3 Target

The Hall A target chamber is located at the center of the hall and contains a cooling system, temperature and pressure monitors, and a target ladder. The picture of the scattering chamber is shown in Figure 2.3.

The standard scattering chamber can contain 3 cryogenic loops (pairs of aluminum cylindrical target cells) with different lengths, and a number of solid targets for calibration or measurement. In the current experiment only two cryogenic loops were utilized due to the limited supply of cryogenic liquid. The Cryogenic target cells are horizontal aluminum cylinders oriented along the beam, having upstream and downstream windows of 0.1 mm (4 mil) and wall of 0.18 mm (7 mil). The diameter of the cells is approximately 6.5 cm. The length of the cells varied with the target type, see details below.

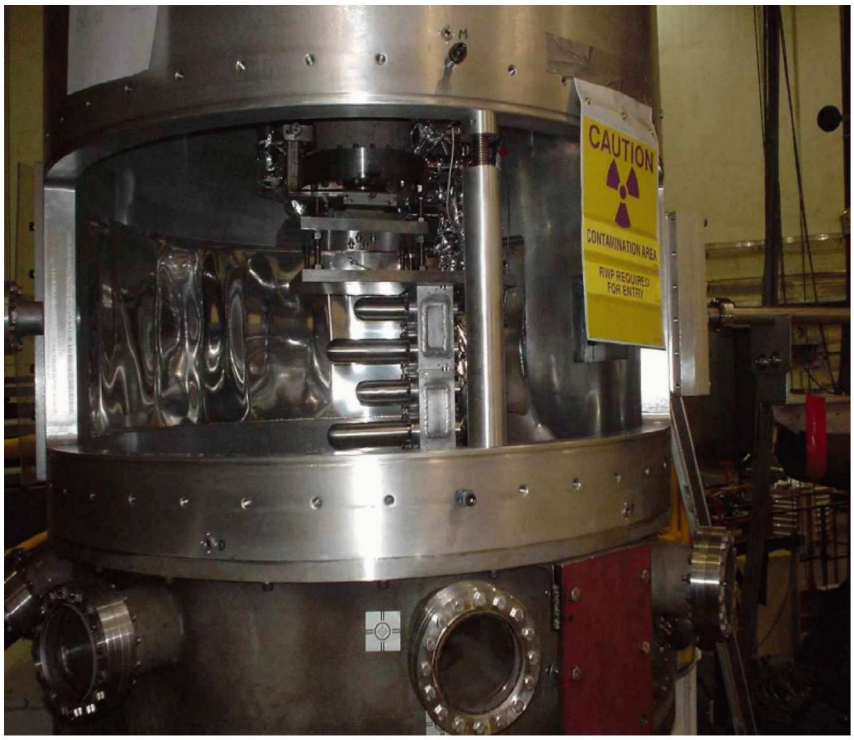


Figure 2.3: Picture of scattering chamber. In the center of the chamber various targets on the ladder are seen. See text for details.

Below is the list of targets that were used during the calibration runs:

- Hydrogen $^{1}$H:

Two liquid Hydrogen target cells one 4 and 15 cm long. These targets were used to perform *ep* elastic scattering for calibration of HRSs, BigBite, and HAND.

- Deuterium $^{2}$H:

Three liquid Deuterium target cells were used: 4, 10 and 15 cm long. The Deuteron target was used mainly for neutron detection efficiency measurement and calibration.

- Carbon $^{12}$C:

This thin (0.25 mm) solid target was tilted by 20° with respect to the incoming electrons. This was done in order to minimize the path inside the material for the recoiled protons. The target was used for calibration and to compare with the previous experiment (E01-015) [14, 15].

- Multi Carbon Foil ("Optic target"):

13 thin carbon foils placed along the beam line. This target was used to calibrate the optics of the HRSs.

- "Dummy target":

This target is two aluminum foils, 20 cm separation. It was used to measure the background produced by the aluminum walls.

- BeO:

This target is used to visualize the beam position at the target on a video screen.

During the production runs, one loop (cell with a length 10 or 20 cm) was filled with the liquid Deuterium (at 22 K). This target was used for the absolute determination of time-of-flight for neutrons (see section 3.4.7). The second loop (cell with length 10 or 20 cm) was filled with $^{4}$He at 20 K (density 0.035 g/cm$^{3}$). Figure 2.4 shows a schematic view of the target ladder including the cryogenic cells and solid targets that were used during the production runs.

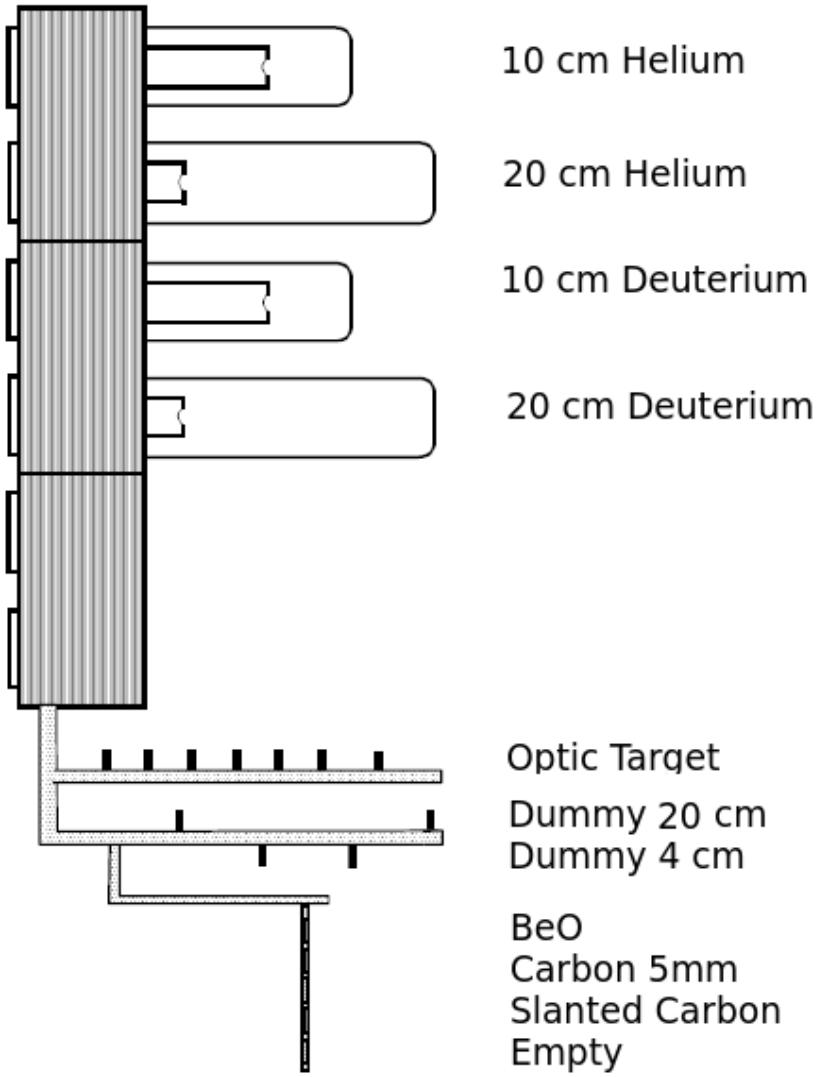


Figure 2.4: Schematic view of the target ladder used for the production runs.

## 2.2 High Resolution Spectrometers

The main detectors in Hall A are the pair of High Resolution Spectrometers (HRSs) that were designed for precise measurement of charged particles with momenta up to 4 GeV/c. Both HRSs are almost identical except for minor differences in the detector packages which can be varied based on the experimental requirements. The general characteristics of both HRSs are summarized in Table 2.1 below and the general layout of the HRS is presented in Figure 2.5.

| | |
|---|---|
| Momentum Range | 0.8 – 4.0 GeV/c |
| Vertical Bend Angle | 45° |
| Optical Length | 23.4 m |
| Momentum Acceptance | ±4.5% |
| Momentum Resolution (FWHM) | $2 \times 10^{-4}$ |
| Angular range | 12.5°–150° |
| Angular Acceptance Horizontal (Vertical) | ±28 mr (± 60 mr) |
| Solid Angle Rectangular (Elliptical) approximation | 6.7 msr (5.3 msr) |
| Angular resolution (FWHM) Horizontal (Vertical) | 0.5 mr (1.0 mr) |
| Transverse length acceptance | ±5 cm |
| Transverse position resolution | 1 mm |

Table 2.1: General characteristics of HRSs

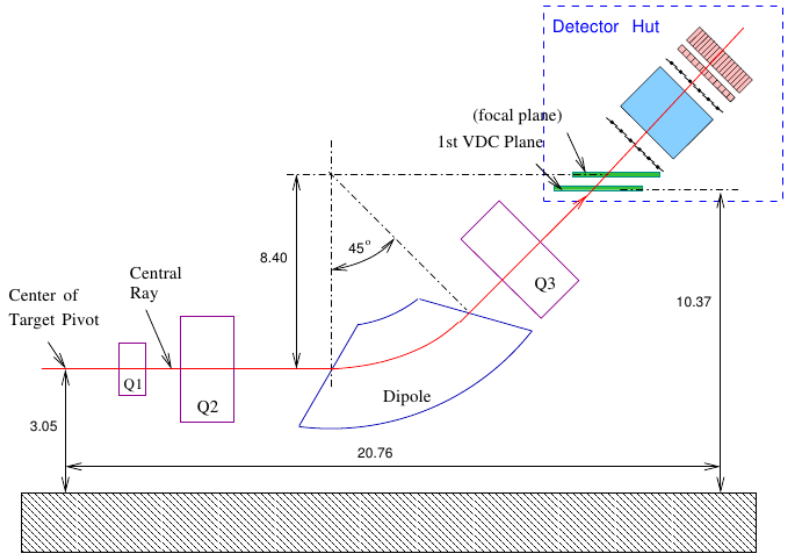


Figure 2.5: Schematic layout of the HRS spectrometer, showing the geometrical configuration of the three quadrupole and the dipole magnets. Also shown is the location of the detector hut. Dimensions are given in meters.

The main part of the HRS is a dipole magnet that bends charged particles vertically by 45°. The polarity of the dipole can be changed in order to detect positive or negative particles. At a particular magnetic field of the dipole only charged particles with in a specific narrow momentum range pass through the spectrometer and reach the detector package. Three quadrupole magnets located along the nominal trajectory of the particle, Q1, Q2 and Q3, are responsible for focusing. For more details see Hall A NIM paper [52].

The detector package is located in a hut at the top of the spectrometer that is maintained at constant temperature and serves as a radiation shield. The schematic layout of the detector package is presented in Figure 2.6:

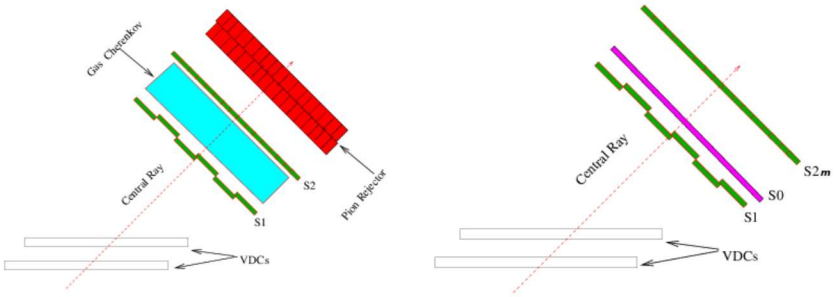


Figure 2.6: Side view of the detector stacks in each spectrometer. The left / right sketch shows the detectors in the left / right HRS. In this experiment the left HRS was used to detect electrons and the right HRS detected protons.

### 2.2.1 Vertical Drift Chambers (VDCs)

At the entrance to the detector package, a pair of Vertical Drift Chambers (VDC) is located with a 23 cm gap between them. Each chamber is composed of two wire planes inclined at an angle of 45° with respect to the dispersive and non dispersive directions. The chambers are filled with 63%/37% argon/ethane gas mixture that is carefully monitored during the measurements. The high voltage for the individual wire planes is about $-4$ kV, while the wires are kept grounded.

Charged particles that pass through the chamber ionize the gas. Free electrons are drifting to the anode wires and ionize more electrons on their way ultimately resulting in an electron avalanche. Due to this avalanche electrical signal is induced on the wires, preamplified and send to the front end electronics (TDCs). The drift time recorded in TDCs are converted to drift distance. Combining the drift distances from all wires that fired, allows the calculation of the hit position and charged particle trajectory. The final position resolution of these VDCs is about 100 $\mu$m and angular resolution is about 0.5 mrad. In Figure 2.7 a schematic layout of the VDCs is shown.

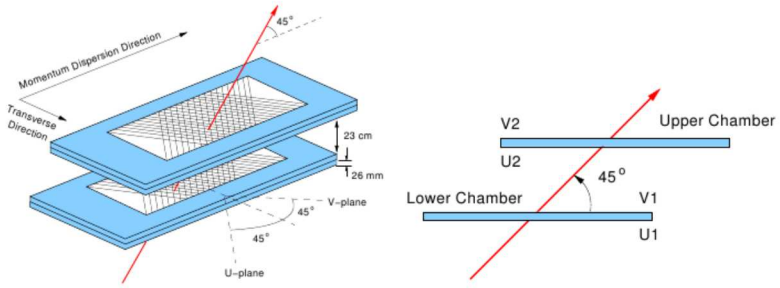


Figure 2.7: Schematic layout of the Hall A VDCs. Left: the orientation of the wires planes relative to the central ray is shown. Right: side view of the VDC is presented.

### 2.2.2 Scintillators

The scintillator planes s1 and s2m supply the primary trigger for the HRSs. They are separated by a distance of about 2 meters. Each of the planes is composed of overlapping thin scintillator bars. The s1 plane has 6 paddles, and s2m has 16 paddles. The active area of each s1 (s2m) paddle is about $29.5 \times 35.5$ cm$^2$ ($37.0 \times 54$ cm$^2$). Each scintillator bar is viewed by two Photomultiplier tubes at each

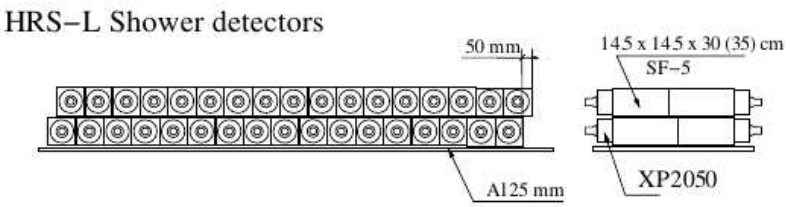


Figure 2.8: Layout of lead glass blocks of the pion rejector.

end. The time resolution of each plane is approximately 0.3 ns. In addition, in the right HRS a third scintillator plane (s0) was added. The s0 plane is mainly use for efficiency measurements.

### 2.2.3 Pion Rejector

The pion rejector is an electromagnetic calorimeter that is used for particle identification by measuring the energy deposition of charged particles. This detector is composed of two layers of lead glass blocks. Each layer consists of 17 long blocks of dimensions $15 \times 15 \times 35$ cm$^3$ and 17 short blocks of dimensions $15 \times 15 \times 30$ cm$^3$. The side and front layout of the blocks are shown in Figure 2.8.

Hadrons, such as pions, deposit less energy than electrons or positrons in the calorimeter.

### 2.2.4 Gas Cherenkov

The gas Cherenkov detector is used in the electron spectrometer for particle identification (and for some experiments to generate auxiliary triggers). The gas that was used was atmospheric $CO_2$ with refractive index of 1.00041. Cherenkov radiation is generated when the charged particles travel faster than the speed of light in that material. The minimal momenta of the particle needed to generate Cherenkov radiation strongly depends on its mass, in case of electrons this momentum is $\sim 17$ MeV/c but for pions it is 4.2 GeV/c. Since the HRS is limited to 4 GeV/c, only electrons should emit Cherenkov light. This detector is mounted between the s1 and the s2m scintillator planes.

## 2.3 The BigBite Spectrometer

BigBite is a non focusing large acceptance spectrometer that was originally commissioned during the previous Short Range Correlations experiment E01 – 015 [53]. BigBite's magnet is a dipole that bends the charged particles trajectories. From the bending angle, the particle's momentum can be reconstructed. The front side of the BigBite magnet is about 1 meter away from the target. It has a fifteen times larger acceptance than the HRS. The nominal acceptance of BigBite is about 10° in the scattering plane (horizontal angle) and $\sim 30°$ out of plane (vertical angle).

BigBite is mounted on a frame that holds the magnet and detectors which can be rotated around the pivot at the center of the target. During this experiment, BigBite was on the right side of the beam line. The right HRS in the forward direction and beam line at backward angles limited the available range for BigBite angles to 65°–100°. In Figure 2.9, a three dimensional drawing of BigBite is shown. BigBite limited the available angles for the right HRS to 12.5°– 44°.

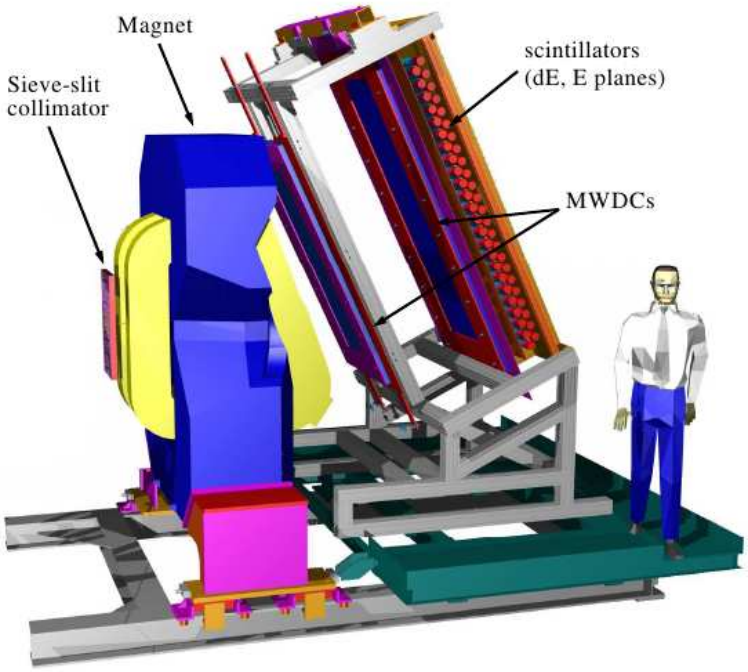


Figure 2.9: The BigBite spectrometer. Shown are the Detectors package and the magnet. In front of the BigBite magnet is shown a sieve slit collimator that can be lowered for calibration purposes.

The BigBite spectrometer has two types of detector packages: "hadron" and "electron". The original commissioning was done with the hadron package. The electron package is considerably different, however in this experiment it was not used and will not be presented in this thesis. With the hadron package, BigBite is capable of detecting protons between 300 and 900 MeV/c. The original hadron package was composed of three scintillator planes: auxiliary, $\Delta$E and E. The $\Delta$E and E planes together are referred to as the trigger plane (TP). Since its first use at JLab (2004 – 2005), the hadron package was modified and the auxiliary scintillator plane was replaced with two Multi Wire Drift Chambers (MWDC) in order to increase the momentum and angle resolution of the detected particles [54].

The detector package is mounted on a rotated aluminum frame. The rotation is needed ensure that the central momentum track pass perpendicular to the detectors plane. The frame was rotated by 25° with respect to the vertical direction. The main characteristics of the BigBite spectrometer are listed in Table 2.2.

| | |
|---|---|
| Optical Length | $\sim$ 2.7 m |
| Bending angle | 25° |
| Momentum Range | 300 – 900 MeV/c |
| Momentum resolution | 1.5% |
| Angular acceptance Horizontal (Vertical) | $\sim$ 240 mrad ($\sim$ 500 mrad) |
| Angular resolution Horizontal (Vertical) | 7 mrad (16 mrad) |

Table 2.2: Main characteristics of the BigBite spectrometer

### 2.3.1 MWDC

As mentioned above, the BigBite's hadron package contains two MWDCs [55]. The first chamber is located $\sim$ 30 cm from the magnet exit window and the second 76 cm downstream from the first chamber. The chambers were built at the University of Virginia. In contrast to the VDC in the HRSs,

each chamber has 6 wire planes in 3 different orientations, $u$, $v$ and $x$. The first two planes are $(u, u')$ oriented at an angle of 60° with respect to the long axis of the chamber. The next planes $(x, x')$ are aligned horizontally, and the last two planes $(v, v')$ are rotated to $-60°$. The planes labeled by primes have the same orientation as the unprimed planes but are shifted by a half of a signal wire spacing relative to them. This is done in order to resolve the left / right ambiguities in translating the drift time to position.

Each wire plane is constructed from two wire types. The first type is a signal wire with 1 cm spacing. They are made from 25 $\mu$m thick gold plated tungsten. The second type, are the High Voltage wires made from 90 $\mu$m thick copper – beryllium alloy and were set to $\sim -1600$ V. Each wire plane is located between two cathode planes.

The first MWDC has an active area of $140 \times 35$ cm$^2$ and contains 141 signal and field wires for the $u, u', v$ and $v'$ and 142 wires for the $x$ and $x'$. The second chamber is larger and its active area is $200 \times 35$ cm$^2$, and it contains 200 wires for $u, u', v$ and $v'$ and 202 wires for $x$ and $x'$.

The gas was a mixture of argon (50%) and ethane (50%).

The size and direction of the particle momentum was reconstructed using the hit pattern information extracted from the MWDC and the magnetic filed of the dipole ($B \sim 0.93$ T). See Figure 2.10 for a schematic drawing of the first BigBite MWDC.

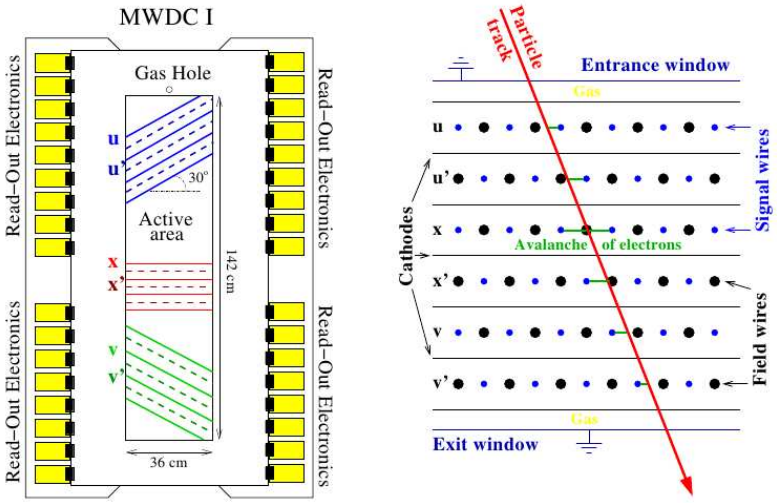


Figure 2.10: On the left side a schematic view of BigBite's first MWDC, size of active area, orientations of the wires, and the read out electronics are shown. A particle tracking through the MWDC is shown on the right.

### 2.3.2 Trigger Plane

The trigger plane (TP) is constructed from two scintillator layers ΔE and E. Each layer consists of 24 scintillators coupled to a PMT at each end. Each bar covered an area of $500 \times 86$ mm$^2$. The first layer of TP seen by the particle in the spectrometer is the ΔE layer, with a thickness of 3 mm. The second E layer has a 30 mm thickness. The active area that was covered by the TP was about $500 \times 2100$ mm$^2$. The E plane generated the single trigger signal for the BigBite detector and was used as a reference time for the MWDC. The singles rate was about 5 – 10 MHz for the full acceptance. The high background rate during the production required a relatively high level of the threshold that reduced the efficiency of the ΔE plane for high momentum protons with low light production.

The first scintillator plane was shifted by one half of a single counter width in order to cover the gaps between the counter in the other plane. This shift also served to increase the position resolution in the dispersive direction compared to the original BigBite detector package that did not have an MWDC. The introduction of the MWDC with their superior position resolution made this consideration obsolete.

The scintillators were made of EJ-204 material, which was cut and diamond milled by ELJEN Technology. The light guides were made from BC-800 produced by BICRON. These light guides were glued to the PMT using a silicon elastomer while the scintillators were glued to a grove in the center of light guide face using Eljen optical cement. In Figure 2.11, a schematic drawing of the trigger plane is shown and in Figure 2.12 a side view of the trigger plane is presented.

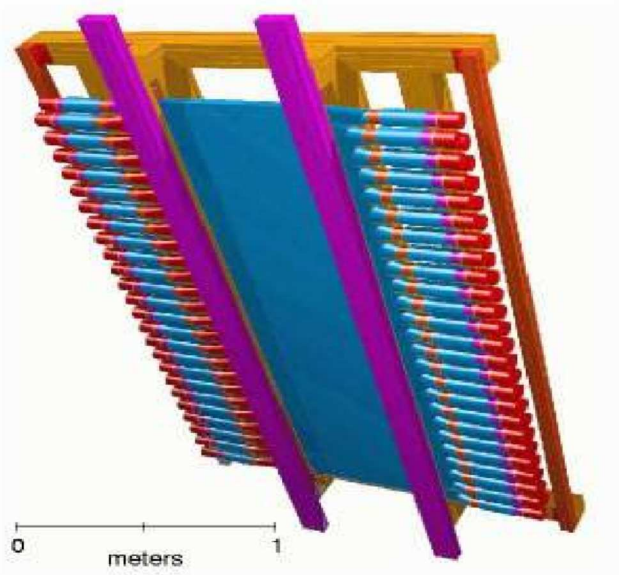


Figure 2.11: A 3D rendering of the trigger plane, showing the ΔE and E planes. Each scintillator bar in both planes has two PMTs attached, one at each end.

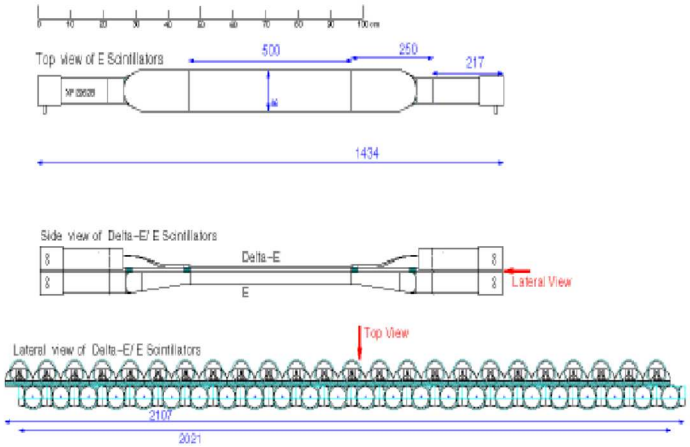


Figure 2.12: A schematic view of the trigger plane scintillators E (top) and ΔE (bottom) plane. The side and lateral view of the trigger plane are shown below.

## 2.4 The Neutron Detector

Behind the BigBite spectrometer, we placed the Hall A Neutron Detector (HAND) with a matching solid angle. This detector was constructed from 112 scintillator bars distributed in six planes. During the production running the front plane of the detector was located 6 meters from the target. The scintillator bars were 100 cm wide and 10 cm thick. The total height of HAND was about 300 cm. The heights of individual scintillator bars were varied between 10 and 25 cm, due to detector availability. Because of their different heights, the bars were arranged in increasing height to match the acceptance of the BigBite spectrometer. The schematic view of the detector is shown in Figure 2.13.

In order to reduce the contribution from the charged particles that emerged from the target, a 1 inch lead wall was placed between BigBite and HAND. An additional plane of 64 thin scintillators with one side photomultiplier was placed in front of the neutron detector. This plane served for charged particle rejection.

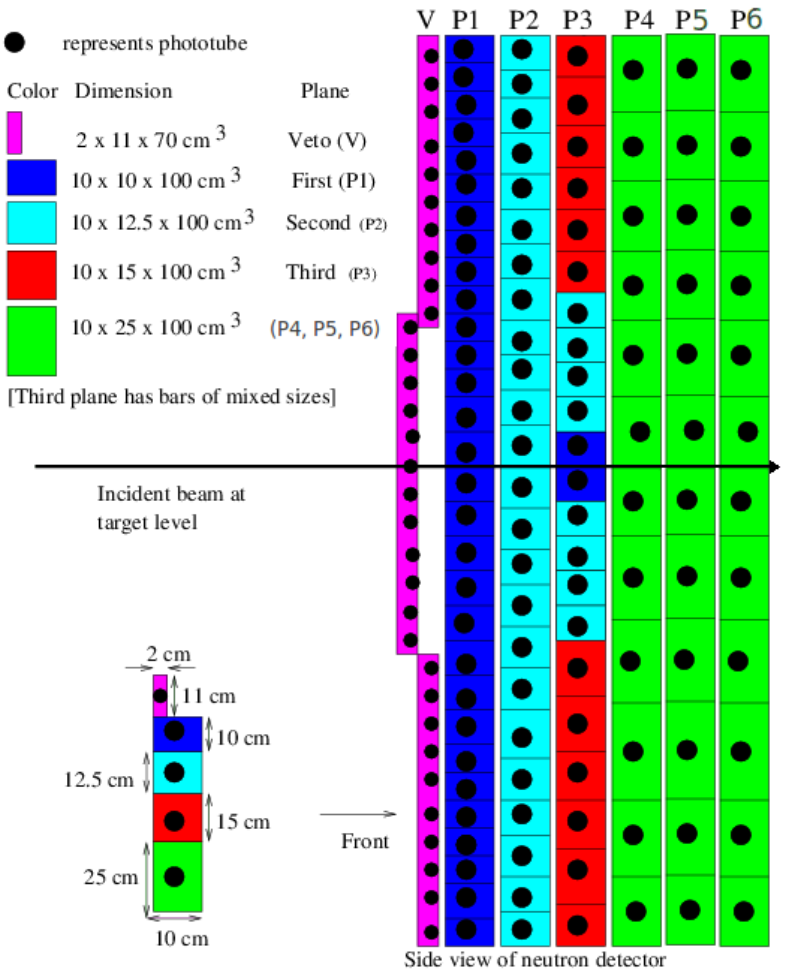


Figure 2.13: Schematic side view of HAND. The scintillators of different sized are shown with different colors.

The length, width and thickness of each veto paddle was 70 cm, 11 cm and 2 cm respectively. Because the veto bars each had a single side PMT, they were arranged in 32 rows of two paddles each, with a 30 cm overlap between them, see Figure 2.14:

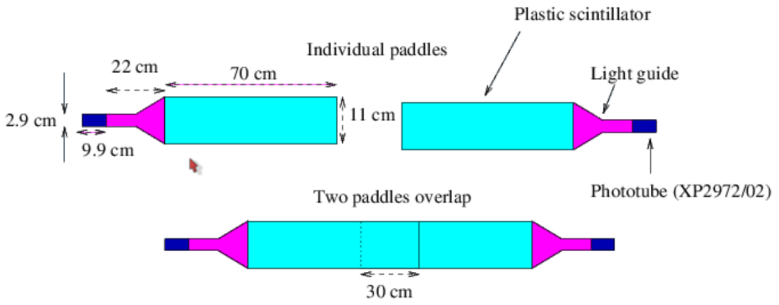


Figure 2.14: Front view of the veto bars and their arrangement. These are the detectors marked as "V" in Figure 2.13.

In thin paddles a charge particles can be easily detected, while the neutral particle does not deposit energy unless there is a nuclear interaction and even then they need to transfer enough energy to charged particle to be detected. This strong/weak response to charged/neutral particles allows us to use this plane as a veto plane for the first layer.

## 2.5 The Data Acquisition System (DAQ) and the off-line analysis.

The Data acquisition (DAQ) used the standard JLab software (CODA) [56]. This software records the data that has been digitized by the front end electronics. Some of the readout hardware units were custom made, such as the trigger supervisor module, F1-TDC and more. Other units were commercially acquired from CAEN, Phillips or LeCroy such as the Analog to Digital Converters (ADCs) and Time-to-Digital Converters (TDCs). In addition to the data, CODA also recorded information from the different diagnostic equipment such as the BCM, BPM etc. The TDCs and ADCs (front end modules) were housed in either VME or FASTBUS crates. Each such crate had a single board computer (SBC) running the VxWorks operating system. On each SBC, a CODA routine known as the ROC was running. This routine's function was to execute a corresponding readout list and arranged the data in a specific format after a trigger from the trigger supervisor was received. Afterwards, this data was passed to the other CODA components and eventually recorded on disk. Data taking was segmented into different files with a unique run number for each.

The offline analysis of the data was performed using the CERN ROOT software. The conversion of the raw data files recorded by CODA was done using a dedicated Hall A analyzer with extension libraries for BigBite and HAND. Some of analysis code (mainly for BigBite and HAND) was modified to take into account the requirements for this experiment.

## 2.6 Selecting events by the trigger setup.

Data acquisition systems are event rate limited to a rate that might be lower than the actual events (including the background) rate during the experiment. Because of this, the electronic triggers play a major role during the experiment enriching the data sample with "good" events. The trigger is an electronic signal that prompts the data acquisition system to start readout of the detector information. During this experiment we had several different types of triggers:

- T1 – The proton R-HRS event trigger.

- T3 – The electron L-HRS event trigger.
- T5 – The coincidence trigger defined as (T1 and T3).
- T6 – The BigBite trigger. This trigger was formed by making an "OR" between the different E plane bars ($\Delta E$ bars were not used in the trigger formation). The signal from individual bar was generated by "AND" between left and right PMTs (this trigger didn't started the DAQ because of its high rate. It was used only as on line monitor for scalers).

Additional triggers T2 and T4 were used and served to measure the inefficiency of the HRSs main triggers. These triggers are important for the absolute cross section measurements. Triggers T1 and T3 were formed in each HRSs by coincidence between the s1 and s2m planes. The logic diagram for these triggers is shown of Figure 2.15.

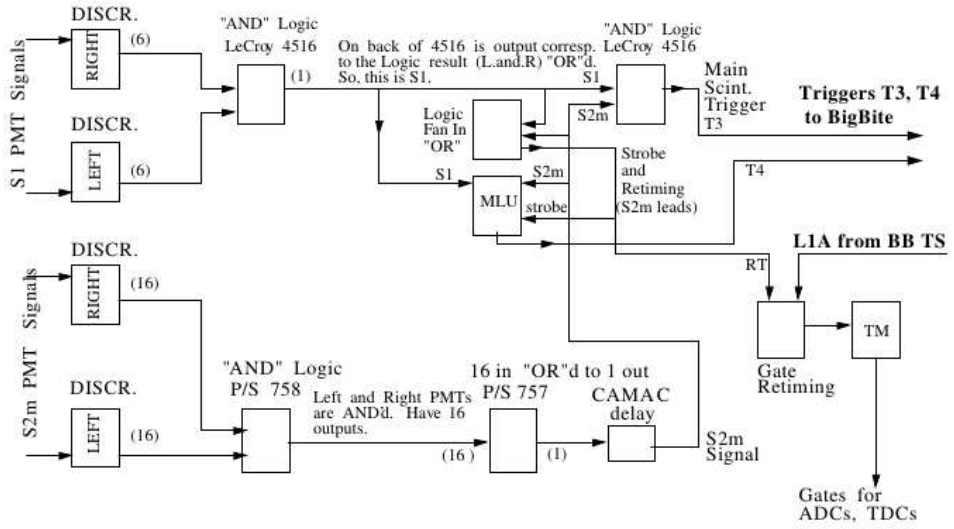


Figure 2.15: The electronic layout for the formation of the single L-HRSs trigger T3. Similar logic is applied for R-HRS.

The electronic layouts for the BigBite and HAND triggers are shown in Figures 2.16 and 2.17, respectively.

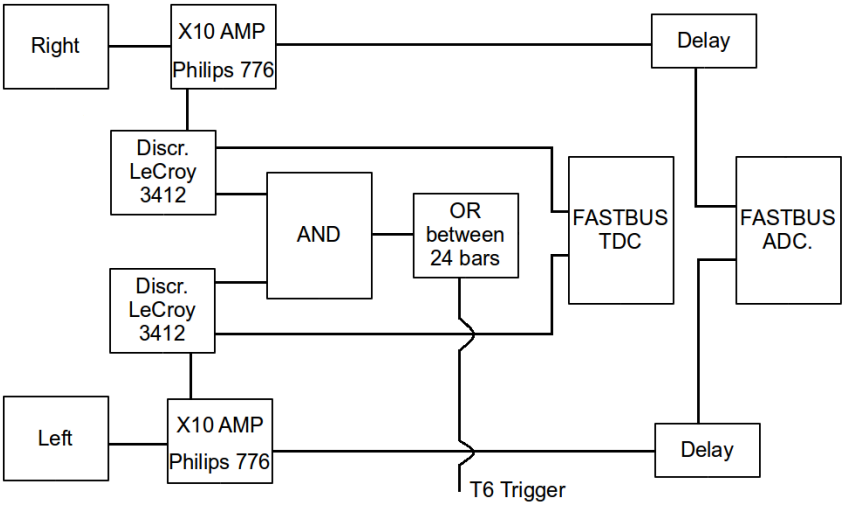


Figure 2.16: Electronic layout for BigBite spectrometer. The trigger is generated using the E plane bars.

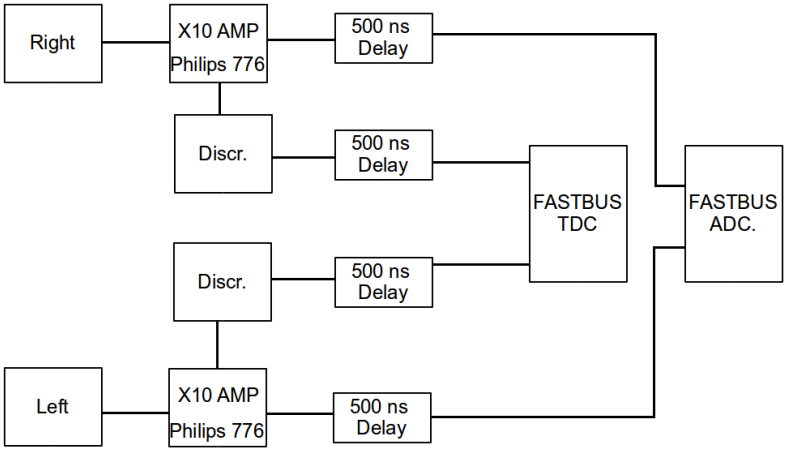


Figure 2.17: Electronic layout for each bar in HAND spectrometer.

The first trigger that arrived to the Trigger Supervisor defined the type of the event. The data that was read out from the front end electronics is marked with this event type. Most of the events were of type T1 (protons in the Right HRS) and type T3 (electrons in Left HRS). However in small fraction of the events we had type T5 events with both proton and electron detected in coincidence by the spectrometers. The electronics was set in such a way that if there was a T5 trigger type, it arrived first to the trigger supervisor so that the event was defined as a coincidence event.

T1 and T3 trigger types were mainly used for calibrations and stability checks, while the T5 was used to extract the triple coincidence events and to measure the various ratios.

## 2.7 Kinematics

In the experiment we used an incident electron beam of 4.454 GeV with a current of 4 $\mu$A. The target was 20 cm long cell mounted in the target chamber at the hall center. Scattered electrons were detected using the L-HRS at a central scattering angle and momentum of 20.3° and 3.602 GeV.

This corresponded to the quasi-free knock-out of a single proton with transferred three-momentum $\|\vec{q}\| \approx 1.64$ GeV/c, transferred energy $\omega \approx 0.86$ GeV, $Q^2 \approx 2$ (GeV/c)$^2$ and $x_B = \frac{Q^2}{2m\omega} \approx 1.2$, where $m$ is the mass of a proton. Knocked-out protons were detected using the right HRS which was set at 3 different central angles and momenta: 33.5° and 1.38 GeV/c, 29° and 1.3 GeV/c, 24.5° and 1.19 GeV/c.

In this thesis we define three experimental setups that correspond to central missing momentum of the knocked-out proton, 500 MeV/c, 625 MeV/c, and 750 MeV/c. Each of these kinematic conditions are set by the variation of the central momentum and angle of the R-HRS that detected the scattered proton. For the first two settings the BigBite spectrometer and HAND were positioned at 97° and for the third setup at 92°.

Its worth noting, that for calibration of right HRS (offset etc.) and for HAND efficiency measurements we changed the polarity of the HRSs i.e. the left HRS detected protons and the right HRS detected electrons. In this thesis, this configuration is called "$x_B < 1$ settings".

Figure 2.18 show a diagram of the layout of the experiment

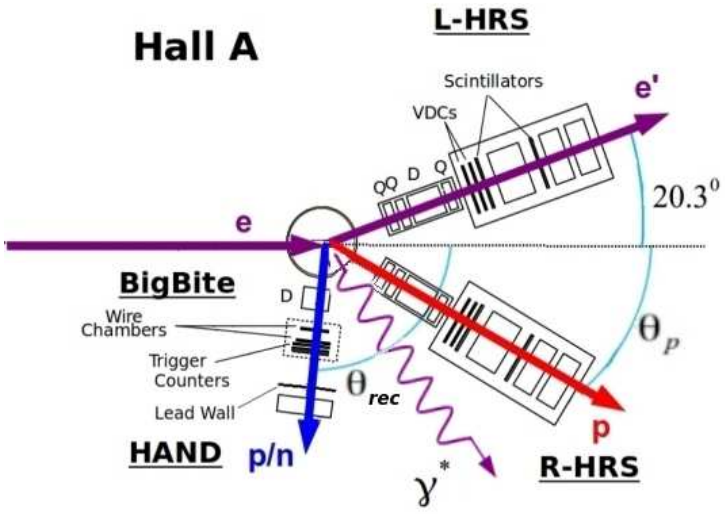


Figure 2.18: A diagram of the layout of the experiment. The electron kinematics were fixed and the proton angle and momentum were varied. In the background, the various detectors with their magnets and their main systems are shown.

# Chapter 3

# Data Analysis

## 3.1 Data Analysis

Data analysis was done using the CERN/ROOT software [57]. The conversion of the raw data recorded by the CODA software to the standard tree structure used by ROOT is done with the Hall A analyzer software [58]. In addition to the generation of the standard ROOT trees, the analyzer also calculated basic physical quantities such as hit positions, momenta, path length of the particles etc. In order to convert the raw data to physical quantities, data base files are provided. These data base files store the information needed to remove various offsets such as cable lengths, corrected for electronic delays constants, introduce calibration parameters, and similar information. In this chapter, we described the calibrations that were done for the detectors that were used during the experiment. Each detector requires different calibrations to extract the physical quantities of interest from the raw data. In this thesis the uncertainties presented are one standard deviation except if stated explicitly otherwise.

## 3.2 HRSs

Coincidence between the Right and Left High Resolution Spectrometers (HRSs) defined the main $(e, e'p)$ trigger for the data taking. During this analysis the reference time for all detected particles is the electron detection in the s2m plane of the HRS. All the time-of-flight (TOF) that are presented in this thesis are defined as a time difference between the signal in the relevant detector and the electron reference time. Corrected TOF calculated based on the measured TOF minus the correction based on the momentum and path length of the electron and proton (neutron) in BigBite (HAND). Absolute time that calculated in the thesis is in respect to the reaction time. If different definition is used, it is stated explicitly.

### 3.2.1 TDCs

The TDC units used to record the time in both HRSs were 1877 LeCroy with 0.5 ns time resolution [59]. These TDCs have multihit capability and allow the measurement of up to 16 hits separated by 20 ns or more. We only used 6 hits.

The data acquisition mode for these TDCs was "common stop" in which each TDC channel generated a start and a delayed trigger signal defined a common stop.

For each HRS the scintillators of the s2m plane generated a timing signal. The s2m plane in each

HRS is made of 16 different paddles. Different cables length and delays create offsets between the timing signals created by particles that arrived simultaneously. The first calibration procedure was to determine software offsets to compensate for these TDC offsets.

The calibration was done by looking at electrons detected in the HRS (for HRS left we used the $x_B > 1$ settings, and for R-HRS we used the $x_B < 1$ settings). For the calibration, we used the TOF between the s1 and s2m planes corrected using the path length and reconstructed momentum (the momentum and path length were calculated from the VDC information). In Figure 3.1 the TOF between s1 and s2m before calibration is shown as a function of the s2m paddle number. The different s2m paddle offsets can be clearly seen. In Figure 3.2 the same quantity is shown but after the offset calibration. In Figure 3.3 the projection on the TOF axis is presented. As can be deduced from Figure 3.3 the TOF resolution was about 0.6 ns.

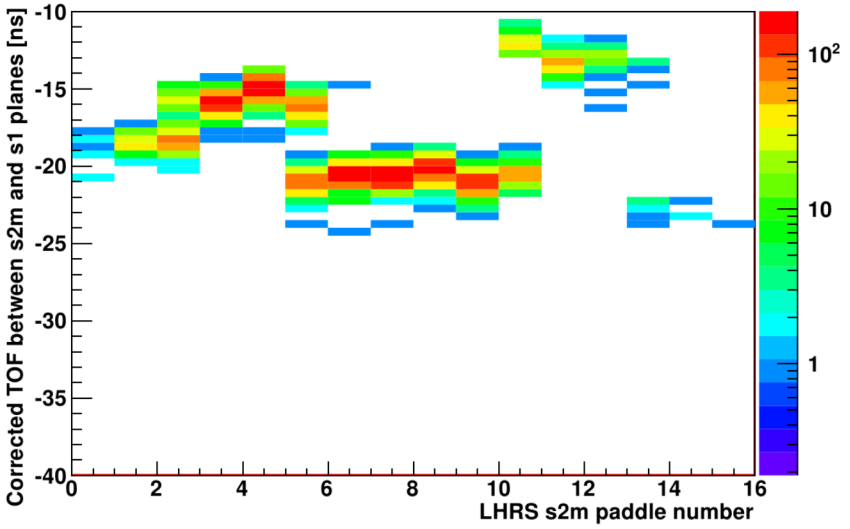


Figure 3.1: TOF of electrons between s1 and s2m in L-HRS corrected for the path length. The TOF shown is before the TDCs offset calibration.

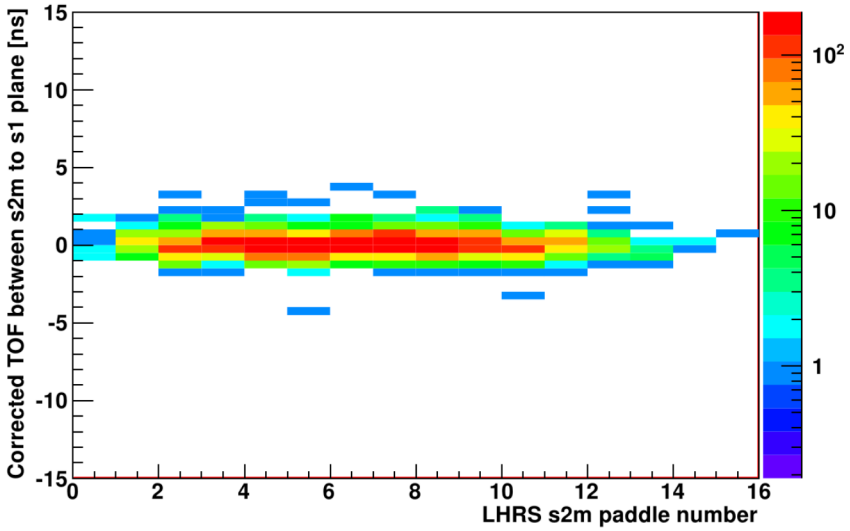


Figure 3.2: TOF between s1 and s2m planes after the TDCs calibration.

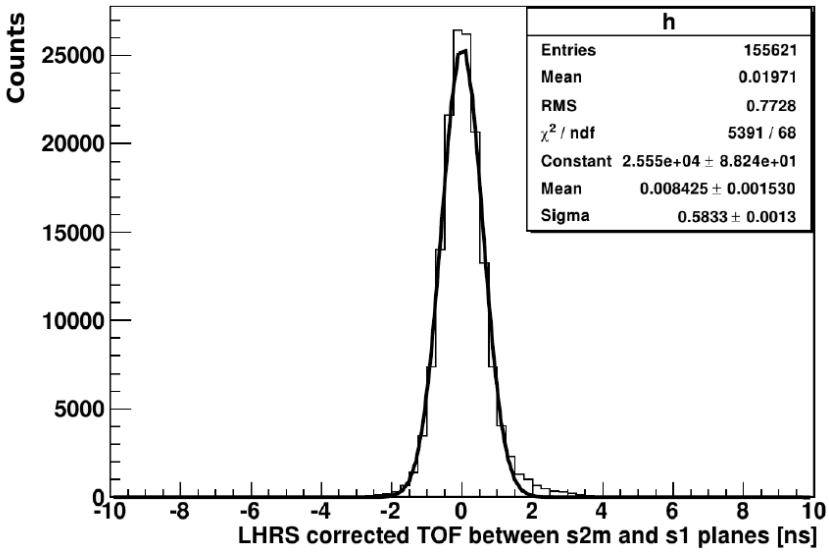


Figure 3.3: The resolution of the TOF after the calibration.

### 3.2.2 VDCs, optics, and momentum reconstruction.

Reconstruction of the momentum and the interaction vertex of the detected particles is done using the VDC's information. Using the transformation matrix, hits on the focal plane in each HRS can be transformed to position and angle at the target. The goal of the optical calibration is to determine the values of these transformation matrix elements.

The calibration of the matrix begins by using the optics target. The optics target is a set of multiple thin foils of $^{12}$C (13 for our setup) positioned at the center of the scattering chamber. The size and position of the foils relative to the HRS are precisely measured. In Figure 3.4 vertex reconstruction is presented while the actual foil position is marked with red triangles.

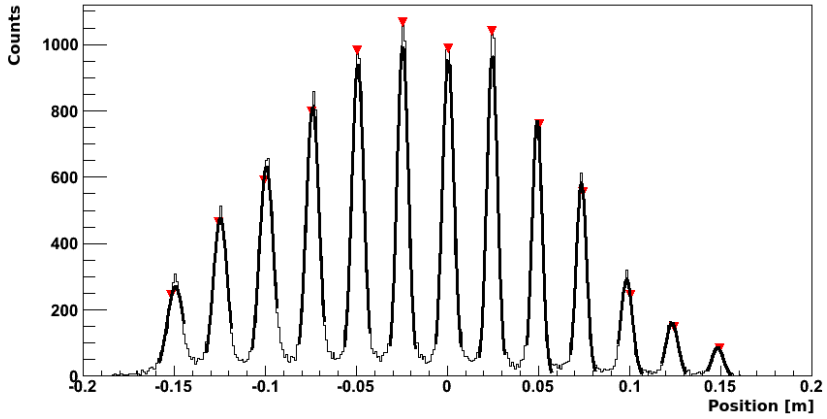


Figure 3.4: The reconstructed position of the 13 thin Carbon foils of the optical target. The expected position of each foil is marked by a red triangle.

During the calibration, matrix elements were varied to get the best agreement between reconstructed and known positions.

The matrix elements responsible for reconstruction of the in-plane and out-of-plane angles are calibrated using events scattered from a thin Carbon target that passed through a sieve slit plate

inserted at the entrance of each spectrometer. In Figure 3.5 the sieve slit reconstruction is shown. The hole locations are known from the spectrometers survey.

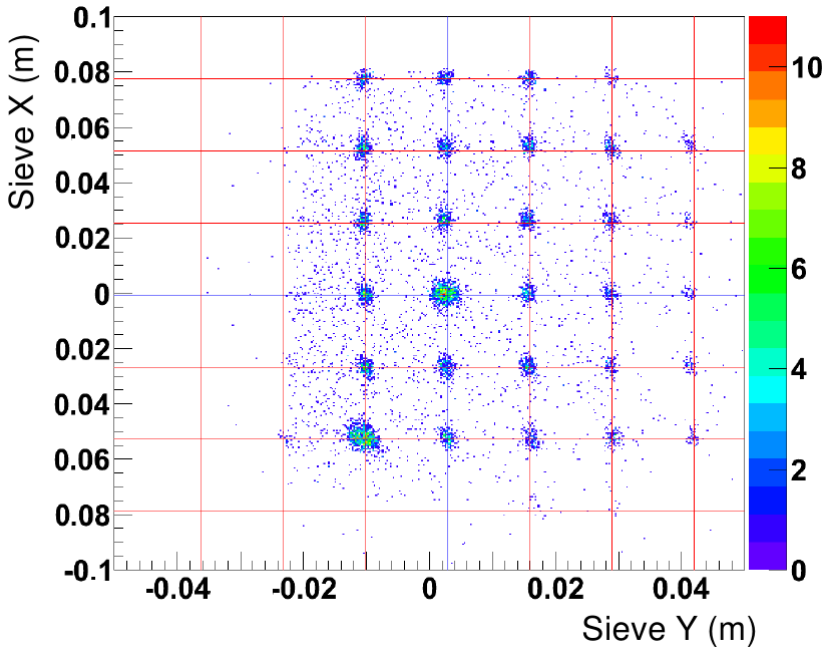


Figure 3.5: Example of reconstruction with a sieve slit in the L-HRS. The intersections of the red lines represent the expected positions as measured by the survey group.

The last set of matrix parameters for the momentum were calibrated using elastic scattering from a thin Carbon target.

An additional calibration test was done using elastic scattering from a Hydrogen target for different central momentum values of the spectrometer. In Figure 3.6 the elastic strip (correlation between the in-plane scattering angle and the momentum of the scattered electron from elastic scattering process) for different elastic kinematics setups is shown.

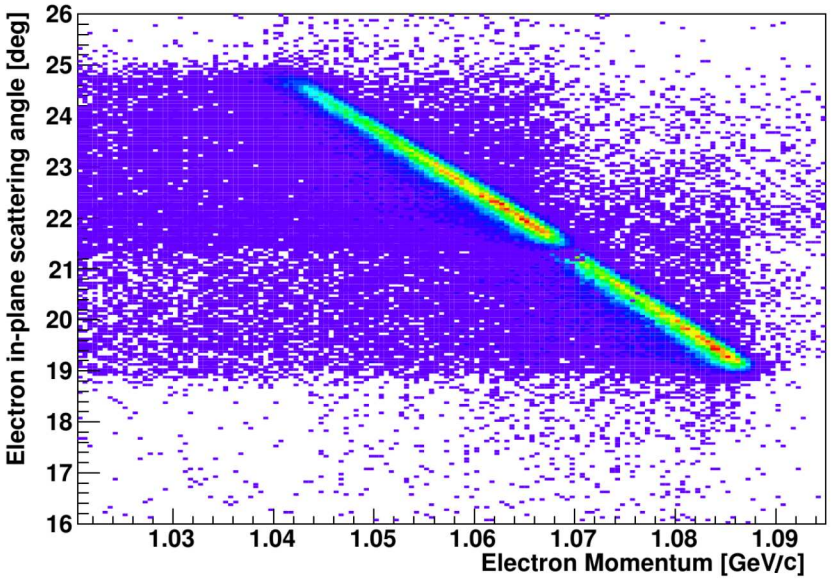


Figure 3.6: Reconstruction of the in-plane scattering angle versus electron momentum for elastic scattering events. The gap between the two strips is due to the momentum coverage of the HRS settings.

Following the TDCs and optical calibrations, the detected particle can be identified. In Figure 3.7 the R-HRS corrected TOF (between s1 and s2m planes and obtained assuming a particle with the proton mass) is shown. Pions, protons and deuterons can be clearly identified.

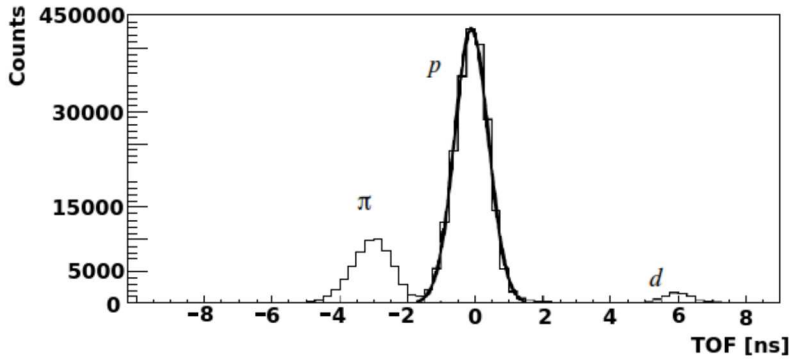


Figure 3.7: A typical TOF (time-of-flight between s1 and s2m planes corrected to proton mass and path length) distribution in R-HRS as obtained during the calibration runs.

During the production runs the fraction of reconstructed tracks from multihits events (multihit in TDCs and multi bar hits) that passed the trigger and the cuts in the spectrometers was less than 0.5% see Figure 3.8.

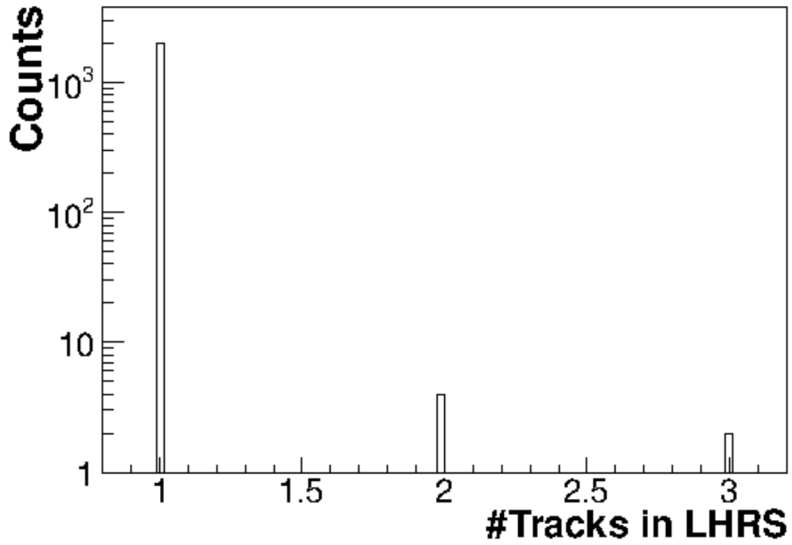


Figure 3.8: Number of reconstructed tracks in LHRS after applying all $(e, e'p)$ cuts (see chapter 4.2 for details).

## 3.3 BigBite

Most of the calibrations for BigBite were done using the two body H$(e, e'p)$ reaction with the elastically scattered protons detected by BigBite and the electrons by one of the HRSs. The elastic scattering events were used mainly to calibrate the momentum reconstruction from the MWDC information and to determine the absolute detection efficiency for protons. Some relative calibrations were done during the production (due to the timing issues that are described in appendix A).

### 3.3.1 ADC/QDC

For the BigBite spectrometer, CAEN 792 QDC modules were used to record the pulse heights due to energy deposited by particles in the BigBite scintillators. The QDC calibration is needed to remove pedestals and align all QDC signals of equal strength to allow particles identification.

Following the pedestal calibration, the gain parameters for E and $\Delta$E planes were varied in order to match the proton's "punch-through" point, point which corresponds to proton with enough energy to pass through whole detector for all the E counters. This was done by first varying the high voltage for the PMTs in order to increase (or decrease) the gain, following by a fine gain corrections by software.

In Figure 3.9, the two dimensional scatter plot shows the energy deposited in $\Delta$E vs E plane, after the QDC's calibration.

Due to the small thickness of the $\Delta$E scintillators, the high momentum protons generate a small signal. The particle ID was therefore done by using energy deposit in E plane and the reconstructed momentum in the MWDCs.

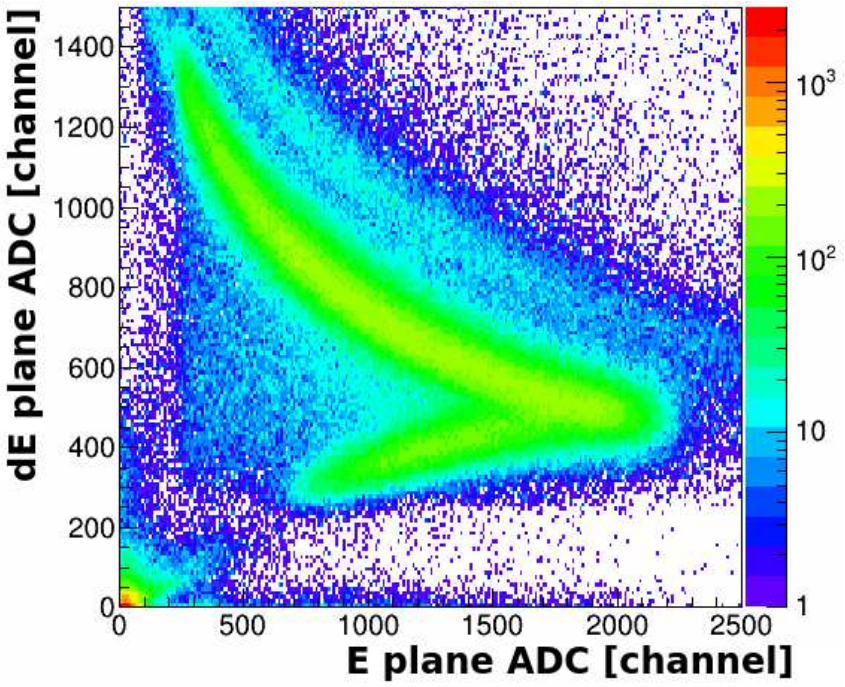


Figure 3.9: Energy deposit in ΔE plane vs E plane. Protons are clearly identified by their energy deposit. With the increase of the protons momenta the energy deposited in ΔE plane decrease while the energy deposit in E plane is increase up to the punch through point, point were protons have enough energy to penetrate both planes. For protons with higher energy deposit in both plane gradually decrease with the increase of the protons momentum.

### 3.3.2 TDC

The TDC information from the BigBite trigger plane was recorded using CAEN 1190 multihit TDCs that have time resolution of 100 ps [60]. However, the time resolution was limited to 500 ps due to the 1877 TDC [59], used to reconstruct the retiming signals in HRSs and trigger supervisor unit (see appendix A for details).

In order to compensate for different wire length and electronic offsets, the relative timing between the E and ΔE bars was adjusted by using particles that hit both a E and a ΔE. This is possible because of the shift between the planes that create 4 cm overlap between bars. The drawback of the method is accumulative error after each iteration due to the final resolution of each time measurement. In order to overcome this, the calibration was started from the center of the detector (and not from top or bottom) and in addition elastic scattering events were used to correct for the accumulated error and to introduce a global offset. Simultaneously with the TOF calibration (using elastic scattering), a position calibration was also performed. In Figure 3.10 a typical position distribution and a TOF distribution are shown:

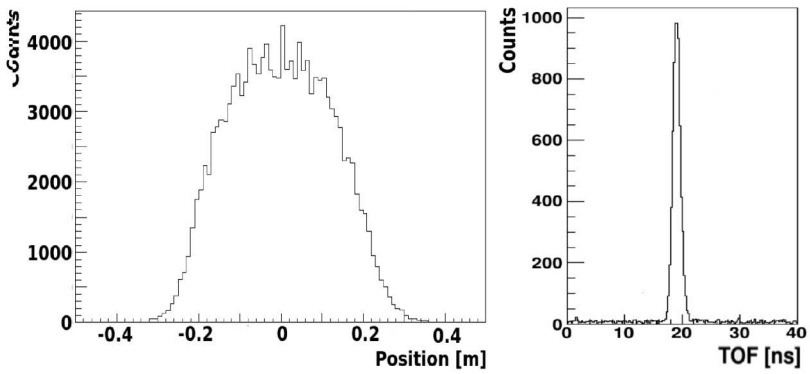


Figure 3.10: Reconstructed position distribution of charged particles in an E plane bar (left) and TOF of elastic protons (right) after the TDC calibration.

### 3.3.3 Wire Chambers

The position information from the MWDC is generated from signals induced on the wires and recorded by 1877 TDC units (same as for the HRSs). These signals are used to determine the drift time of charged particles between the position the particle hit the chamber and the wires, similar to the VDCs in HRSs. The signals from the different wires have offsets due to different cable lengths. The extraction of the hits locations is done by converting the drift time to distance, so the starting time (or stop time) for all wires must be aligned in order to convert time to distance with the same parameters for all wires. The alignment of the signals was done by adjusting the $T_0$ parameter, that stands for starting drift time in the MWDC, see Figure 3.11.

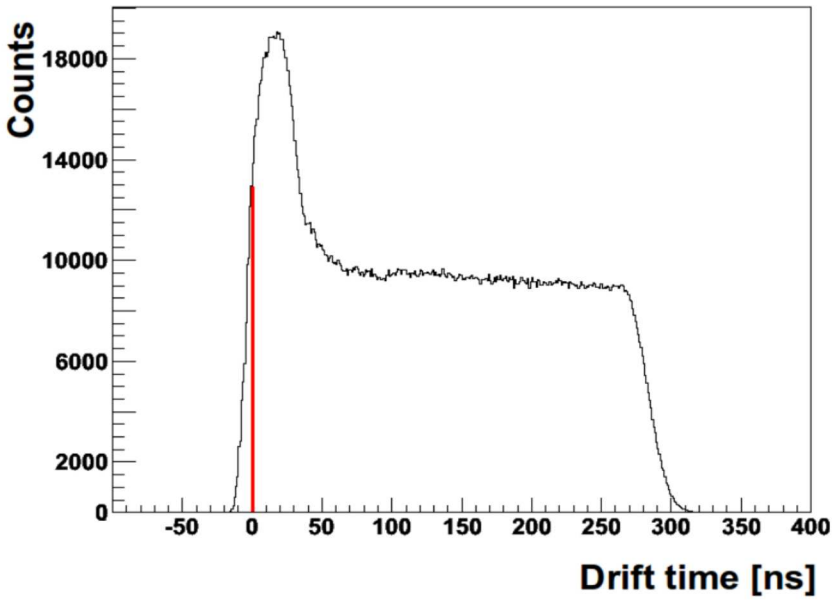


Figure 3.11: A typical distribution of the drift time.

The commissioning of the BigBite with the MWDC, done prior to this experiment, included an intensive study of the chambers and calibration of the actual wire spacing and time to distance conversion. For the current experiment, the parameters and the conversion constants used are those based on that study [54].

### 3.3.4 Momentum / optics

Physical quantities such as the momentum of the particle, the hit position, the path length etc. are reconstructed using the MWDC information. Reconstruction of these physical quantities is based on an analytic calculation of the curvature of the particle trajectory in the magnetic field.

The information that must be supplied for this calculation is the geometry of the magnet, the characteristics of the magnetic field, and the position of the magnet in the Lab coordinate system. Figure 3.12 shows a photograph of the magnet and a drawing of the simulated magnetic field.

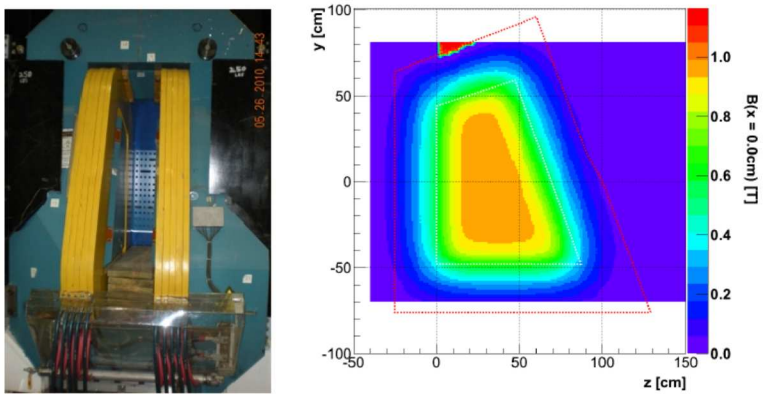


Figure 3.12: Photograph of the BigBite magnet, taken from its back side (left) and the simulated magnetic field of BigBite in the mid-plane of the magnet (Right).

The magnet was surveyed by the survey group during the experiment setup. The result of this survey was introduced as geometrical constants that were added to the data base file used by the analyzer software.

After the geometrical constants were supplied, a calibration of various offsets was done using elastic scattering H$(e, e'p)$ and comparing the expected momentum and angle based on the electron information from the L-HRS. In Figure 3.13, the proton's reconstructed momentum is shown versus the expected momentum, as calculated from the electron measurement.

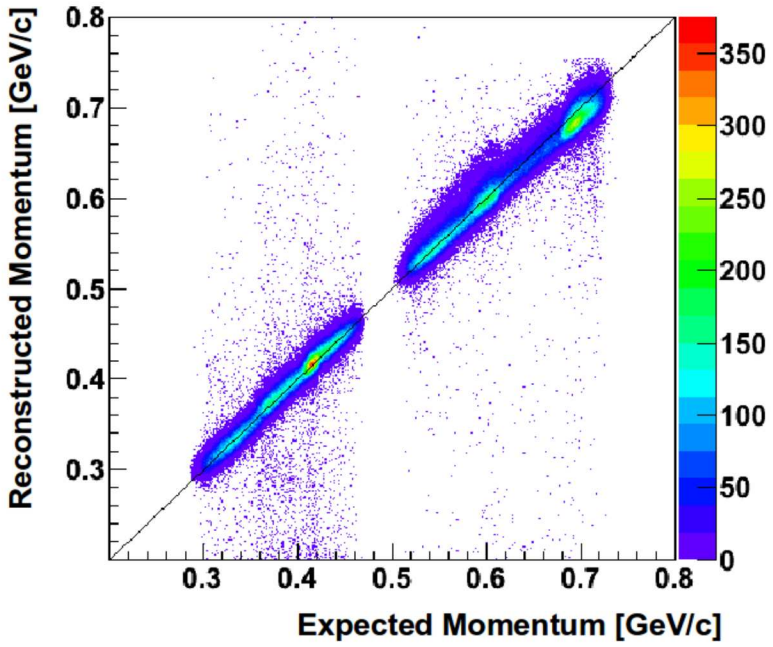


Figure 3.13: Reconstructed momentum in BigBite vs expected momentum (elastic scattering on Hydrogen).

The momentum resolution for BigBite ($\Delta p/p$) is about 1.5% (one standard deviation). In Figure 3.14 two measurements of the momentum resolution are shown:

Left: Resolution is $\frac{\Delta p}{p} \approx \frac{6.7}{450} \approx 1.5\%$ for $\sim 450$ MeV/c protons.

Right: Resolution is $\frac{\Delta p}{p} \approx \frac{10}{650} \approx 1.5\%$ for $\sim 650$ MeV/c protons.

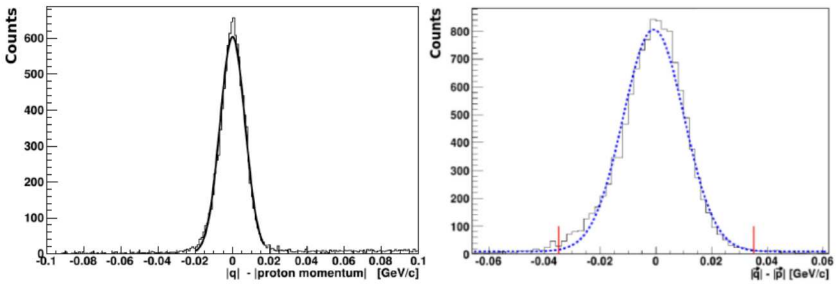


Figure 3.14: The difference between the momentum transfer in H$(e, e'p)$ and the measured momentum in BigBite. Momentum resolution determined by elastic scattering with protons having momentum of 450 MeV/c (left) and 650 MeV/c (right).

### 3.3.5 Proton ID

Particle identification (ID) in the BigBite spectrometer was done in two ways. The first method uses the energy deposited in the E plane and the reconstructed momentum in the MWDC. The 2D plot of these quantities shows a clear bands for protons, deuterons, and minimum ionizing particles (including noise), (see in Figure 3.15).

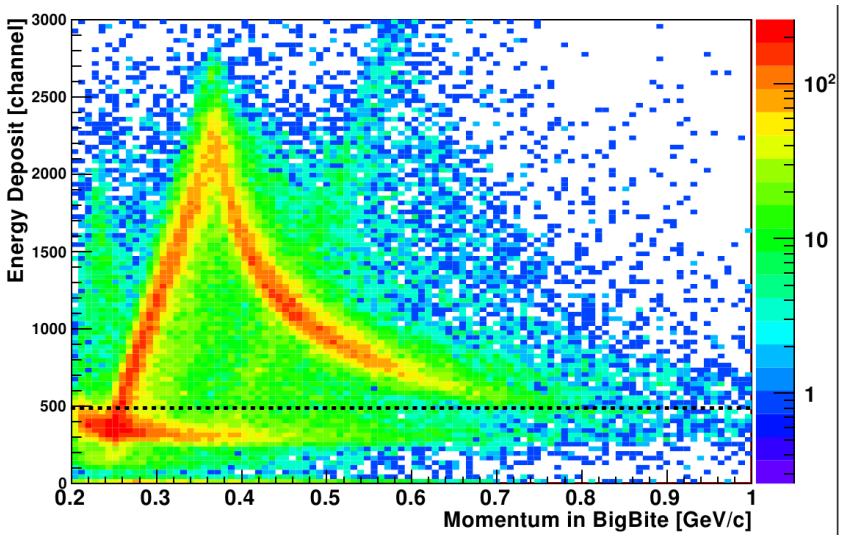


Figure 3.15: Energy deposited in the E counters vs reconstructed momentum in BigBite. Below the horizontal dashed line minimum ionizing particles and bad momentum reconstructed tracks are located.

The second method utilizes the corrected TOF. We calculate the difference between the measured TOF and the expected TOF assuming the mass of the proton. We expect this corrected TOF difference to be centered around zero. For heavier or lighter particles the TOF difference is non zero (example on Figure 3.7).

### 3.3.6 Multi hits and hits matching

For each event, there are multiple tracks in the MWDC and multiple hits in the trigger plane scintillator bars. As shown in Figure 3.16 for most of the events more than one bar produces a signal. There are also approximately 2.5% of the events with more than 1 hit in the same bar (see Figure 3.17).

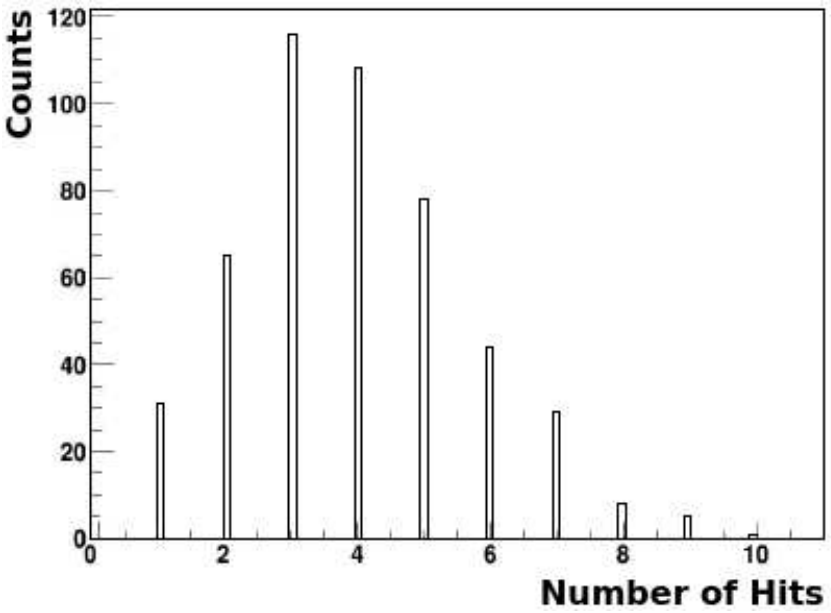


Figure 3.16: Number of E counter hits per event during the elastic scattering run.

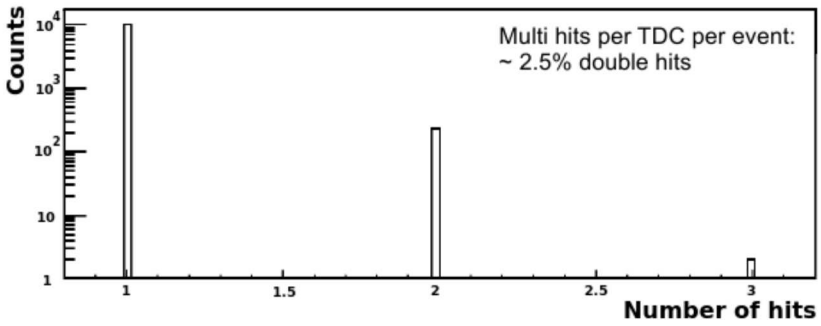


Figure 3.17: Number of hits per event in each E counter.

Figure 3.18 shows, the difference between the position measured by MWDC and the position based on the scintillator's time measurement. The width of this distribution defines the resolution within the MWDC tracks and the hits in the Trigger plane can be matched.

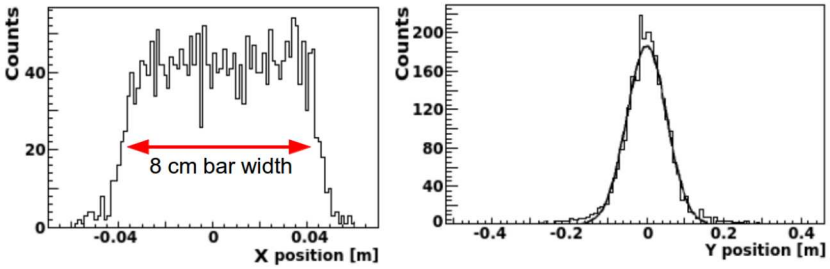


Figure 3.18: Difference between hit position on the E plane as reconstructed based on the MWDC and as reconstructed based on the E plane information. The left figure is for the dispersive direction and the right figure is along the scintillator bar.

For each track, we checked if there was a E or $\Delta$E bar located inside the region defined by the resolution of the track. If there was a legitimate match, the track was recorded.

After the hit matching, the number of multiple protons in each event was reduced to $\sim 2\%$.

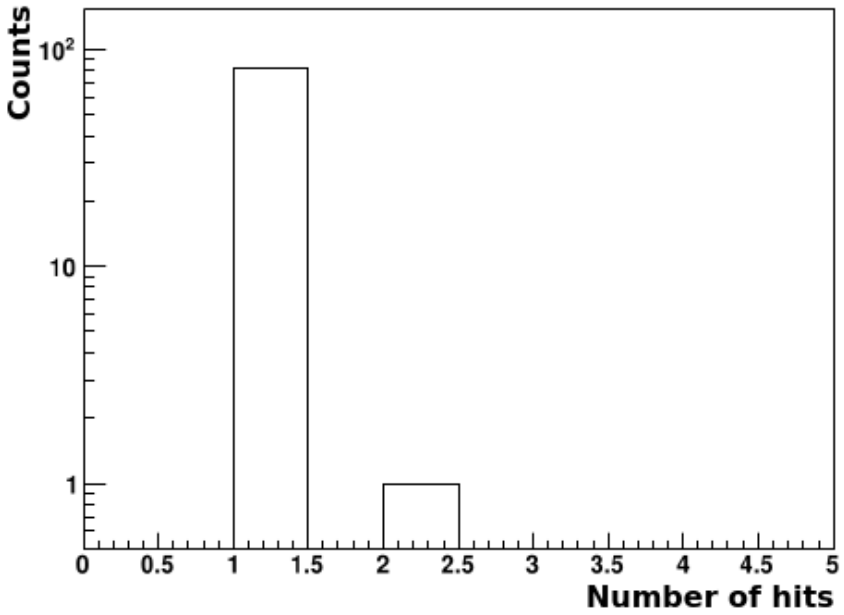


Figure 3.19: Number of reconstructed tracks with a matching hit in the E plane (data is from the 750 GeV/c settings).

### 3.3.7 The proton detection efficiency in BigBite

The BigBite detection efficiency is determined by the efficiency of the Trigger Plane (TP) scintillators and the efficiency of the MWDC.

The TP in BigBite is composed of scintillator bars with very high detection efficiency (close to 100%) for charged particles. The efficiency of the MWDC is lower.

The absolute efficiency of BigBite was determined using low intensity elastic runs where we know how many protons should reach BigBite based on kinematical considerations. These measurements gave an efficiency of $\sim 98\%$.

During the production measurements, the singles rate was increased to 1 MHz, compared to only 50 KHz during the elastic runs. The two orders of magnitude change in singles rates did not affect the efficiency of the scintillators but it drastically reduced the overall efficiency of the BigBite. This is mostly due to the inefficiency of the tracking algorithm for the MWDC at high rates.

The determination of the efficiency during the production runs was based on the measurement of the $^4$He$(e, e' p_{\mathrm{recoil}})$ reaction. The TOF peaks with and without the requirement of the MWDC are shown in Figure 3.20. The efficiency of the MWDC was determined by the ratio of the number of events in these peaks. Combining this result with the efficiency of the TP, yields the overall efficiency of BigBite for proton detection.

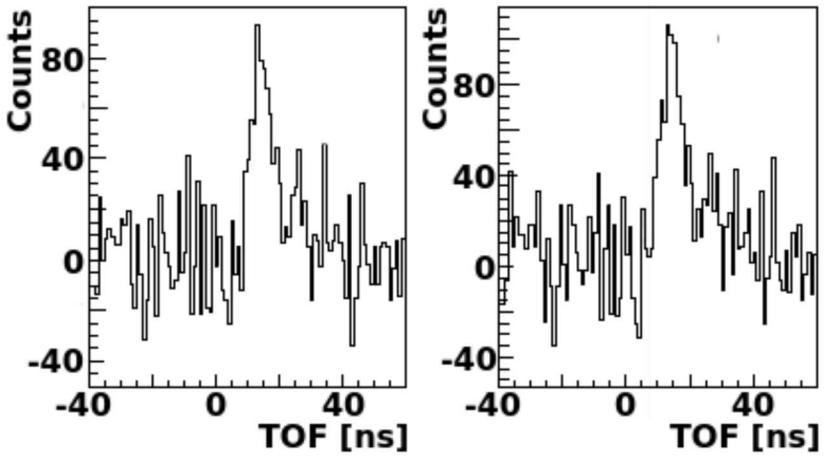


Figure 3.20: Background subtracted TOF distributions for protons in BigBite. Left figure represents TOF with track in the MWDC and right figure represent the TOF without requesting a track in the MWDC.

To check the stability of the detection efficiency we divided the production period into sequential groups of runs and determined the efficiency of BigBite for each group. Figure 3.21 shows the efficiency of MWDC as a function of time during the production data taking runs.

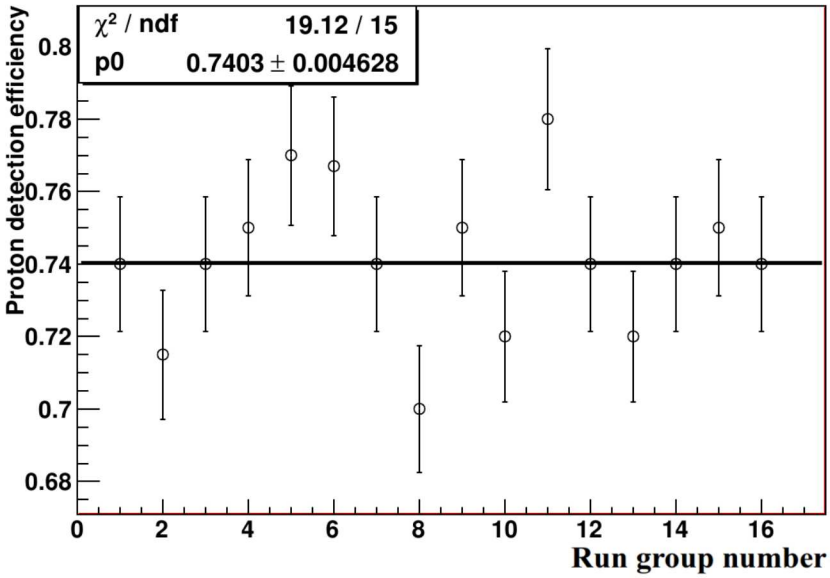


Figure 3.21: Proton detection efficiency of the MWDC during the production period. The run period was divided into groups of 20-25 runs (presented in chronological order).

As the MWDC efficiency showed no dependence on time, a constant overall BigBite efficiency (including trigger plane efficiency) of 73±1% was assumed.

The same efficiency determination was performed using the $^4$He$(e, e'pp)$ events, however the statistics of the triple coincidence events is very low so the measurement was done for the entire production period as one group with a large statistical uncertainty. The MWDC efficiency as determined in this measurement was $77 \pm 6.5\%$.

## 3.4 HAND

In the neutron detector all the physical quantities are derived from the absolute TOF of the detected particles. For each photomultiplier (two per bar) we recorded the information in a TDC and an ADC. The ADC information was used to determine the threshold (which impacts the absolute neutron detection efficiency), and for the "time-walk" correction that improves the time resolution (see Chapter 3.4.3).

The BigBite TOF distributions can be corrected by using the momentum and the path length of the detected particle known from the MWDC information. This is done in order to improve the signal to random background ratio. In HAND we use only the TOF spectra to reconstruct all physical quantities. Except during the full exclusive scattering from the Deuterium target, momentum and path length correction are not possible.

### 3.4.1 ADC calibration and threshold determination

The energy deposition in the HAND scintillators was recorded using LeCroy 1881M ADC FASTBUS units [61]. Similar to the calibration done for BigBite, all pedestals were aligned to zero. Figure 3.22 shows pedestals before and after the alignment.

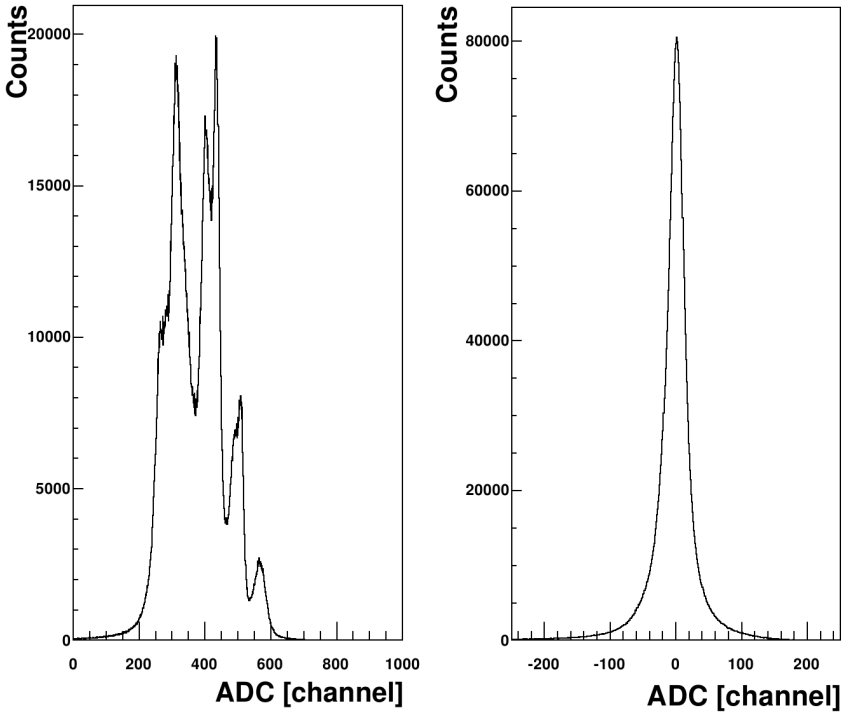


Figure 3.22: Pedestal distribution of HAND's first layer scintillators. Left: before pedestal alignment, Right: after.

To calibrate the ADCs, elastic scattering H$(e, e'p)$ events were used. HAND was placed 15 m from the target and the L-HRS was tuned to detect electrons that are accompanied by $\sim 1$ GeV/c protons in the HAND direction. The kinetic energy of these protons was sufficient to punch-through 65 cm of plastic scintillators.

The light production of a proton in the scintillators is converted into "electron equivalent", MeVee. This conversion is needed because the relationship between energy loss and light production is linear

for electrons but for heavier particles it is non-linear, and unique to the particle species. The conversion is done by Eq. 3.1 [62]:

$$T_E = -8 \cdot e^{-0.1 \cdot T_p^{0.9}} + 0.95 \cdot T_p \tag{3.1}$$

where $T_p$ and $T_E$ are the energy deposited by protons and electrons both in MeVee. The light production is different for different layers due to different energy loss of the protons in the proceeding layers. The energy deposition is summarized in Table 3.1:

| Layer | Proton Kinetic Energy [MeV] | Energy Deposit [MeVee] | ADC channel |
|---|---|---|---|
| Veto | 480 | 11 | 660 |
| 1 | 469 | 27 | 1620 |
| 2 | 442 | 28.5 | 1710 |
| 3 | 413 | 29 | 1740 |
| 4 | 383 | 30 | 1800 |
| 5 | 353 | 32 | 1920 |
| 6 | 320 | 33 | 1980 |

Table 3.1: Energy loss in HAND counters

The calibration of the ADCs using the known proton energies from elastic scattering is needed to determine the threshold value in MeVee. The threshold affects the absolute neutron detection efficiency. Contrary to charged particles, neutrons deposit a broad range of energy in scintillators, between zero and the full kinetic energy of the neutron. Setting the peak of the elastic protons at the ADC channel as shown in Table 3.1, means that 5 MeVee corresponds to ADC channel number 300. In Figure 3.23 the energy deposition for elastic protons is presented.

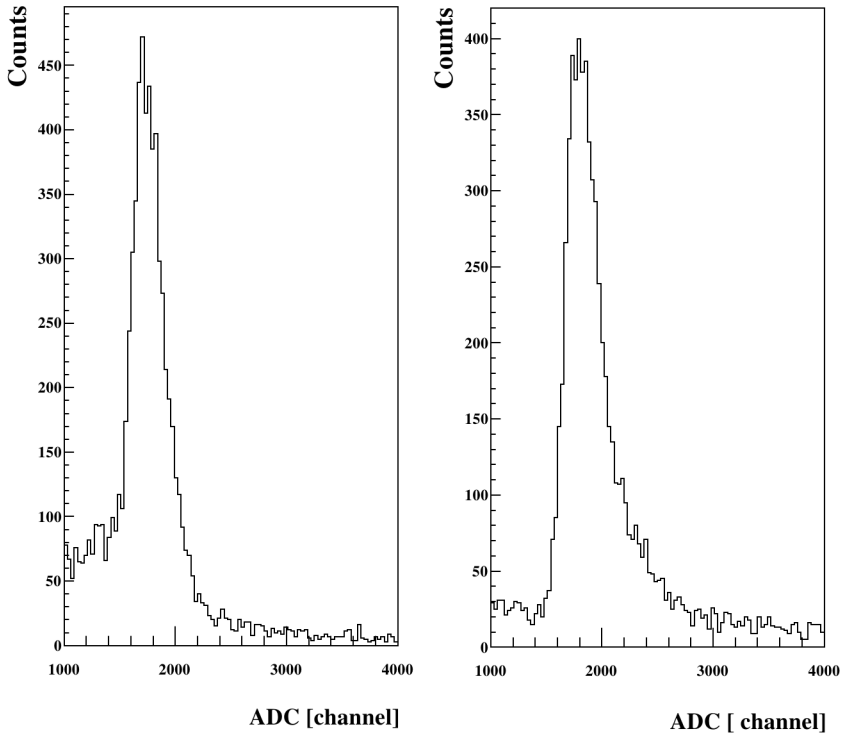


Figure 3.23: ADC distributions for elastic protons in layer 1 (left) and in the fourth layer (right). Shift in the ADC peak position is clearly seen in agreement with the expected value.

In addition to the software threshold set at ADC channel 300 as described above, there was a hardware threshold determined by the HV and discriminator levels. The choice of value for the hardware threshold is made by taking into account the efficiency and the background level. High levels will reduce the background but also the absolute efficiency.

The hardware threshold is defined by the beginning of the drop in the ADC distribution caused by requiring a TDC signal. In Figure 3.24 the ratio of ADC signal with/without TDC signal is shown.

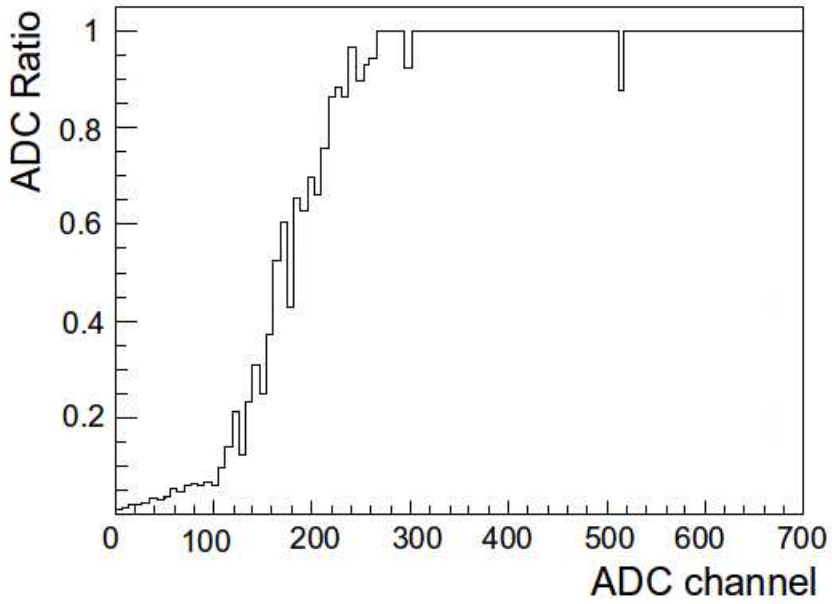


Figure 3.24: Hardware threshold. Ratio between number of events with TDC requirement to total number of events, plotted vs ADC channel number.

In Figure 3.25 the thresholds for the second layer bars are shown.

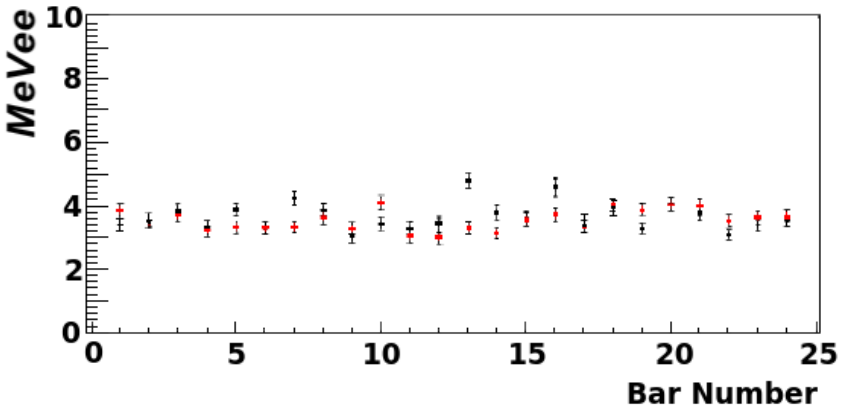


Figure 3.25: Example of the hardware thresholds values for the scintillator bars in the second layer. Red points represent the left side PMTs and black represent right side.

The hardware level that was set on the discriminators was 30 mV (the minimum threshold for these discriminator type is 15 mV). The hardware threshold in MeVee was controlled by changing the HV.

### 3.4.2 TOF calibration.

Since all the physical quantities of the neutrons are derived from the TOF, the absolute calibration of the time measurement and its resolution are crucial.

The time calibration was done using two methods. The first one is a calibration using cosmic muons. In this method, a cosmic particle path between the upper and lower bar in the same plane are used to calibrate the TDCs of all bars with respect to the upper bar. This procedure include the correction to travel time of the muons between the bars. In the second technique, elastic scattering from Hydrogen target, H$(e, e'p)$, was used to aligned measured TOF from all bars with respect to the reaction time.

For this calibration, we moved HAND 15 meters away from the target at 50°.

During this experiment, the last method was used to align all bars to the same time and the calibration with muons was only for a consistency check.

The absolute time calibration of the HAND detectors was done using the H$(e, e'p)$ reaction.
The chosen kinematics for the H$(e, e'p)$ time calibration was:
Beam energy –2.257 GeV LHRS – 1.775 GeV / 27.5°
The momentum of the elastic protons was 1.067 GeV/c. As mentioned in the previous section this momentum allows protons to punch-through 65 cm of plastic scintillators.

For these protons with known momentum the TOF in respect to reaction time is given by Eq. 3.2:

$$TOF = 0.25 \cdot (T_L + T_R) - \frac{\text{path}_{\text{electron}}}{0.3} - \frac{\text{path}_{\text{proton}}}{\beta \cdot 0.3} \tag{3.2}$$

where $\beta$, is the known velocity of the proton, path lengths are in meters, and 0.3 $\frac{\text{m}}{\text{ns}}$ is approximately the speed of light.

In Figure 3.26, as an example, the TOF of one scintillator bar. The resolution (before pulse height correction) is poor $\sigma \approx 1.2$ ns. This poor resolution is due to the combination of the TDC resolution, TOF resolution of the L-HRS, and the resolution of the signal used for the common stop (see appendix A for details).

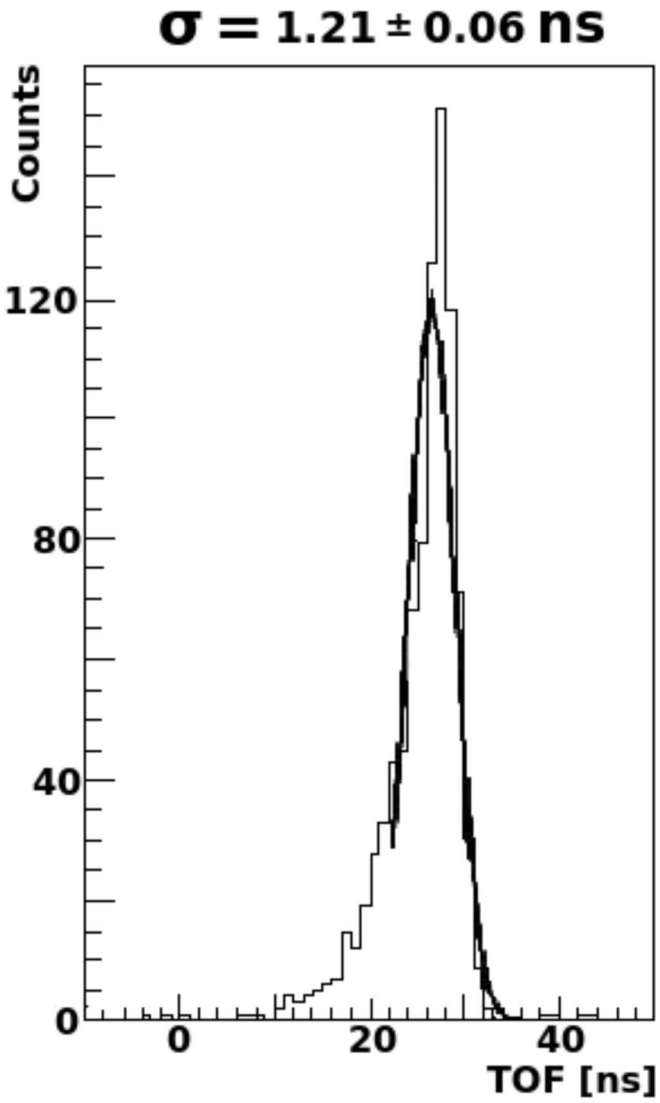


Figure 3.26: TOF distribution of a single bar from layer 5.

### 3.4.3 Time Walk correction

To achieve the best possible resolution, pulse height information is used in order to correct the shift in the measured time due to the pulse size. Notice that the time resolution is limited to 0.5 ns by the TDCs resolution. The amount of energy deposited in the scintillators is distributed over a wide dynamical range (especially for neutrons). Therefore, the output signals in the PMTs can vary greatly. That can affect the time the signals pass the discrimination level. The "time walk correction" is done in the offline analysis to compensate for the pulse height-time dependence.

When a larger signal arrives at the discriminator, the output signal will cross the discriminator threshold faster than the output for smaller signals (the rise time is constant). To perform the pulse height correction, the correlation between the time and energy deposition was measured. The data for this measurement was taken from the production data because that data contained events with pulses that covered a wide ADC range.

To establish the correlation between the time and the pulse height, the time-of-flight between each PMT (Left / Right) and its reference bar was used. The reference bar for each scintillator was a bar

that was located in front of it. Time-of-flight between them is defined by Eq. 3.3:

$$TDC - 0.5 \cdot (T_L + T_R)_{\text{reference}} \tag{3.3}$$

where the first term is the time recorded in the inspected PMT and the second term is the time in the reference bar.

One MUST apply a very narrow cut on the ADC and on the hit position of the reference bar in order to eliminate time walk and attenuation affecting the reference time itself.

By looking on the TOF dependence of the energy deposition, a parametric function that corrects for the time walk can be extracted, see Figure 3.27

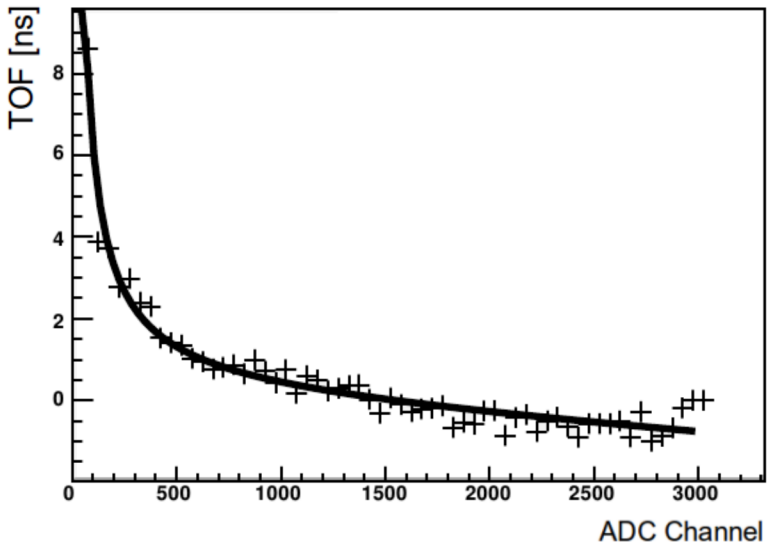


Figure 3.27: Dependence of the TOF on the energy deposition in the scintillator.

The function shown in Figure 3.27 is .

$$TDC = a \cdot X^b + c \cdot X + d \tag{3.4}$$

We fit the data to determine the a,b,c and d parameters [63].

The effect of this correction is clearly seen for the elastic measurements if we compare Figure 3.28 to Figure 3.26.

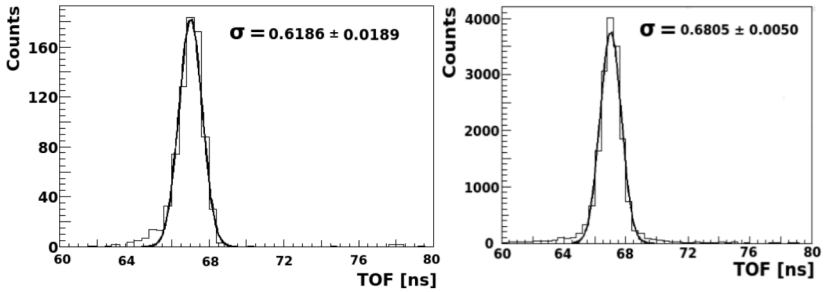


Figure 3.28: TOF distributions for elastic protons. Left side for single bar (same as for Figure 3.26) and Right side all bars combined.

The time walk correction improves the signal resolution by factor of 2, from 1.2 ns as shown in Figure 3.28 to $\sigma = 0.65$ ns, after the pulse height analysis. The improvement in the time resolution makes the TOF peak sharper and improves the signal to background ratio. This effect is demonstrated for the deuterium target in Figure 3.29.

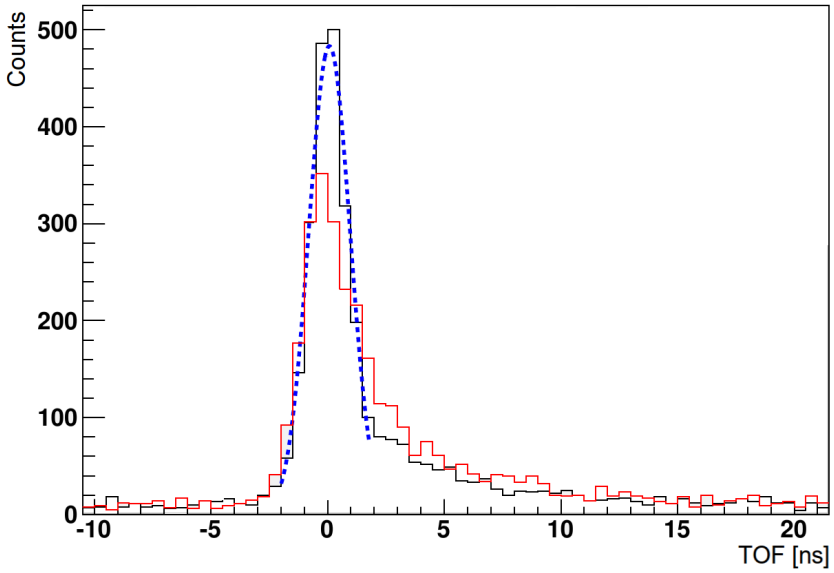


Figure 3.29: Difference between measured TOF and expected TOF for neutrons in HAND. Data is from the d$(e, e'pn)$ reaction. The impact of the pulse height correction, an increase in the signal to background ratio due to a narrower peak. Red line before time walk correction and black after.

### 3.4.4 Position Calibration.

The position along the bars can be extracted from the time difference between the left and right sides of the scintillator bar, Eq 3.5:

$$POS = a \cdot (TDC_L - TDC_R) + b \tag{3.5}$$

where a and b are constants that depend on the light propagation velocities and the bar length.

The determination of these two constants is done by fitting the measurement to the simulated position. Simulation of the position was done by taking uniformly distribution between $-50$ and 50 cm and smearing it with Gaussian ($\sigma = 10$ cm). This width was determined from the TOF resolution. The result of the measurements and simulation are shown in Figure 3.30.

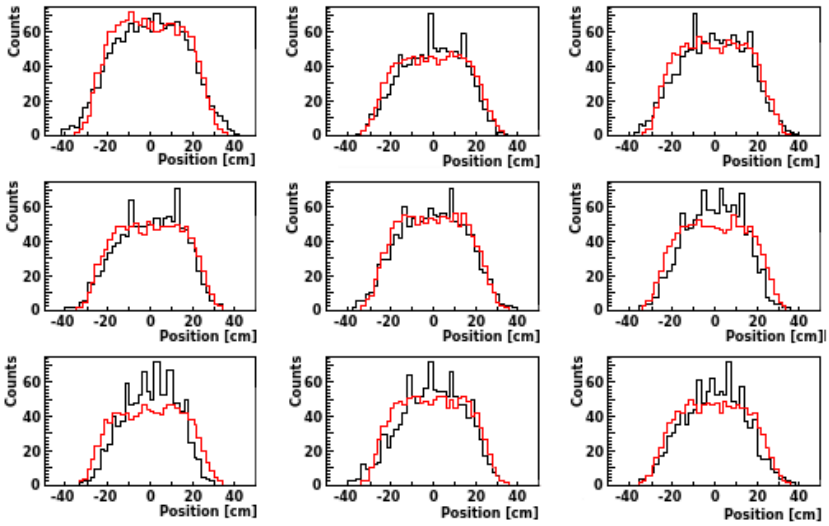


Figure 3.30: Position distributions for different bars. Red histogram represent the simulation.

### 3.4.5 Neutron ID

Neutral particles do not generate signals directly in scintillators. Rather they knock out protons or other charged particles by nuclear reactions. These charged particles deposit their energy in the scintillator's material and produce light [64].

In this experiment due to the large luminosity and the large solid angle of HAND, the recoil neutrons signals are accompanied by a large background of charged and neutral random particles that hit the detector.

The pulse height and its timing recorded by ADCs and TDCs, respectively, are not sufficient to identify the particle type. Moreover, the high energy charged particle can hit several layers and generate artificially multiple hits. To overcome these obstacles, we developed a neutron detection algorithm. The algorithm is similar to the algorithm developed for the previous SRC experiment (E01-015). In this algorithm, we use "blocking bars" in order to define a signal as a neutron [65]. A particle is defined as a neutron if it produces a hit in a bar but no signal is observed in any bars in front of it within a time window of $\pm 8$ ns (this value is based on the time resolution of HAND and on the physical time needed for a particle to pass through the bars. Other values of the time window were tested and for larger and smaller values, the number of neutrons decreased). In Figure 3.31, examples for the blocking bars algorithm are presented.

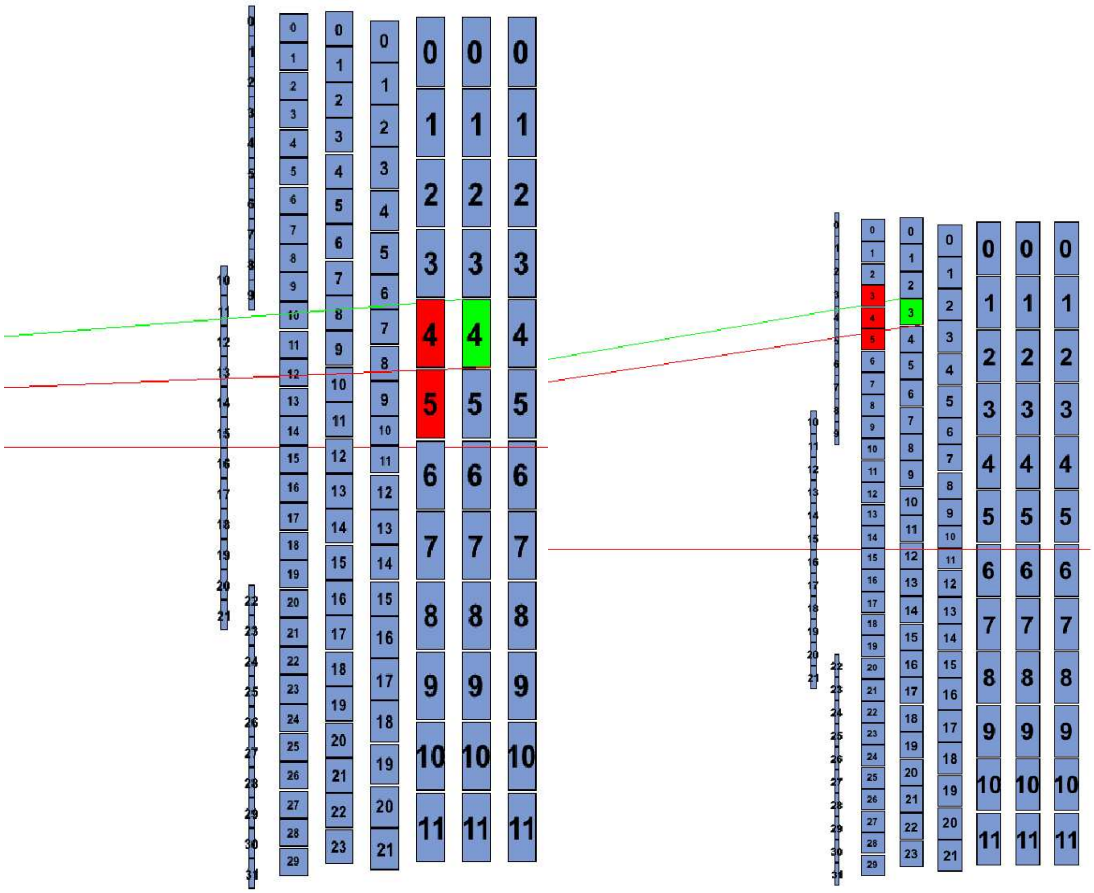

Figure 3.31: Example of blocking bars algorithm. Horizontal red line represent the center of the detector aligned with the target center. Rays pointing from the target to extreme corner of the scintillator bar are marked in green. These rays define the maximal and minimal angles in which the investigated bar can be seen from the target. Based on these angles blocking bars that are in line of sight between the target and the investigated bar are defined.

A special case of the neutral particles are photons that reach the detector. Most of the photons generate showers from the lead wall and can be identified by the Veto layer that serves as a blocking plane for the first layer. Moreover, the small number of photons that hit the scintillator bars could be easily identified based on their TOF (actually the gamma peak is very important and was used for the absolute time calibration of the detector). This blocking bars algorithm removes charged particles, but since HAND consists of many bars (and multi hit TDCs) there can be a number of "neutrons" identified in each event. In Figure 3.32 and 3.33, the number of neutrons per event is presented for 500 MeV/c and for 750 MeV/c settings respectively. These multihit events have the same number of neutrons under the TOF peak and in the background region, so we assume that the contribution from the double counting can be eliminated by the background subtraction.

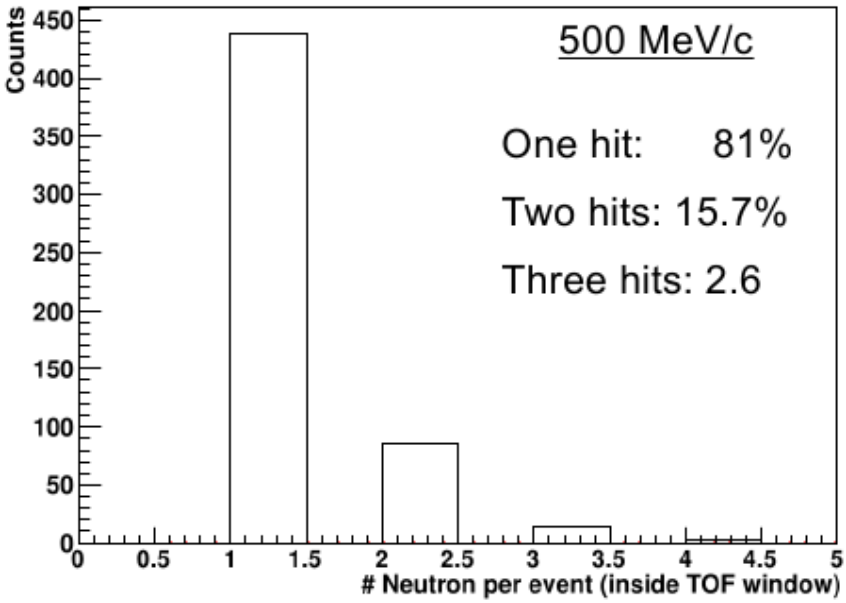


Figure 3.32: Number of multiple neutrons per event at the 500 MeV/c kinematics.

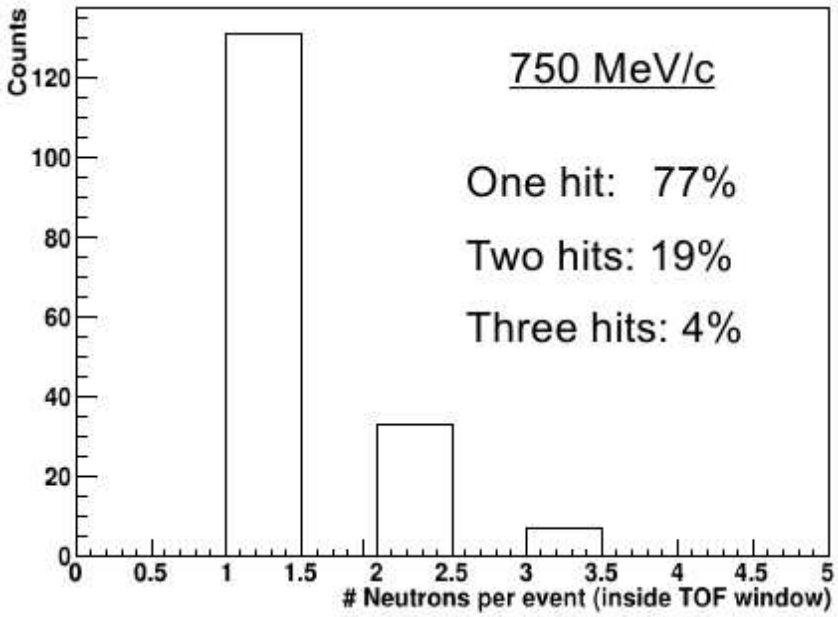


Figure 3.33: Number of multiple neutrons per event at the 750 MeV/c kinematics.

The effect of multi neutron events is also taken into account in the absolute neutron detection efficiency determination presented in the following section.

### 3.4.6 Neutron Detection Efficiency

The neutron detection efficiency is crucial in determining the number of $(e, e'pn)$ triple coincidence events. The measurement of the efficiency is done using fully exclusive scattering from the deuterium (LD2) target and detecting all three outgoing particles in the d$(e, e'pn)$ reaction. The d$(e, e'pn)$ efficiency measurements were divided into two groups. First group correspond to $p_{\text{miss}}$ of about 250

MeV/c ("low") and second for $p_{\rm miss} \sim 450$ MeV/c ("high"). In case of exclusive scattering from d$(e,e'pn)$ the size of the missing momentum is equal to the size of the neutron momentum $p_n$.
Low momentum kinematics ($p_{\rm miss} = 0.25$ GeV/c):

- Beam energy = 2.257 GeV.
- LHRS: central momentum =0.899 GeV/c, angle = 56° (protons).
- RHRS: central momentum = 1.850 GeV/c, angle = 14° (electrons).

High momentum kinematics ( $p_{\rm miss} = 0.44$ GeV/c):

- Beam energy = 1.16 GeV.
- LHRS: central momentum = 0.7642 GeV/c, angle = 54.5° (protons).
- RHRS: central momentum = 0.789 GeV/c, angle = 14° (electrons).

The rate of neutrons with momentum greater than 0.44 GeV/c is very low and practically could not be measured during the current experiment. We extrapolated the efficiency measurement to the higher neutron momenta measured during the production. The extrapolation was done using the Kent State University simulation [66] that was tested in various experiments and is considered reliable for neutrons up to 1 GeV/c.

We use following cuts to obtain the neutron TOF peak in the d$(e,e'pn)$ measurement:

1) Nominal HRSs cuts for the $(e,e'p)$, see Chapter 4.1.

2) Coincidence time between LHRS and RHRS – used to eliminate the random background.

3) Missing mass of d$(e,e'p)$ reaction – to remove the contribution of inelastic scattering and pion production that can effect the absolute neutron detection efficiency, see Figure 3.34.

4) Angular direction of missing neutron pointing toward HAND. To determine the efficiency, we need to know how many neutrons were detected out of the neutrons that enter the detector based on the d$(e,e'p)$ kinematics.

5) Vertex cut – eliminate the contributions from the aluminum walls of the target cell.

6) Vertex difference between the HRSs – to reduce the random coincidence events.

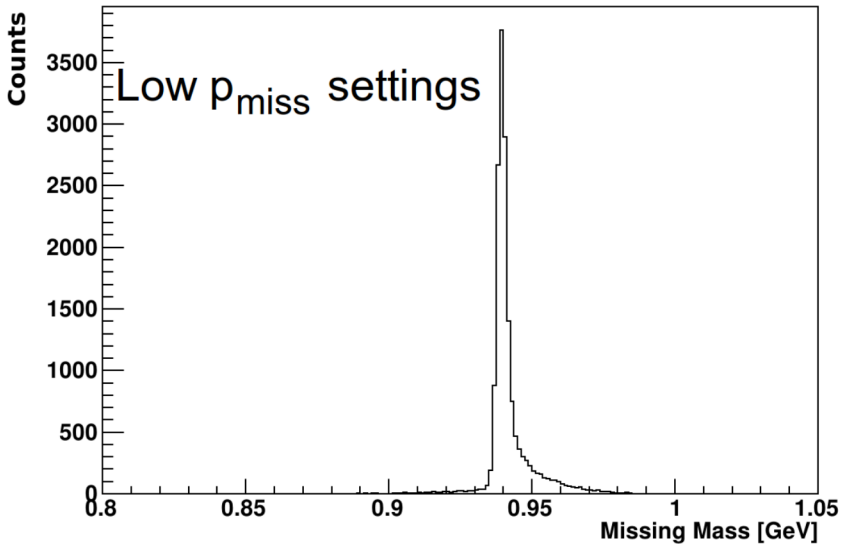


Figure 3.34: Missing mass for d$(e,e'p)$ channel during the LD2 measurements.

The number of d$(e, e'p)$ events was extracted from the $p_{\text{miss}}$ distribution and the number of d$(e, e'pn)$ from the TOF distributions of neutrons (with the cuts specified above).

The measured neutron TOF distributions for d$(e, e'pn)$ are shown below in Figure 3.35 for the "low" and the "high" missing momentum kinematics. For the low momentum settings, we have lower temporal resolution because we were not able to use the time information from HRSs (there was a problem in TDCs configuration of the FASTBUS) during the time this was measured.

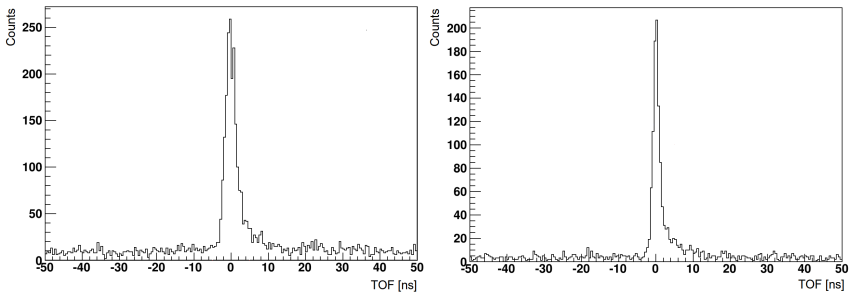


Figure 3.35: Corrected TOF spectra for low (left) and high (right) settings for the HAND efficiency measurements.

In this experiment, the best achieved resolution for neutron TOF was 1.5 ns, identical to the previous SRC experiment, and close to the best possible of 1.27 ns. This limit (1.27 ns) is due to the thickness of the scintillator bar. The thickness of the bars is 0.1 m and they were located 6 m from the target. This mean that we have uncertainty of 0.1/6. The TOF for $\sim$ 250 MeV/c is about 76 ns ($76/60 \sim 1.27$ ns).

To estimate the number of d$(e, e'pn)$ events in the "low" settings, we counted the number of events between $-5$ and 10 ns.

The efficiency was calculated as a ratio of the number of detected d$(e, e'pn)$ events out of the expected based on the number of d$(e, e'p)$ events. The angular cut was determined to be $\pm 4^\circ$ in the in-plane angle and $\pm 14^\circ$ in the out-of-plane angle. A larger angle range reduces the efficiency of HAND, see Figures 3.36 and 3.37.

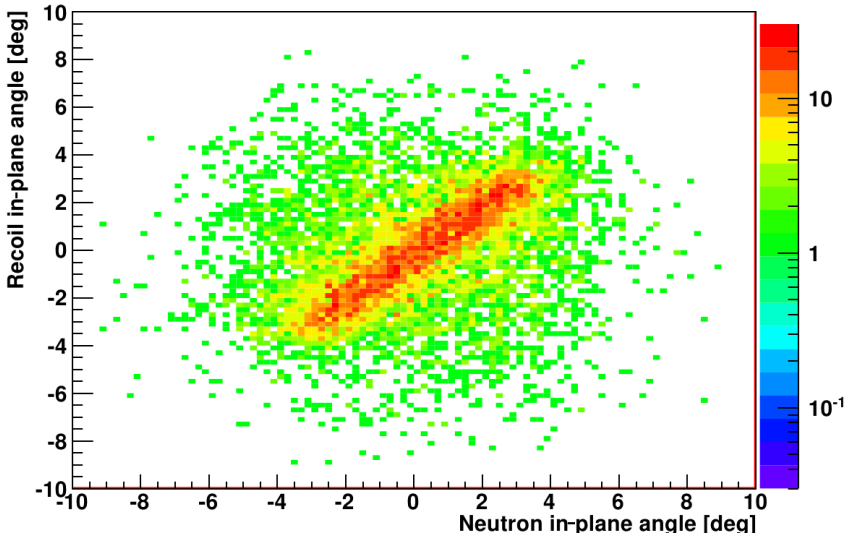


Figure 3.36: The in-plane angle based on the reconstructed neutron in HAND versus the recoil angle based on the HRSs reconstruction (d$(e, e'pn)$ exclusive scattering).

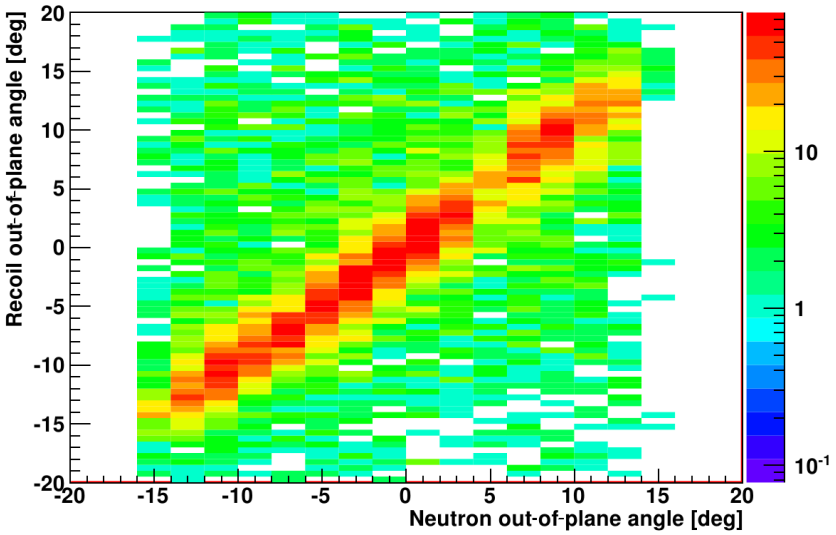


Figure 3.37: The out-of-plane angle based on the reconstructed neutron in HAND and the recoil angle based on the HRSs reconstruction (LD2 exclusive scattering).

Using all cuts stated above, the absolute neutron detection efficiency measurement is plotted on Figure 3.38:

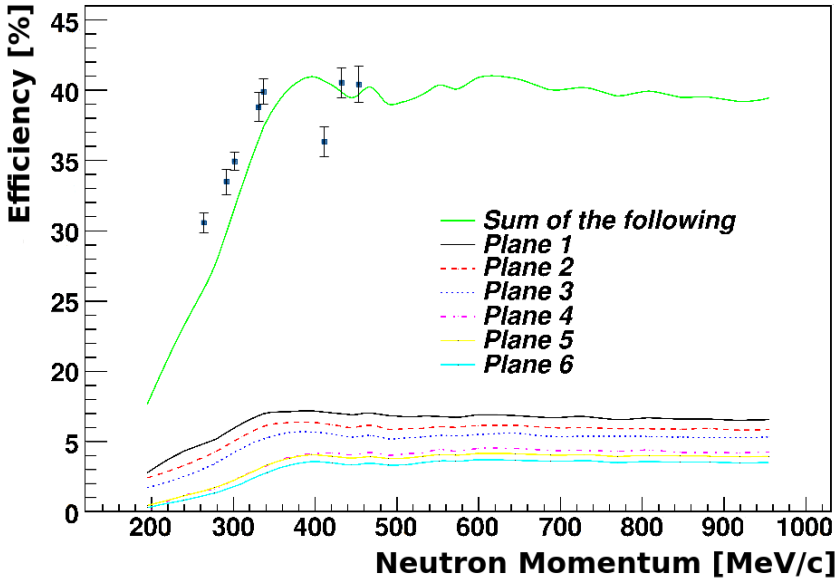


Figure 3.38: The absolute neutron detection efficiency.

A simulation with the code was using a for threshold values of 5 MeVee, which is equal to our software cut (hardware threshold was $\sim 3$ MeVee). The simulation for the neutron detection efficiency shown in the figure is scaled by $\sim 1.35$. In the previous experiment, a factor of 2 was used to match data and the simulation. For the production data, the minimal momentum is $\sim$ 350–400 MeV/c. Above this region, the efficiency is fairly constant. We analyzed the production data assuming the neutron detection efficiency is constant and equal to $40 \pm 1.4\%$.

The efficiency measurements were done prior to the production run, so in order to make sure that the neutron detection efficiency stayed at the same level we monitored the background level during the production. We expect that the neutron background level under similar running conditions, like

beam energy, current etc, to be constant. Monitoring the background level gives indications regarding the neutron detection efficiency stability. The runs that were marked as bad by shift workers (after verification) and runs that have abnormal background level were excluded from the analysis, see Figure 3.39.

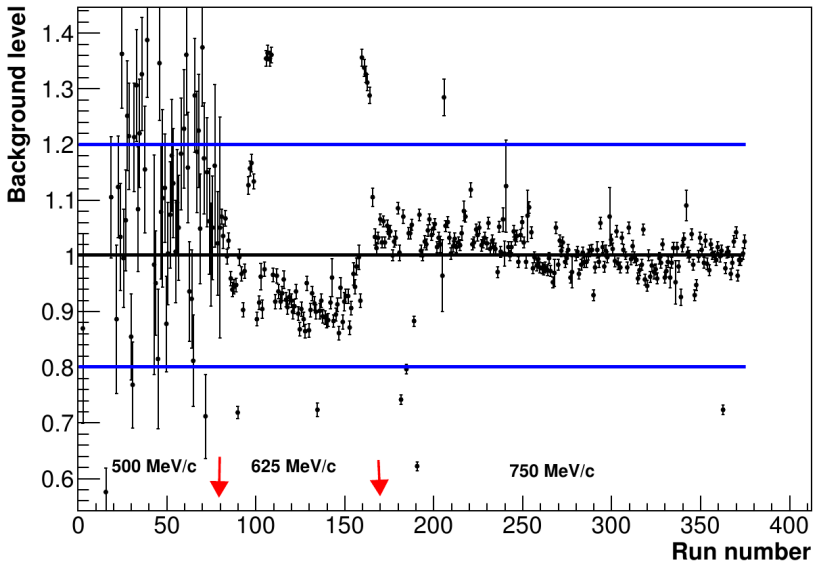


Figure 3.39: Normalized background level versus run number. Runs from 500 MeV/c are on the left and runs from 750 MeV/c setting are on the right side. The arrows represent the change between different kinematical settings. The runs within the average ±20% are taken for the analysis. These data already exclude corrupted runs, such as with no signal.

At the beginning of the production time we used different beam currents and we had large fluctuation in the background as shown in the left side of Figure 3.39.

### 3.4.7 Absolute timing and momentum calibration

TOF calibration with elastic scattering was the first step, which allowed a relative time calibration. The final absolute time calibration was done using the exclusive triple coincidence d$(e, e'pn)$ measurement with an identical electronics settings as during the production measurements. For the efficiency measurement, the RHRS was used as an electron arm and defined the time, and during the production, this was done by the LHRS. For the efficiency measurement, the statistical uncertainties are important therefore these were done with $x_B < 1$ kinematics. For absolute time determination, many fewer events are required. Switching the polarity between the spectrometers is needed in order to perform measurements at large x Bjorken ($x_B > 1$). This polarity switch introduced an unknown global offset in the timing circuit due to different cable lengths between the leading signal (electron coming from the Left or Right HRS) and HAND, that need to be determined with a known process. The kinematics that was used for the triple coincidence d$(e, e'pn)$ measurement to define the absolute time.

| Beam Energy [GeV] | Protons momentum | Proton angle | Electron momentum | Electron Scattering angle |
|---|---|---|---|---|
| 4.46 | 0.952 | −42.5 | 3.95 | 16 |

Table 3.2: Absolute time measurement kinematics.

An additional difficulty, during all the measurements with large $x_B$, is the large random background and small signal. In Figure 3.40 the measured TOF distribution in HAND for d$(e, e'pn)$ reaction is presented.

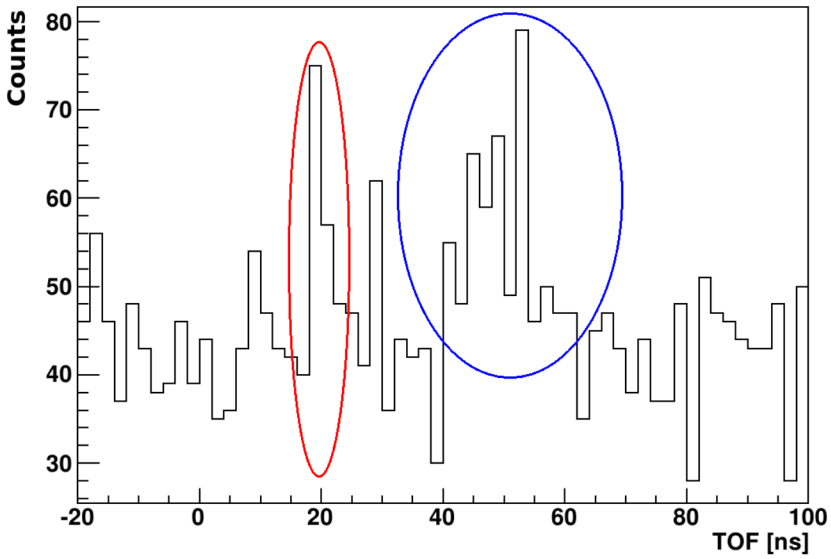


Figure 3.40: The TOF distribution measured in HAND from Deuterium target. The red circle marks the gamma peak and the blue represents recoil neutrons.

In case of exclusive scattering from deuterons, the momentum of the neutron is known to be the measured $-p_{\text{miss}}$ of the d$(e, e'p)$ reaction. TOF signal can be corrected using the reconstructed momentum of the neutron, Figure 3.41 show the corrected TOF.

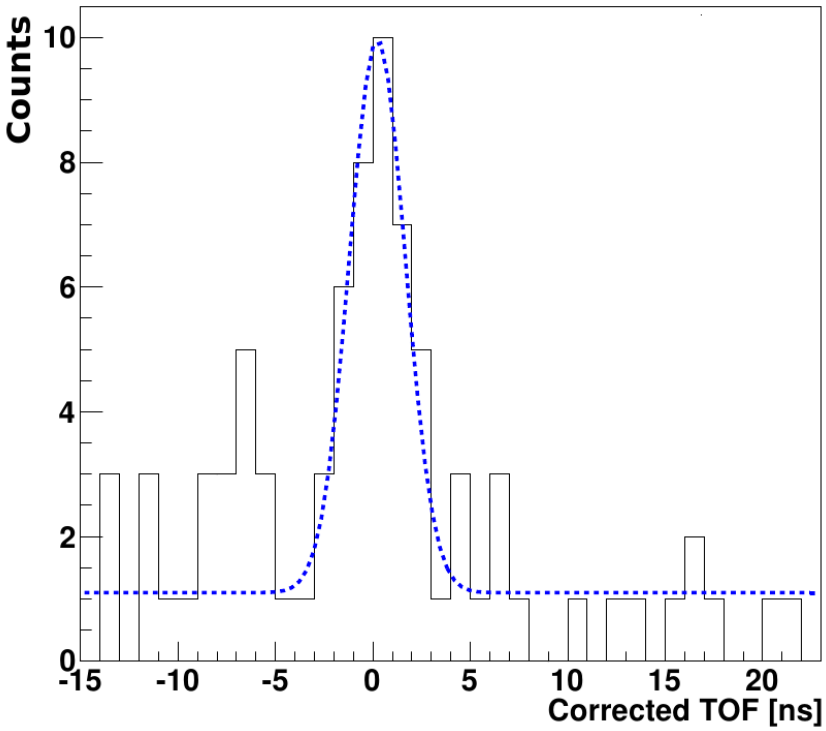


Figure 3.41: Difference between measured and expected TOF of neutrons for scattering from deuterium target after changing to $x_B > 1$ kinematics. This measurement used for absolute time determination for HAND.

The TOF resolution of $\sigma \sim 1.5$ ns was determined by fitting the distribution presented in Figure 3.41 to a Gaussian plus a constant background.

In addition to the TOF calibration based on exclusive scattering from the Deuteron target, we can check the position of the gamma peak in the spectrum. In Figure 3.40, this peak is clearly seen at TOF $\sim$ 20 ns, much sooner than the neutrons. In that figure, the gamma peak is identified in the triple coincidence reaction, but it also can be clearly identified in the double coincidence $(e, e' p_{\mathrm{recoil}})$, see Figure 3.42.

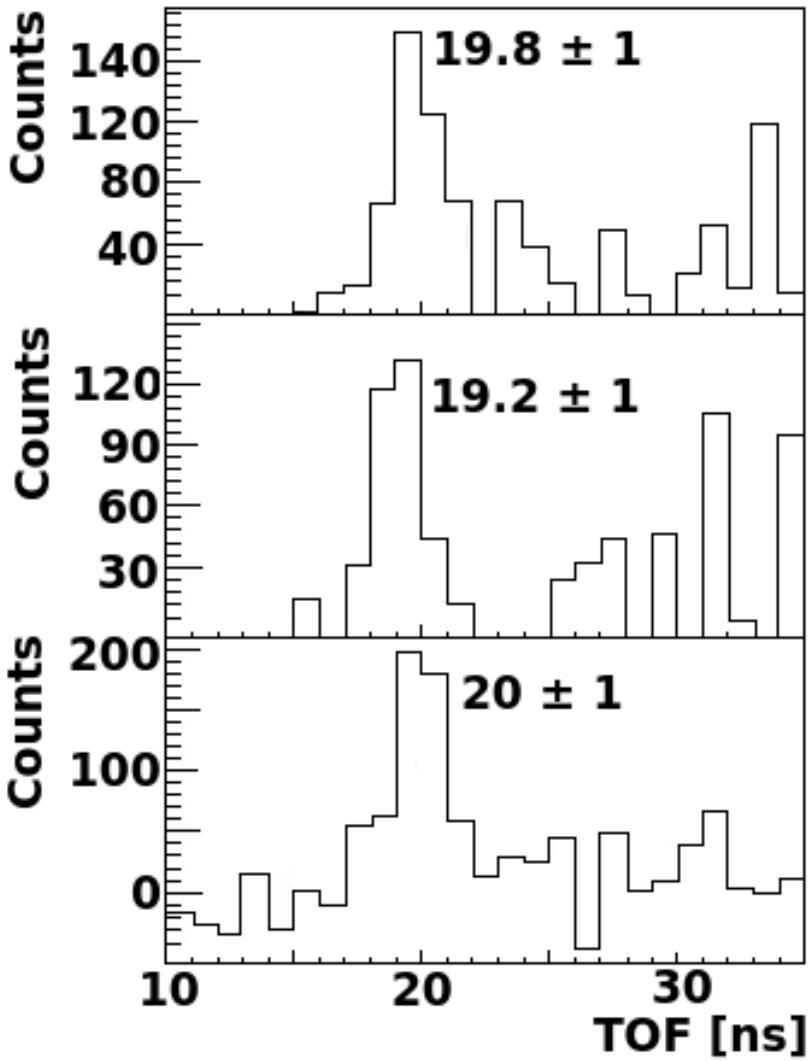


Figure 3.42: Absolute TOF spectra measured in HAND in respect to reaction time. The gamma peak identified for the three production kinematics. Top plane is for 500 MeV/c settings, middle for 625 MeV/c and bottom for 750 MeV/c. The peak positions with their uncertainties are shown near the peaks.

The exclusive d$(e, e'pn)$ measurements are time consuming due to very low rate, so there was only one such measurement prior to the production run. However, the recoil gamma can be measured during the production with the $^4$He target. This fact allow for a stability check by looking at the gamma peak position during the entire experiment as shown in Figure 3.43.

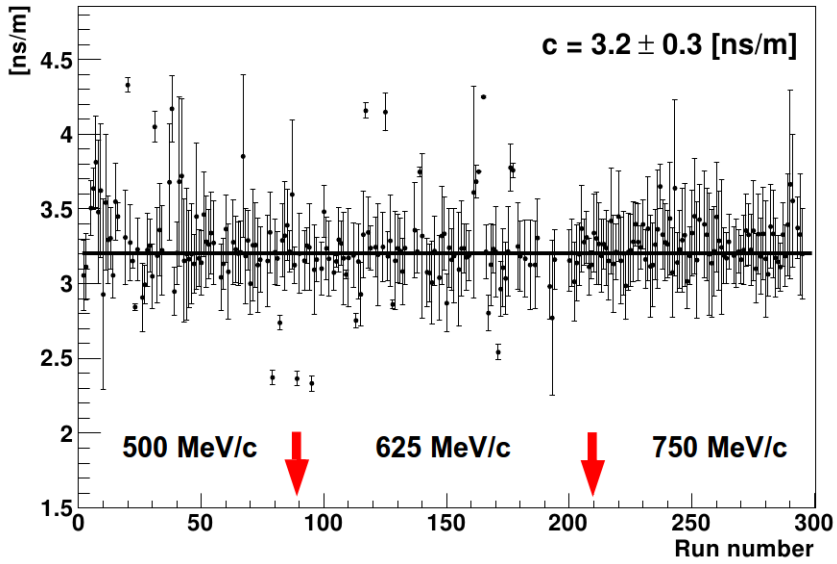


Figure 3.43: Gamma peak position in [ns/meter] vs. run number. The arrows represent the change between different kinematical settings.

Most of the data is within 3.3 ns/m ±20%. Runs with gamma peaks identified out of this range were not used for the analysis.

### 3.4.8 Neutron Momentum reconstruction

After the absolute time calibration of HAND, based on TOF information, the momentum of the detected neutrons can be reconstructed using the relation, Eq 3.6:

$$p_n = \frac{m}{\sqrt{\left(\frac{0.3 \cdot t}{d}\right)^2 - 1}} \tag{3.6}$$

where $m$ is the neutron mass, $t$ the TOF and $d$ the distance from the target to the detector.

In Figure 3.44, the neutron momentum reconstructed from TOF using the equation above is plotted versus the missing momentum for the exclusive d$(e, e'pn)$reaction.

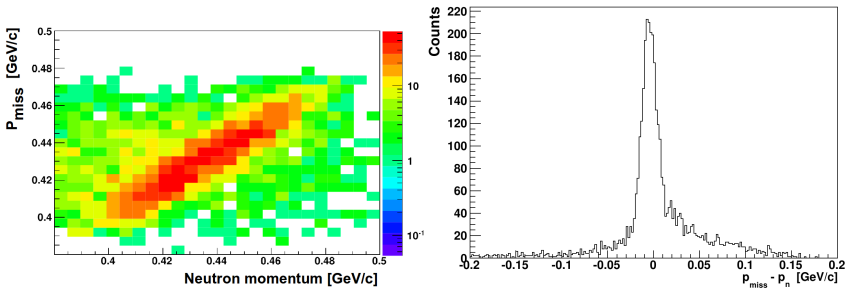


Figure 3.44: The neutron momentum reconstructed from TOF vs. the expected momentum based on the HRSs (left). The difference between $p_{\text{miss}}$ and reconstructed neutron momentum, $\Delta p$ (right). Scattering is from a liquid Deuterium target.

### 3.4.9 Event Mixing / background

During production running, there was a large random background in the neutron TOF spectra that must be taken into account. To count the number of recoil neutrons, we need to subtract from the total number of events in the peak the number of background events. The number of background events can be estimated by taking the background level measured out of the peak region. However, some of the physical quantities we are interested in like momentum and the missing mass depend on the TOF and can not be calculated in the out of peak region. For example, momentum in the time shorter than 20 ns is not defined since it corresponds to a time shorter than that needed for light to travel 6 meters from the target to HAND. To subtract the random background in these cases, we need to use a different approach. This is done using event mixing technique which allow is to estimate the background level independent on the variable of interest. In the event mixing procedure we use actual data and mix different particle from different events, so we know that the output of the mixing is a random background. The information for the knocked-out proton ($(e, e'p)$ reaction) is taken from one event and the information for the recoil neutron from all other events, except the one that is used to define the knocked-out proton. In the text below we describe the algorithm for the mixing with an example based on the 750 MeV/c kinematics. In addition we verify that the mixing algorithm is consistent with the simulated random background.

The simulation was done in the following way:

1) We take protons from ($(e, e'p)$ events) (For the example shown below the 750 MeV/c data set measurement).

2) We simulate neutrons ($(e, e'pn)$ events) by generating neutrons back to the $p_{\mathrm{miss}}$ of the $(e, e'p)$ reaction with a smearing momentum assuming a Gaussian with a width of 100 MeV/c in each axis (based on the experimental result, discussed in section 4.4).

3) We generated a random background in HAND by making uniform distribution of particles in TOF and uniform distribution in the spatial acceptance of the detector ($\pm 4^\circ$ in and $\pm 14^\circ$ out of the scattering plane).

4) We combine the "signal" and the "background" events with a known ratio.

5) We generate background by mixing events using the algorithm described above (taking protons from one event and recoil neutrons from all others).

The example for event mixing algorithm and comparing it to the simulated background is presented below.

In Figure 3.45 shown simulation for neutrons TOF distribution obtained by $(e, e'p)$ events from 750 MeV/c kinematics and applying step #2 above. In addition we simulate a flat background (step #3) and than combine both (step #4).

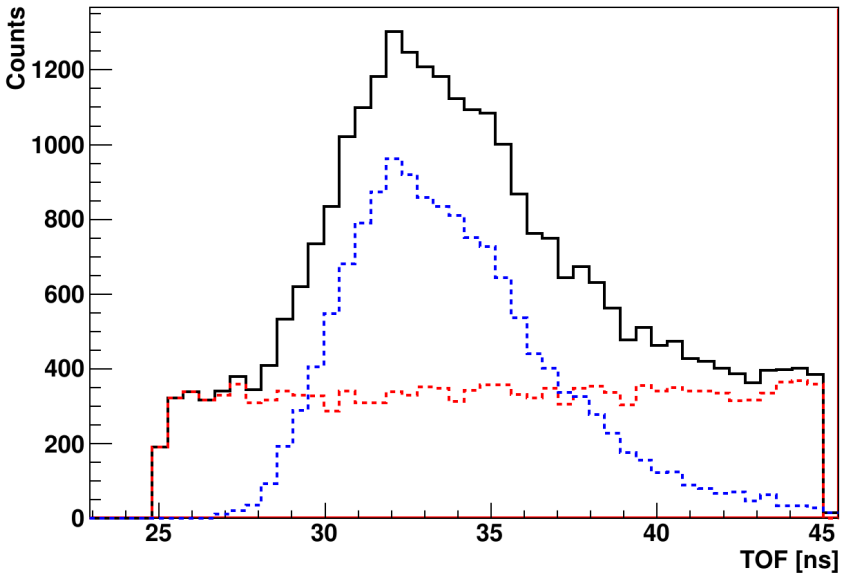


Figure 3.45: Simulated TOF distribution in HAND. Background (red dashed line), SRC recoil neutrons generated using $(e, e'p)$ data for 750 MeV/c (blue dashed line) and the combine distribution (black line).

In the last step (#5) the event mixing is performed in the TOF range of interest. In this example we took a range from 25 to 45 ns. If the event mixing is done directly on the black distribution of Figure 3.45 than the shape of the mixed events remains same. In order to prevent this, we assign weight to each TOF bin in order to generate a flat background,

In the event mixing from the simulation we know exactly for each event, if it is a signal or background event. We compared the mixing output to the expected background distribution. The physical quantities such as the opening angle and CM momentum for pure signal and for pure background are used.

The results of the simulation and event mixing algorithm are shown in Figure 3.46.

The black line represents the pure simulated signal of neutrons (no background). The red line in the figure represents the pure background distribution from the simulation, while the blue line is after the event mixing procedure as described above. Thus, we expect that the background events generated by the uniform distribution will be identical to events distribution resulting from the mixing and this can be verified in Figure 3.46.

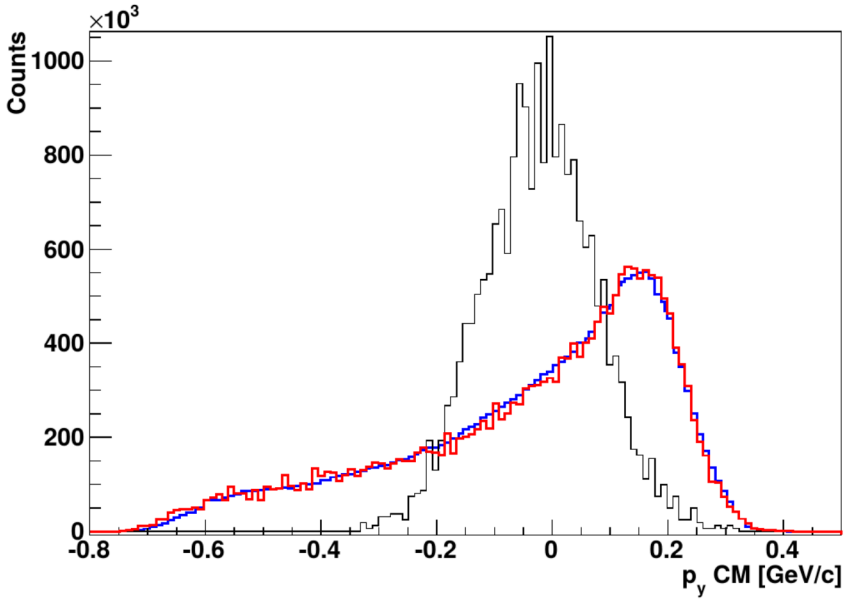


Figure 3.46: Distribution of the simulated CM of the pair in the $y$ direction in Lab coordinate system ($y$ direction is almost aligned with the direction of the detected particle in HAND). Black histogram – pure neutrons signal simulated based on the $(e, e'p)$ events from 750 MeV/c kinematics, Red – pure BG distribution, Blue – mixed events. See text for more details.

One important precaution should be taken during the events mixing algorithm. If the mixing is applied directly on the TOF distribution of Figure 3.45 (black line) than the resulting mixing will give wrong results. The shape of the TOF and physical quantities would be similar to the original shape. This happens because there is more events under the peak than the mixing will be biased to this events. In order to remove this bias, we normalized the number of events for each bin in TOF to the height of the random background, for the simulation it was taken as red dashed line of Figure 3.45.

# Chapter 4

# Results

## 4.1 $^4$He$(e, e'p)$ Event selection

Following the calibrations of the detectors, the next step in the analysis was the selection of the events. The basic data set is the double coincidence $^4$He$(e, e'p)$ events from T5 triggers. The first set of cuts that were applied on the data defined the acceptance of the spectrometers. The nominal cuts are:

- in-plane angle ±30 mrad, see Figure 4.1.
- out-of-plane angle ±60 mrad, see Figure 4.1.
- momentum acceptance ±4.5%, see Figure 4.2.

These cuts were applied to the electrons in the L-HRS and the protons in the R-HRS.

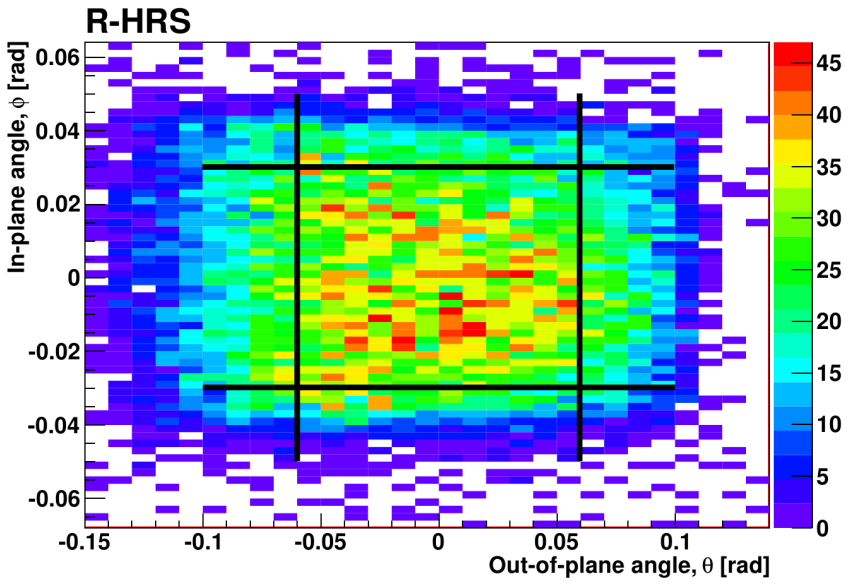


Figure 4.1: In plane angle vs out of plane angle for R-HRS. Acceptance are marked with the black lines.

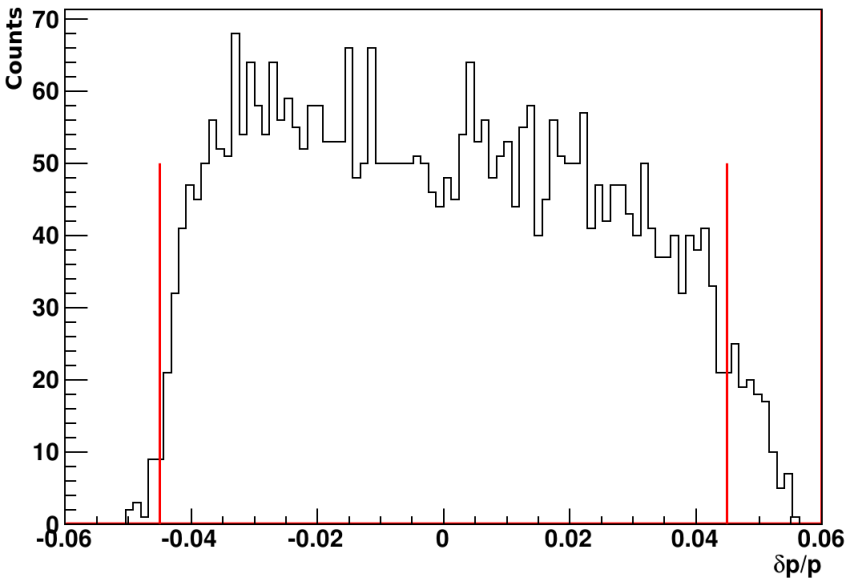


Figure 4.2: Momentum acceptance of the R-HRS. Vertical lines represent the applied cuts (identical to the nominal acceptance cut). Similar cuts were applied to the L-HRS.

As already mentioned, the trigger was generated from a coincidence between signals from the left and right HRSs. However, the electronic coincidence time can be improved by calculating the actual time difference between the RHRS and the LHRS. The LHRS detected electrons, and therefore the time of its signal (with respect to the time of the reaction in the target) depends only on the path length of the particles ($\beta \approx 1$). For the RHRS, the time also depends on the momentum of the hadrons (in our kinematics $0.75 < \beta < 0.83$). In Figure 4.3 the measured coincidence time is presented. The coincidence time resolution after the path length and momentum correction was $\sim 0.6$ ns and we applied a cut of $\pm 3\sigma$. Figure 4.3 shows an example from a run with a LD2 target.

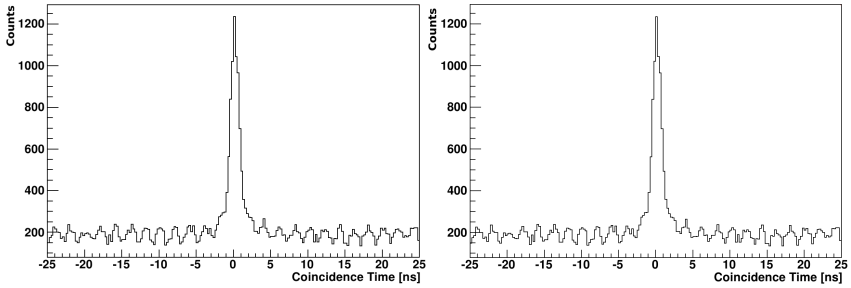


Figure 4.3: Coincidence time after the correction between HRSs. Left figure results from scattering from a Deuterium target and right figure is coincidence time for the 750 MeV/c $^4$He production data (no additional cut applied). The 2 ns beam structure is clearly seen in both figures.

The next cut that was used is the cut on the reconstructed vertex. The $^4$He was contained in an aluminum cylinder. In order to remove the contribution of the Al$(e, e'p)$ events, we applied a cut to remove scattering events from the cell end caps; see Figure 4.4.

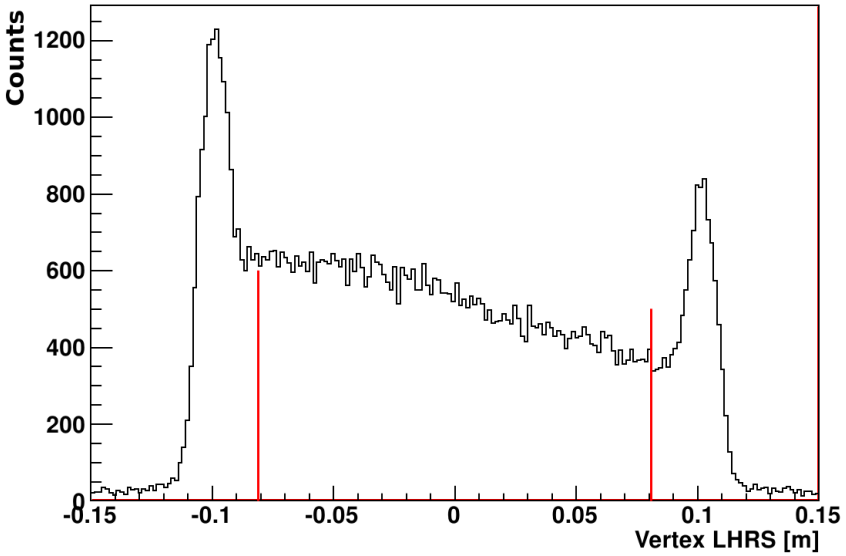


Figure 4.4: Vertex reconstruction based on the L-HRS. Target walls are identified and a software cut removed their contribution.

The target length was 20 cm, the cut applied was ±8.1 cm. The vertex resolution of the HRSs was $\sim 1$ cm. The choice of the above cut removed the contribution from the wall and treated as systematic error of less than $< 3\%$ under all measured conditions.

The random background from scattered electrons from one event and protons from another was reduced by cutting on vertex difference between L-HRS and R-HRS, as shown in Figure 4.5.

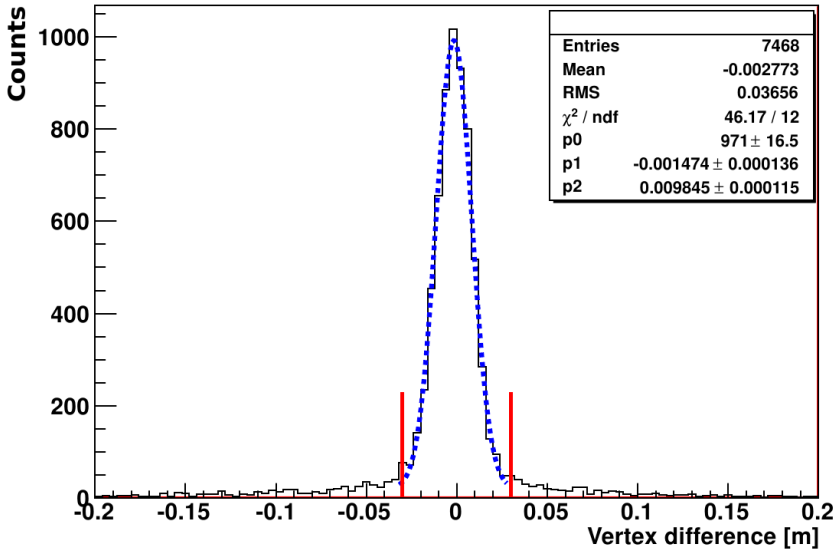


Figure 4.5: The difference between the vertex reconstructed by the L-HRS and the R-HRS. The cut shown was used to remove random background.

The applied cut on the vertex difference was ±3.2cm.

## 4.2 The semi-inclusive $(e, e'p)$ reaction.

The cuts on coincidence time and on the vertex information are sufficient for selection of protons in the R-HRS. No additional PID cut is required. In Figure 4.6 the beta distribution (measured using the time difference between the s1 and the s2m planes) of the events in R-HRS for the highest missing momentum setup is presented. In this kinematic we have the largest contamination from pions. However, it is clear that the cut on the coincidence time and the vertex position are sufficient to reduce the non proton contribution.

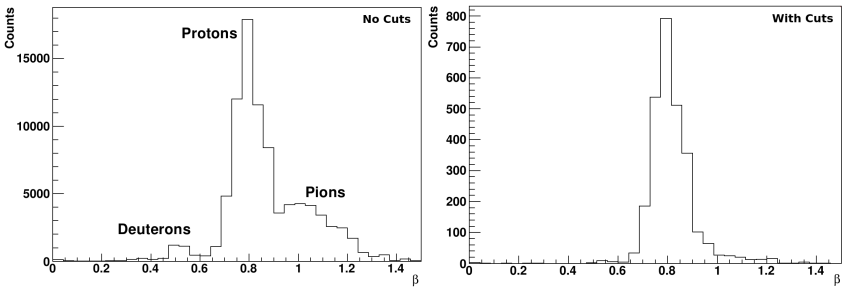


Figure 4.6: Beta distribution for 750 MeV/c. Left figure show the spectrum before the cuts on coincidence time and vertex were applied. Right figure show the events after the cuts were applied.

In order to investigate the SRC region, in addition to the basic event selection cuts, additional physical cuts are needed to suppress the contributions from competing processes. These cuts are intended to remove the contributions from events with a pion (or $\Delta$) produced. That reaction becomes accessible for missing energy larger than 140 MeV. In this analysis, we followed the procedure described in details in Ref. [33] and used a cut on the $\omega - y$ scaling plane to remove the contributions from the pion and $\Delta$. Similar to the $x_B$ variable that represents the momentum fraction carried by struck quark in a deep inelastic scattering (DIS) process, the y-Scaling variable is the equivalent when considering nucleons in nuclei (i.e. hadrons instead of quarks). Here we used the derivation of y-Scaling variable for the A$(e, e'p)A-1$ reaction as defined in Ref. [33]:

$$y\left(\vec{q},\,\omega\right) = \left[\left(M_A + \omega\right)\sqrt{\Lambda^2 - M_{A-1}^2 W^2} - \vec{q}\Lambda\right]/W^2 \tag{4.1}$$

where $W = \sqrt{\left(M_A + \omega\right)^2 - q^2}$ is the center-of-mass energy, $\Lambda = \left(M_{A-1}^2 - M^2 + W^2\right)/2$ , $M_A$ and $M_{A-1}$ are masses of the initial and recoil systems respectively, $\omega$ and $\vec{q}$ are energy and momentum transfer of the virtual photon.

The missing energy of the reaction should be large enough to accommodate the kinetic energy of the recoil nucleon (for the 750 MeV/c momentum of the recoil nucleons, the kinetic energy is $\sim 250$ MeV). In the kinematic of this experiment, there was not a pronounced separation between the nucleon and $\Delta$ regions. Choosing large $x_B$ suppresses pion/$\Delta$ production. Nevertheless we used a cut on the $\omega - y$ plane instead of a cut on $x_B$. In general the positive values of $y$ scaling parameter corresponds to $x_B < 1$ and negative to $x_B > 1$. The choice of this cut instead cutting on $x_B$ was done following previous analysis [33]. In this previous analysis a number of similar cuts were tested and the separation from the delta region was optimized. We also estimated our ratios based on other similar cuts, but all results were the same within the uncertainty limits (see section 4.10).

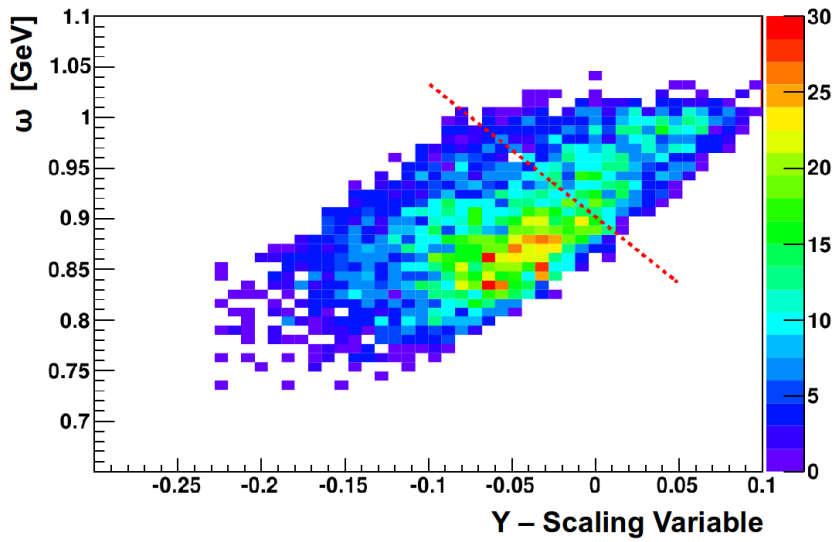


Figure 4.7: A plot of energy transfer versus the $y$ scaling variable. Example from 500 MeV/c, a cut that separates the nucleon and the possible $\Delta$ regions. Positive values of $y$ scaling corresponds to $x_B < 1$, where the $\Delta$ production is not suppressed.

The two-dimensional cut on $\omega - y$ plane removes the large missing energy events in the $^4$He(e,e'p) reaction that are most probably related to the $\Delta$-production region; see Figures 4.8, 4.9 and 4.10.

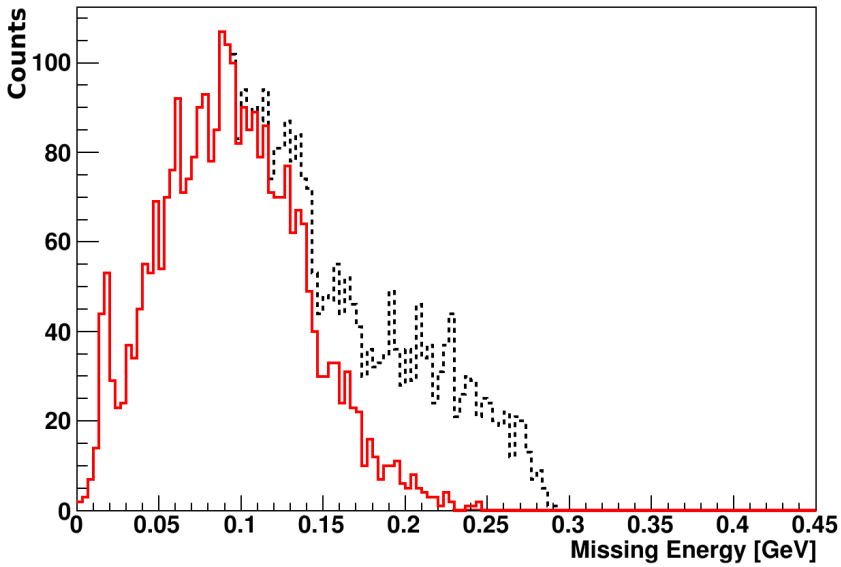


Figure 4.8: $(e, e'p)$ Missing energy distribution for 500 MeV/c. Red distribution represents the events with $\omega - y$ cut. Dashed line represents all events.

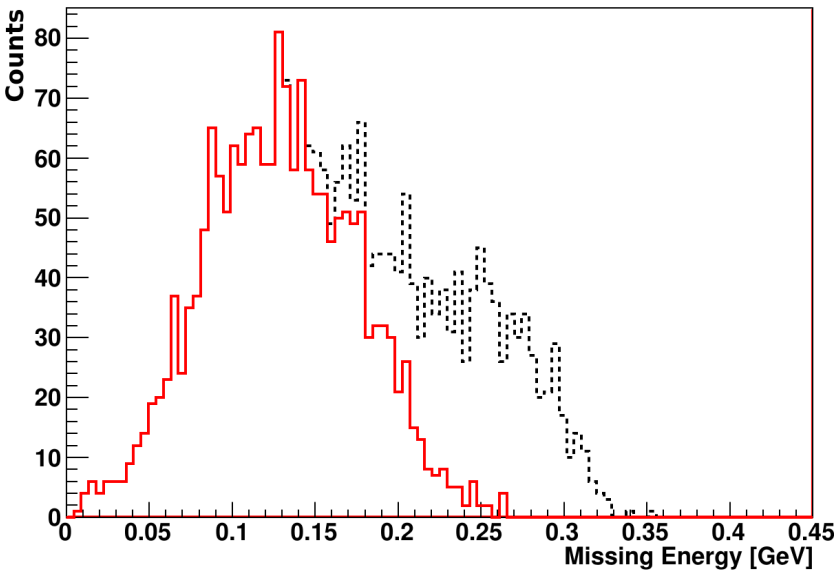


Figure 4.9: Same as Figure 4.8 for 625 MeV/c.

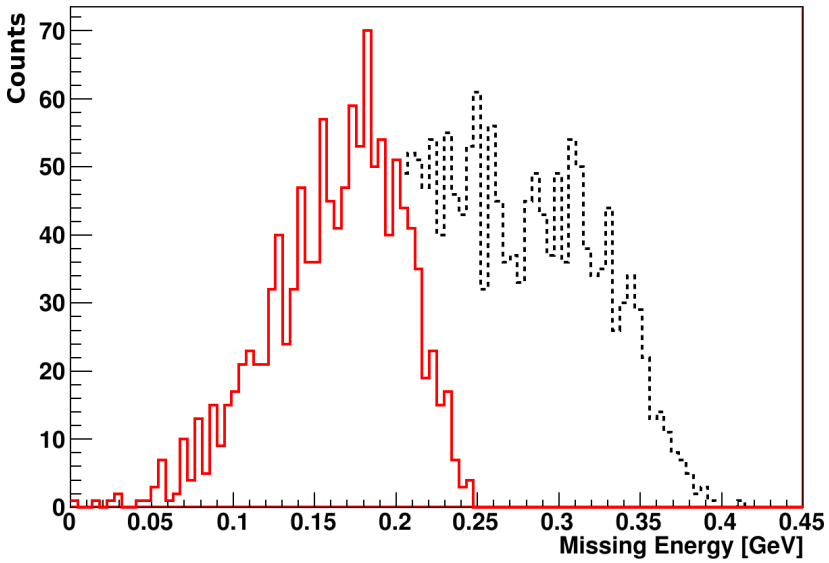


Figure 4.10: Same as Figure 4.8 for 750 MeV/c.

In Figures 4.11 and 4.12, the effect of the $\omega - y$ cut (show in Figure 4.7) on the distributions for the kinematical variables, $x_B$ and $Q^2$ is shown.

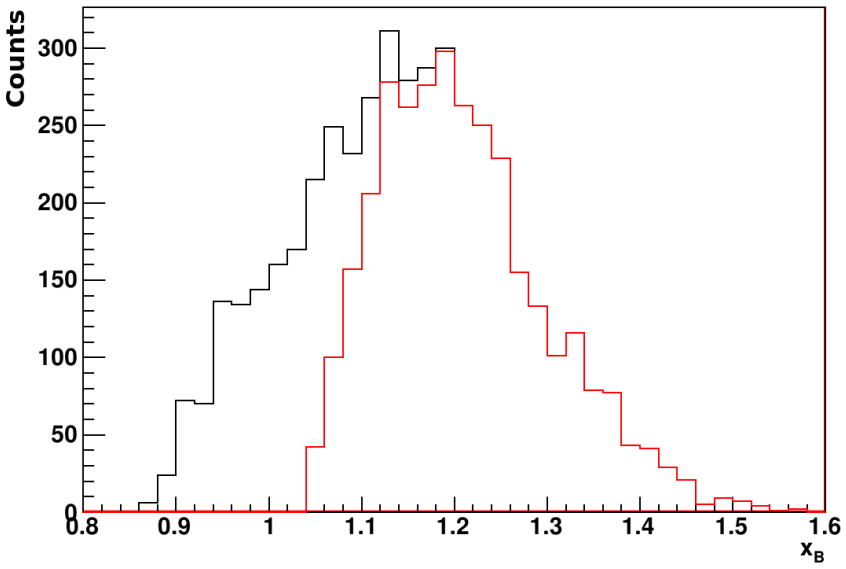


Figure 4.11: Number of events versus $x_B$. The histograms shows the distributions with/without (Red/Black) cut on $\omega - y$. The $\omega - y$ cut is as shown in Figure 4.7.

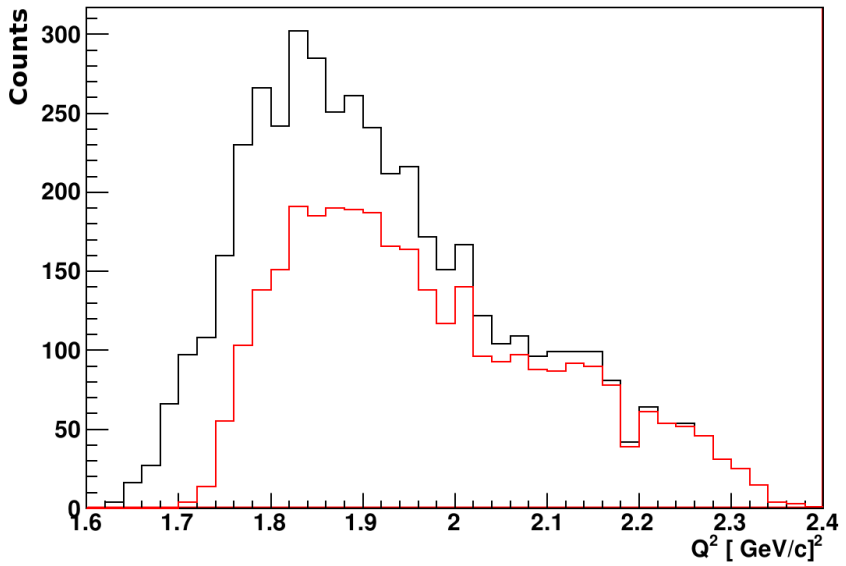


Figure 4.12: $Q^2$distribution. Red/Black with/without cut on $\omega - y$ as shown in Figure 4.7.

Even with the $\omega - y$ scaling cut, there is contamination from pion production as shown in Figure 4.13. This is important for extracting the $^4$He$(e, e'pp)/^4$He$(e, e'p)$ and $^4$He$(e, e'pn)/^4$He$(e, e'p)$ triple to double ratios (see section 4.8), because we wish to avoid changes in the ratio due to contamination of the denominator by pion production. To do so, we add a cut on the missing mass to be below 1 GeV.

The missing momentum coverage of the three kinematics for this experiment is shown in Figure 4.14.

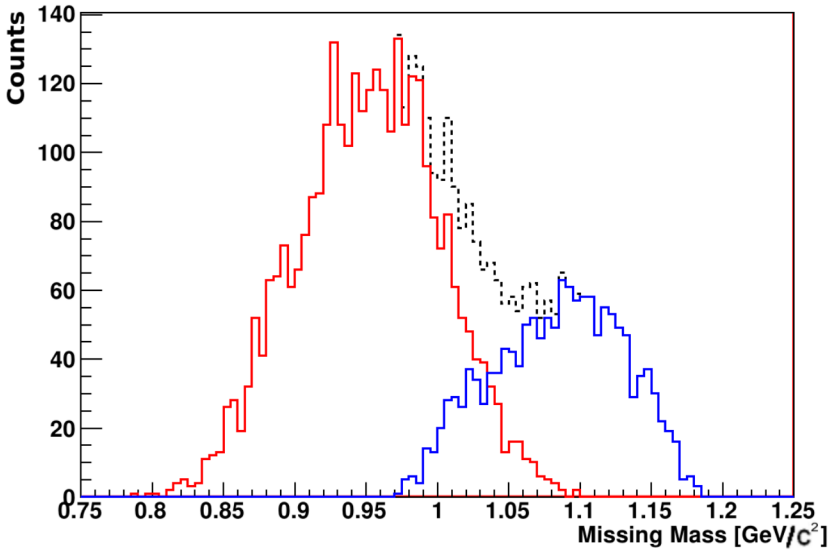


Figure 4.13: $(e, e'p)$ Missing mass distribution. Dashed line represent all $(e, e'p)$ events. Red are events coming from the $(e, e'p)$ region in the $\omega - y$ scaling plane. Blue is from the excluded region in the $\omega - y$ plane.

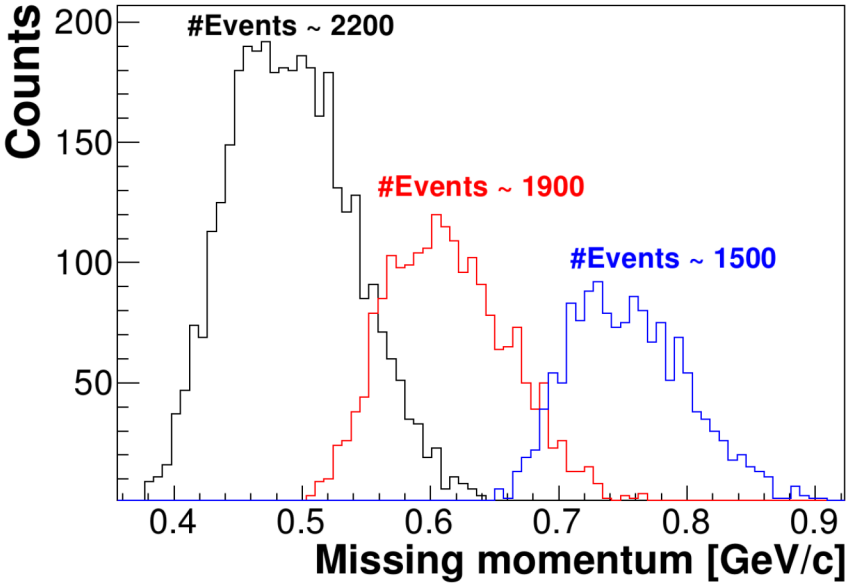


Figure 4.14: Missing momentum distribution for three kinematical setups of the experiment. Total number of $(e, e'p)$ event for each kinematics are presented with the cuts listed below.

To summarize, the cuts that were applied in order to select $^4$He$(e, e'p)$ events are:

- HRSs acceptance cuts.
- L-HRS/R-HRS Coincidence time cut.
- A cut on the vertex.
- Vertex difference between LHRS and RHRS.
- $\omega - y$ scaling cut.

- Missing mass cut (will be discussed in section 4.6).

## 4.3 $^4$He$(e, e'pn)$ Triple coincidence events.

For the $(e, e'p)$ events that passed the selection cuts we produced TOF distribution for neutrons in HAND (and protons in BigBite) simultaneously to identify a recoil neutron (proton). The TOF distributions and the momentum reconstruction for the three measured kinematics are presented in Figures 4.15, 4.16 and 4.17.

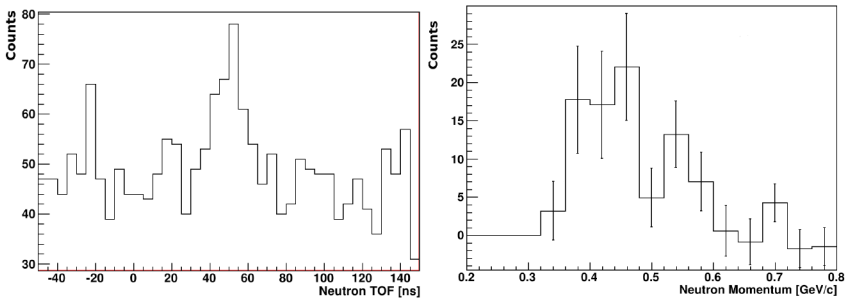


Figure 4.15: TOF distribution and reconstructed background subtracted momentum distribution for neutrons at 500 MeV/c.

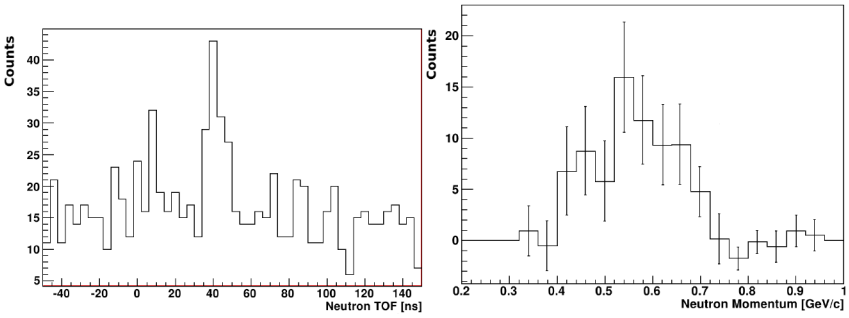


Figure 4.16: Same as Figure 4.15 for 625 MeV/c.

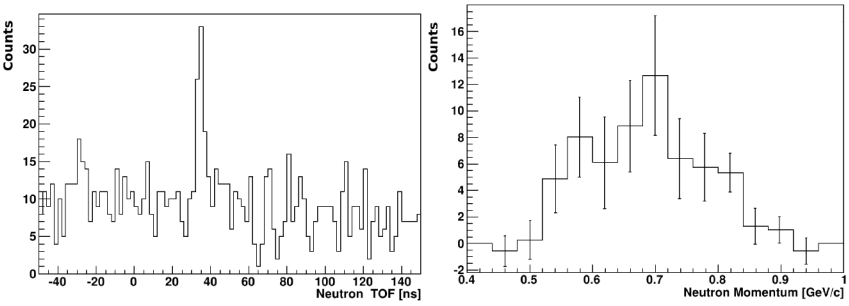


Figure 4.17: Same as Figure 4.15 for 750 MeV/c.

As can be seen in Figures 4.15, 4.16 and 4.17, with increasing missing momenta the main TOF peak is shifting to shorter time, and the neutrons have a larger reconstructed momentum. The width of the peaks also reduces as the missing momentum increases.

The TOF distributions have a large background to signal ratio that does not allow us to investigate the physical quantities on an event by event basis. However after background subtraction (see below) the total number of recoil neutrons can be determined.

In order to count the number of triple coincidence events, we applied an angular cut $\pm 4^\circ$ (in-plane) and $\pm 14^\circ$ (out-of-plane) and a cut on TOF. The former was required for determining the solid angle for the protons (BigBite) and neutrons (HAND) detection. The latter was set to be between 30 and 60 ns, corresponding to neutron momenta between 300 and 900 MeV/c. To determine the total number of real triple coincidence $^4$He$(e, e'pn)$ events, subtraction of the random background was performed. We assumed a flat background; the background has a slight negative slope, which is negligible in the relevant region of the cut. The net real triple coincidence events were defined as:

$$Net = (S + B) - (B/n) \tag{4.2}$$

$$\Delta Net = \sqrt{(S + B) + (B/n)^2} \tag{4.3}$$

where $Net$ is the background subtracted net number of $(e, e'pn)$ events, $(S + B)$ is the total number of events in the peak window, $B$ is the number of events outside the peak while $n$ is the ratio between the width of the background and the peak windows. In order to reduce the contribution to the statistical uncertainties from the background $(B)$, the background level was measured in a wider range than the signal range and than normalized. The range for background was take from both sides of the peak, between $-90 - 10$ ns and $150 - 250$ ns. The number of $^4$He$(e, e'pn)$ events are given in Table 4.1 with their statistical uncertainties.

| Kinematic setup | $\#(e, e'pn)$ measured | $\#(e, e'pn)$ efficiency corrected |
|---|---|---|
| 500 MeV/c | $107 \pm 20$ | $267.5 \pm 51$ |
| 625 MeV/c | $66 \pm 14$ | $165 \pm 35$ |
| 750 MeV/c | $50 \pm 13$ | $125 \pm 33$ |

Table 4.1: Number of triple coincidence $^4$He$(e, e'pn)$ events.

## 4.4 CM motion of the pairs

One of the important physical quantities describing the SRC pair is its center of mass momentum (CM). This quantity is not affected by the FSI between nucleons in the SRC pair and can only be modified by the FSI with the residual $A - 2$ nucleons.

The CM momentum is defined as:

$$\vec{p}_{\rm cm} = \vec{p}_{\rm miss} + \vec{p}_{\rm rec} \tag{4.4}$$

Based on the previous investigations of the exclusive scattering, we measured the CM momentum in a coordinate system that has one axis $(z)$ along the $\vec{p}_{\rm miss}$ direction. Our kinematics select nucleon pairs with large relative momenta. The probability to find such high relative momentum in the nucleus decrease as the momentum increase. There is alternative way to find high momentum nucleon in the nucleus i.e. combining lower relative momentum (higher probability) with CM motion in the same direction, see Figure 4.18. This can create a biased shift in the CM momentum in the $\vec{p}_{\rm miss}$ direction while the orthogonal directions to $\vec{p}_{\rm miss}$ are centered around zero.

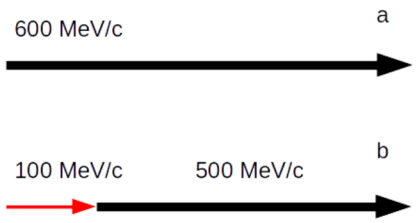


Figure 4.18: Two examples how a high momentum nucleon can be produced. (a) High relative momentum (b) Lower relative momentum (black arrow) plus contribution from CM momentum (red arrow).

The reconstructed CM momentum distributions are shown in Figure 4.19:

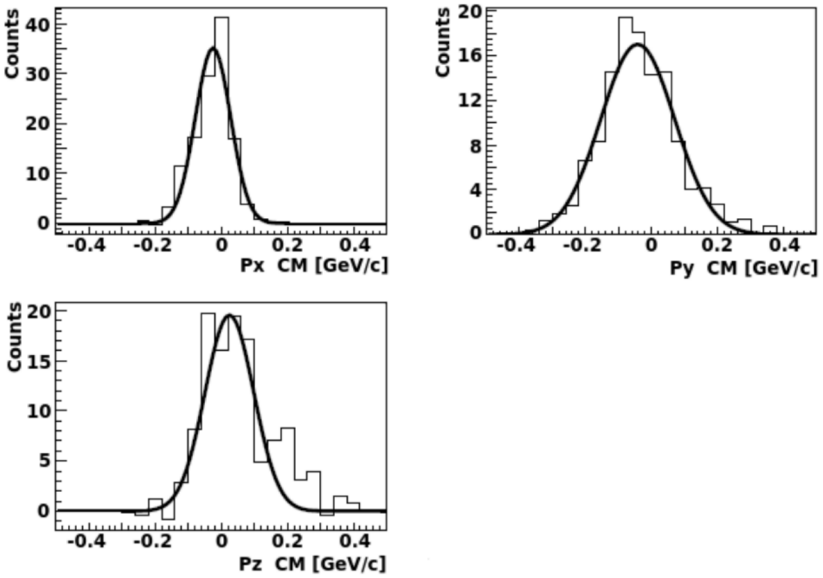


Figure 4.19: The number of events as a function of the $x$, $y$ and $z$ components of $\vec{p}_{\rm cm}$ distributions. $x$ and $y$ directions (top left and right respectively) are orthogonal directions to $\vec{p}_{\rm miss}$ and $z$ (bottom) along $\vec{p}_{\rm miss}$. The distributions shown here are for the 750 MeV/c kinematics.

The measured CM momentum distribution is not the actual momentum distribution of the pair, since the measured distribution is truncated by the finite acceptance of HAND. In order to find the actual CM momentum, we performed a simulation by taking $(e, e'p)$ events and simulated the recoil neutron with different values of CM momentum. By applying the acceptance cuts on the simulated events, we truncated the CM momentum extracted from the simulation and compared it to the measured CM. The intersection between the output of the simulation and the measured values was found. In the CM simulation, we assumed a Gaussian distribution with the same width for each axis (along the $\vec{p}_{\rm miss}$ and in the orthogonal directions). In addition, we repeated the above simulation, however this time we added an additional shift to a simulated neutron along the $\vec{p}_{\rm miss}$ direction. The results of the simulation are presented in Figures 4.20,4.21 and 4.22.

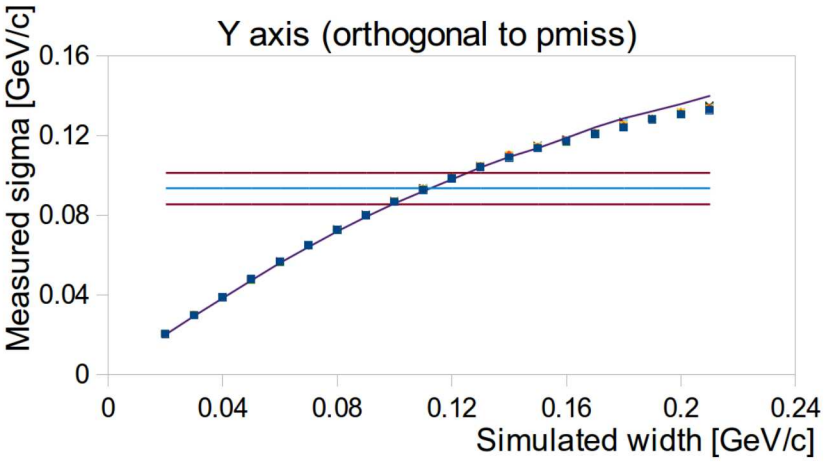


Figure 4.20: The measured width as a function of simulated width in the $y$ direction. The horizontal lines show the measured width of the $\vec{p}_{cm}$ distribution with its uncertainty band, $\pm\sigma$, (see text below for details). The solid curve corresponds to the simulation without applying the cut on the TOF. The different colors and shapes of the points are explained in the text below.

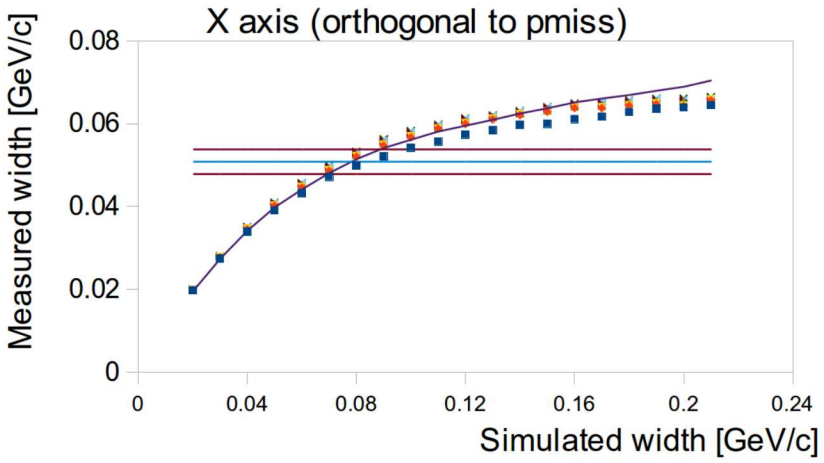


Figure 4.21: Same as Figure 4.20 but for the $x$ direction.

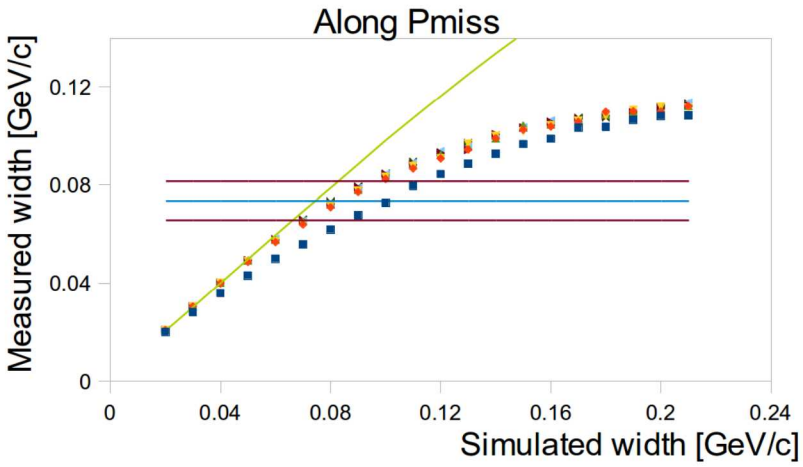


Figure 4.22: Same as Figure 4.20 for the $z$ direction (along $\vec{p}_{\rm miss}$).

The above three plots are taken from the 750 MeV/c settings. The different points colors/shapes in the above figures represent different constant shift in the $p_{\rm miss}$ direction from zero up to 50 MeV/c in 10 MeV/c steps. Blue squares differs from all other by having unphysical (much larger than the expected CM momentum) shift of 150 MeV/c in the $\vec{p}_{miss}$ direction. It is clearly seen that the effect of different shifts is negligible. Due to limited statistics we can not determine if there is any actual shift, so in this thesis we ignore the shift. The solid line corresponds to the simulation without applying the cut on the TOF distribution of neutrons (in other words, there is no cut on neutrons momenta between 300 up to 900 MeV/c) . The result is as expected, and the effect of this cut is significant only in the $p_{\rm miss}$ direction. The horizontal lines represent the actual measurement: average and $\pm\sigma$ lines.

The difference between the simulated and measured widths shows the effect of the finite solid angle of HAND. All the values for CM are summarized and plotted in Figure 4.23:

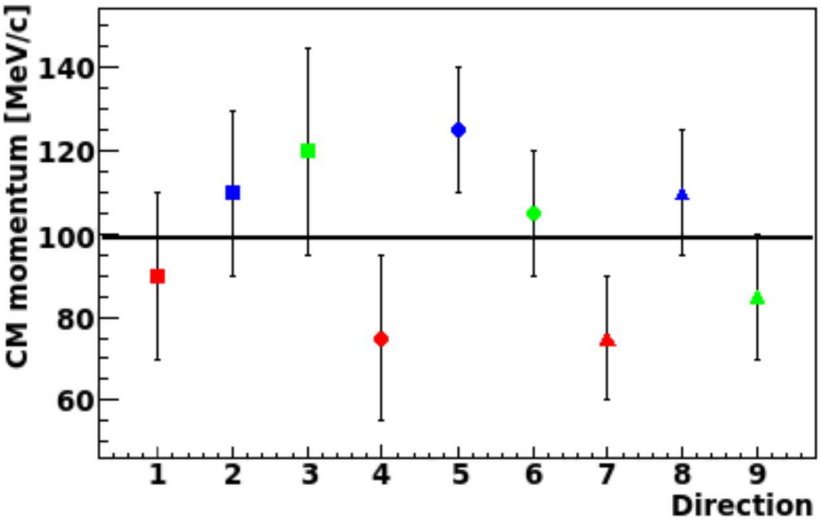


Figure 4.23: Different colors represent different spatial directions; Red points – $x$ direction. Blue points – $y$ direction. Green points – $z$ direction. Different symbols are for three kinematical setups; squares are for 500 MeV/c, circles for 625, and triangles for 750 MeV/c.

We estimate the width of the CM momentum to be the weighted average of these measurements,

which is $100 \pm 20$ MeV/c. This value is similar to the estimated by Perugia theoretical group [18].

## 4.5 Opening angle

One of the direct measures that identify the 2N-SRC is the opening angle between $\vec{p}_{\mathrm{miss}}$ and $\vec{p}_{\mathrm{rec}}$. In this analysis, the opening angle was used as a way to normalize the mixing event distributions to the data. As described in the previous sections, this normalized distribution represents the random background level. In Figure 4.24, an example of opening angle for the 625 MeV/c kinematics is shown.

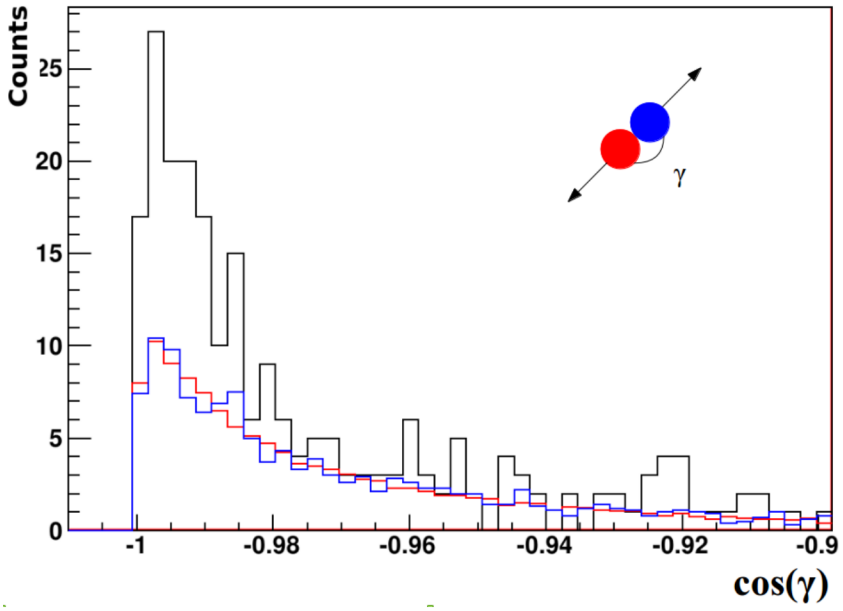


Figure 4.24: Opening angle distribution measured during the 625 MeV/c setting. Black histogram: signal and background. Blue histogram: opening angle for events in the off coincidence time region. Red: opening angle for events obtained using event mixing.

The combined opening angle distribution between neutrons and $p_{\mathrm{miss}}$ for 750 and 625 MeV/c kinematics is shown in Figure 4.25:

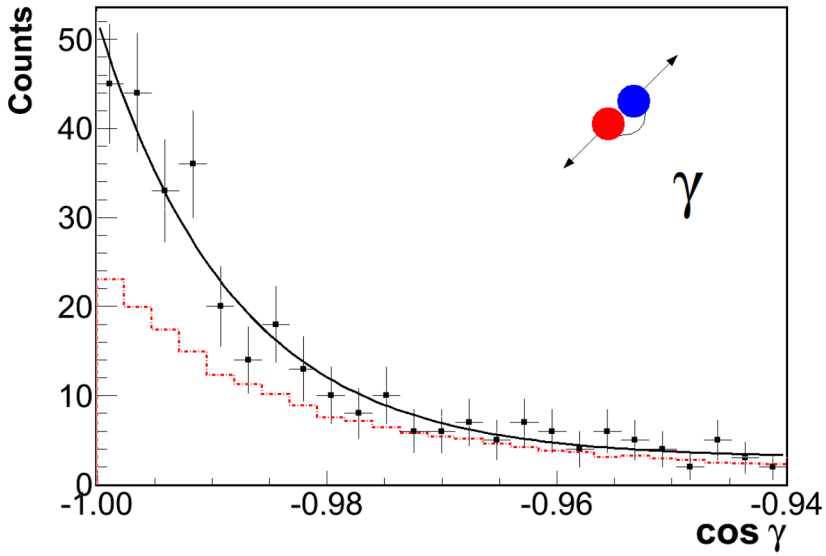


Figure 4.25: Opening angle for 625 and 750 MeV/c setups. Red line represent the random background from mixed events. Solid line is the opening angle based on the simulation with $\sigma = 100$ MeV/c in each direction with a mixture of flat random background.

## 4.6 Missing mass

The missing mass distributions also indicates the state of the residual $A-2$ system. For the $^4$He$(e,e'pn)$ reaction, the residual $A-2$ system consists of one proton and one neutron. Thus the missing mass distribution should be around the deuteron mass. The missing mass is calculated using Eq 4.5:

$$M = \sqrt{(\omega + m_{\mathrm{He}} - E_f - E_n)^2 - (\vec{q} - \vec{p}_f - \vec{p}_n)^2} \tag{4.5}$$

where $m_{\mathrm{He}}$ is the mass of the Helium target, $E_f$ ($\vec{p}_f$) and $E_n$ ($\vec{p}_n$) energy (momentum) of the knocked-out proton and recoil neutron, and $\omega$ and $\vec{q}$ are the energy and momentum transfer.

Figures 4.26, 4.27 and 4.28 show the missing mass distributions for the three kinematics:

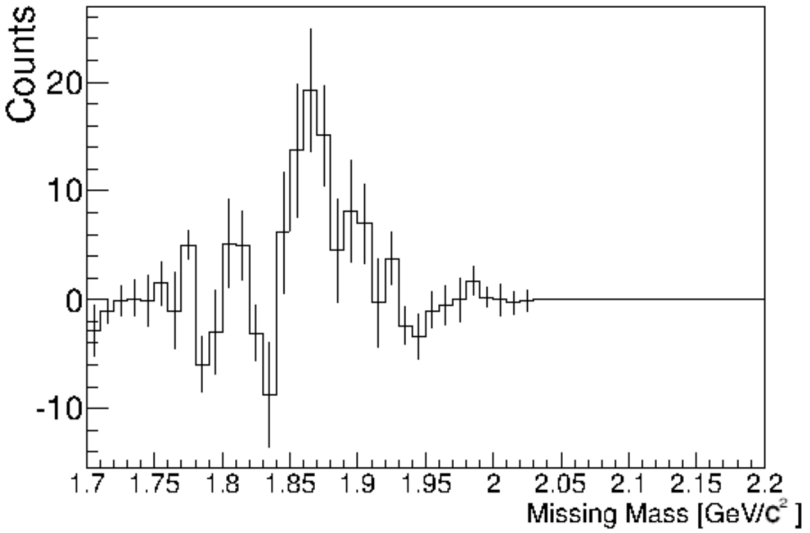


Figure 4.26: Missing mass distribution for $^4$He$(e, e'pn)$ reaction at 500 MeV/c.

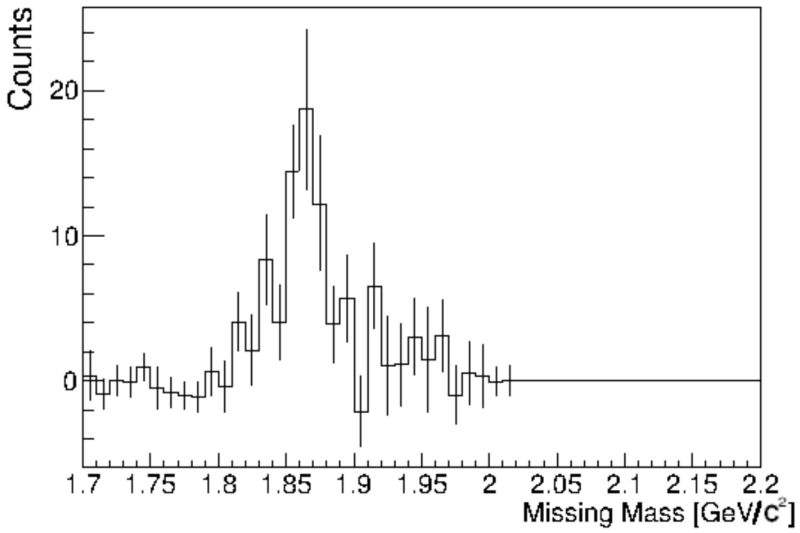


Figure 4.27: Same as Figure 4.26 for 625 MeV/c.

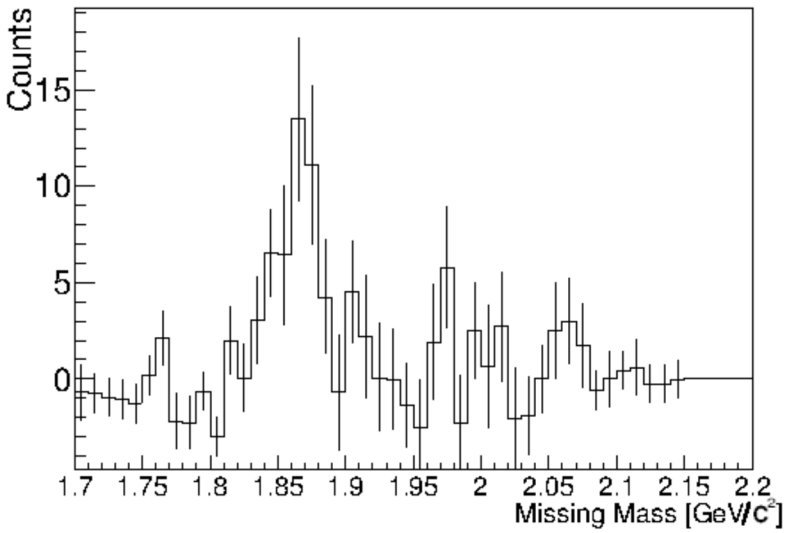


Figure 4.28: Same as Figure 4.26 for 750 MeV/c.

The missing mass distribution at 750 MeV/c has more events for $M_{miss} > 2$ GeV, correspond to $m > m_d + m_\pi$ . To reduce this contribution, we apply an additional cut on the missing mass of the $(e, e'p)$ reaction. The cut was $M_{\text{miss}} < 1$ GeV, see Figure 4.29. Although this cut does not have any affect on 500 MeV/c and 625 MeV/c kinematics, we also apply it for consistency.

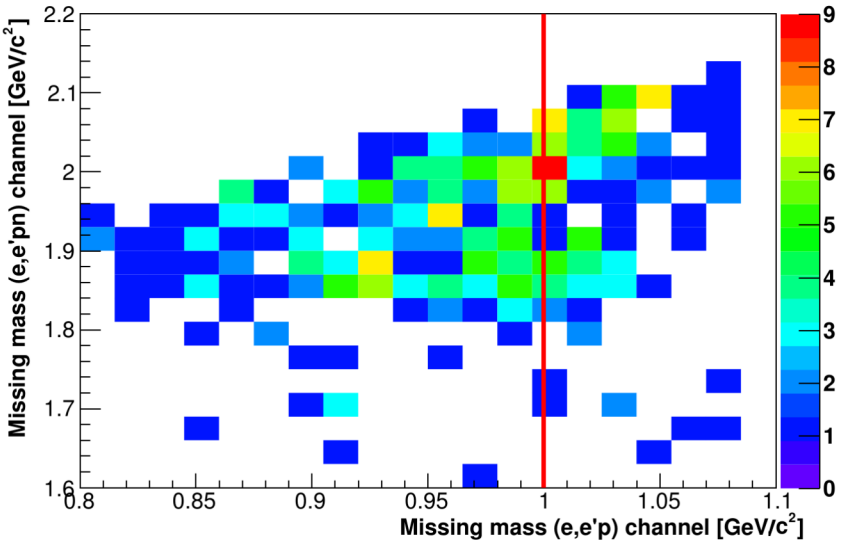


Figure 4.29: $(e, e'pn)$ missing mass versus $(e, e'p)$ missing mass for 750 MeV/c kinematics. Vertical red line represents the cut on $(e, e'p)$ missing mass in order to suppress the pion production channel in the triple coincidence events.

## 4.7 Triple coincidence events $^4$He$(e, e'pp)$

Protons in BigBite were identified by their corrected TOF spectra and comparison to an energy deposited in the trigger plane vs reconstructed momentum from MWDC. The signal in BigBite was very clean so that all detected particles after the cuts are protons, see Figure 4.30. Similar to HAND,

the number of $(e, e'pp)$ events was determined by counting the number of the events in the TOF peak. However, in BigBite case the TOF was corrected using the proton momentum and path length to improve the signal to background ratio (and as additional method for proton identification as stated above) as shown in Figure 4.31.

Cuts on in-plane and out of plane angles ($\pm 4°$, $\pm 14°$) and on the momentum from 0.3 GeV/c to 0.9 GeV/c were applied to match the acceptance of HAND. An additional cut on the retiming signal was applied (as discussed in the appendix A).

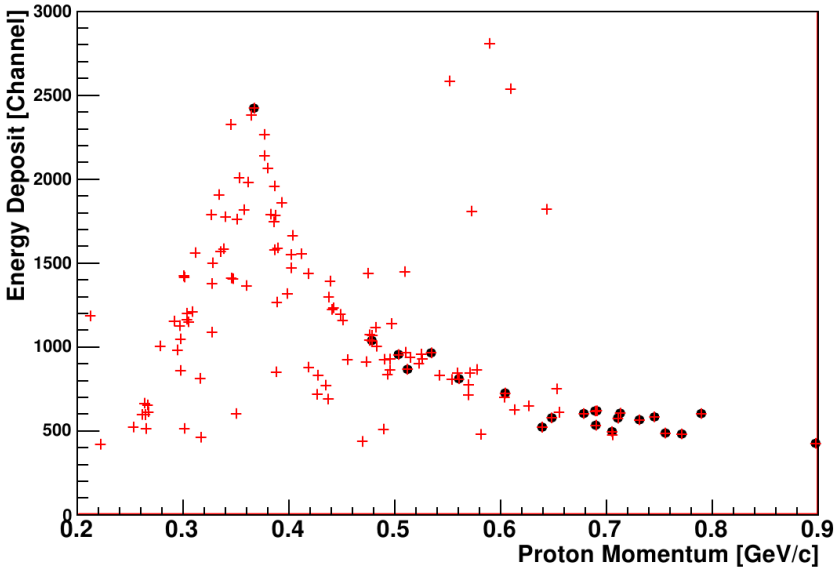


Figure 4.30: Energy deposit vs momentum in BigBite. Black circles are events that also pass the cut under the TOF peak.

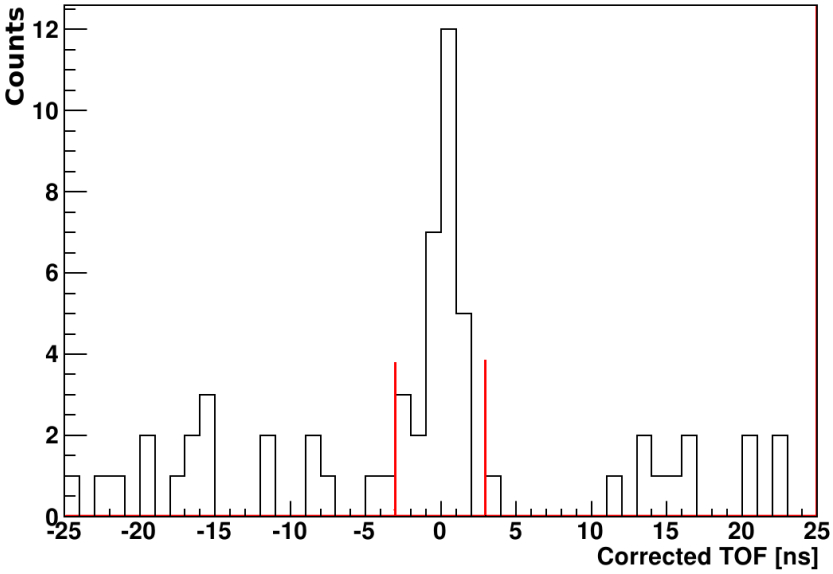


Figure 4.31: Difference between expected TOF and measured for protons in BigBite. Correction is made by assuming that the particle has a proton mass.

From the Figures 4.30 we can see that most of the background events are random protons, and the background level as seen in Figure 4.31 is small.

During the production in the first kinematics (500 MeV/c) we had timing problems that affected the data acquisition of the BigBite TDCs. This caused a loss of about half of the statistics for this $^4$He$(e,e'pp)$ setup.

| Kinematic setup | $\#(e,e'pp)$ measured | $\#(e,e'pp)$ efficiency corrected |
|---|---|---|
| 500 MeV/c | $7.5 \pm 3.2$[1] | $10 \pm 4.3$ |
| 625 MeV/c | $20 \pm 5$ | $27 \pm 6.7$ |
| 750 MeV/c | $22.5 \pm 5.2$ | $30.4 \pm 7$ |

Table 4.2: Number of triple $^4$He$(e,e'pp)$ coincidence events.

Similar to the $(e,e'pn)$ channel, for the $^4$He$(e,e'pp)$ channel we also performed the analysis of the CM motion, opening angle and missing mass distribution of the $A-2$ system. The results are consistent between these two channels. However, the low number of $^4$He$(e,e'pp)$ events limit the ability to deduce physical quantities with reasonable uncertainties. A combined missing mass spectra for the 625 and 750 MeV/c kinematics is shown in Figure 4.32.

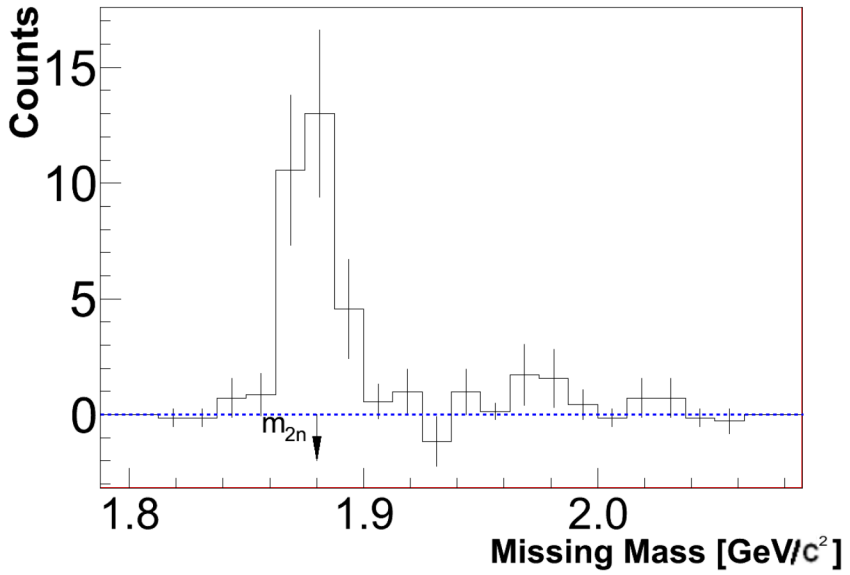


Figure 4.32: Missing mass for the $^4$He$(e,e'pp)$ reaction for $p_{\text{miss}}$ 625 and 750 MeV/c.

## 4.8 Triple to double ratios $^4$He$(e,e'pN)$ to $^4$He$(e,e'p)$

The ratio between the measured number of $^4$He$(e,e'pN)$ to $^4$He$(e,e'p)$ is modified by the finite acceptance of detectors, thus the measured ratios should be corrected by an acceptance factor. This happens because the CM of the correlated pair can be in motion in the laboratory frame, hence the knocked-out and the recoil nucleons may not be back-to-back in the laboratory, and the recoiled nucleon can miss the detector (BigBite or HAND).

The extraction of this correction factor is based on a simulation of the CM motion. We used MCEEP (Monte Carlo $(e,e'p)$) that is a simulation package developed for the Hall A spectrometers and $A(e,e'p)$ experiments [67]. The MCEEP code was modified to include a model for a moving

[1]For this kinematics only half of our data is available for BigBite due to timing issues

deuteron [53]. In addition to using MCEEP, we performed a simple simulation by taking the $^4$He$(e,e'p)$ events and simulate $^4$He$(e,e'pN)$ events with the measured CM momentum of the pair, see section 4.4. The acceptance factor equals the ratio of the number of simulated $^4$He$(e,e'pN)$ events without and with acceptance cuts for the recoil nucleon. Both simulation techniques gave the same results. The dependence of the correction factor on the $p_{\rm miss}$ is shown in Figure 4.33 and summarized in Table 4.3:

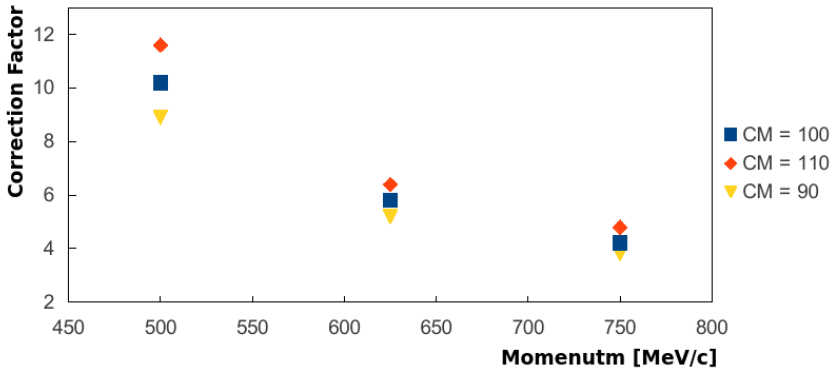


Figure 4.33: $(e,e'pN)$ to $(e,e'p)$ Correction factor as a function of $p_{\rm miss}$ [MeV/c], assuming CM momentum with widths of 90, 100 and 110 MeV/c. The correction factors are summarized in Table 4.3.

In the previous Hall A SRC experiment, E01-015, this geometrical correction factor was also extracted with MCEEP simulations for moving deuteron and moving $np$ pair in a Carbon nucleus [65]. For a known CM distribution the MCEEP simulation gives uncertainty in the geometrical correction factor of $\sim 2\%$ [65].

The geometrical correction factor is very large and strongly affects the triple to double ratios. Due to this large effect of we performed a sensitivity check by assuming 10% uncertainty on the width of the CM momentum distribution and checked its impact on the experimental uncertainties of the measured results.

| | 500 MeV/c | 625 MeV/c | 750 MeV/c |
|---|---|---|---|
| CM = 90 MeV/c | 8.9 | 5.2 | 3.8 |
| CM = 100 MeV/c | 10.2 | 5.8 | 4.3 |
| CM = 110 MeV/c | 11.6 | 6.4 | 4.8 |

Table 4.3: Acceptance correction factor for the $(e,e'pN)$ to $(e,e'p)$ ratio.

After applying the acceptance correction factor, the ratio of $^4$He$(e,e'pn)/^4$He$(e,e'p)$ is extracted from the measurements as shown in Figure 4.34 and summarized in table 4.4.

| | $\#(e,e'pn)$ | $\#(e,e'pn)$ extrapolated | $\#(e,e'pp)$ | $\#(e,e'pp)$ extrapolated | $\#(e,e'p)$ |
|---|---|---|---|---|---|
| 500 MeV/c | $107 \pm 20$ | $2728.5 \pm 510$ | $7.5 \pm 3.2$ | $102 \pm 43.9$ | $3100 \pm 56$ |
| 625 MeV/c | $66 \pm 14$ | $957 \pm 203$ | $20 \pm 5$ | $156.6 \pm 38.9$ | $1619 \pm 40$ |
| 750 MeV/c | $50 \pm 13$ | $537 \pm 140$ | $22.5 \pm 5.2$ | $130.72 \pm 30.1$ | $1228 \pm 35$ |

Table 4.4: The number of events in all measured reaction channels.

The triple to double ratios $(e,e'pn)/(e,e'p)$ and $(e,e'pp)/(e,e'p)$ are presented in table 4.5.

| | $\frac{(e,e'pn)}{(e,e'p)}$ | $\frac{(e,e'pp)}{(e,e'p)}$ |
|---|---|---|
| 500 MeV/c | $0.88 \pm 0.19$ | $0.078 \pm 0.033$ |
| 625 MeV/c | $0.59 \pm 0.15$ | $0.096 \pm 0.026$ |
| 750 MeV/c | $0.43 \pm 0.12$ | $0.106 \pm 0.028$ |

Table 4.5: The triple to double ratios. The uncertainties include statistical uncertainty and systematic uncertainty (see section 4.10).

see more detailed discussion of the experimental uncertainties in the section 4.10.

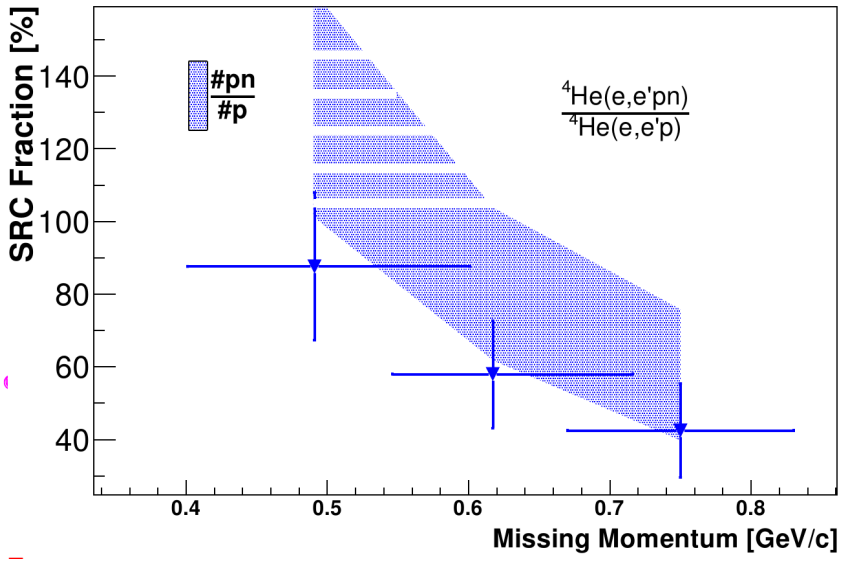


Figure 4.34: $^4$He$(e,e'pn)/^4$He$(e,e'p)$ ratio as function of missing momentum. The horizontal error bars indicate the acceptance range. The shaded area represents the ratio corrected for transparency and single charge exchange (see details on these calculations in appendix B).

Figure 4.34 shows a clear decrease in the $^4$He$(e,e'pn)/^4$He$(e,e'p)$ ratio from 500 MeV/c to 750 MeV/c. The shaded band represents the measurement corrected for single charge exchange and the transparency of the knocked-out and recoil nucleons (see appendix B). The fraction of $np$ SRC pair is decreasing, and this decrease could be due to non $2N$-SRC contributions or due to FSI.

At the 500 MeV/c kinematics the corrected SRC fraction is above 100%. This area is marked by white horizontal stripes to represent the unphysical region. The systematic uncertainties in the correction factor (15% due to finite detector acceptance, $\sim$ 20% due to FSI) and statistical fluctuations can explain the extension of the band beyond 100%.

Figure 4.35 shows the $^4$He$(e,e'pp)/^4$He$(e,e'p)$ ratio divided by a factor of two to account for possible scattering from either one of the protons in the $pp$ pair.

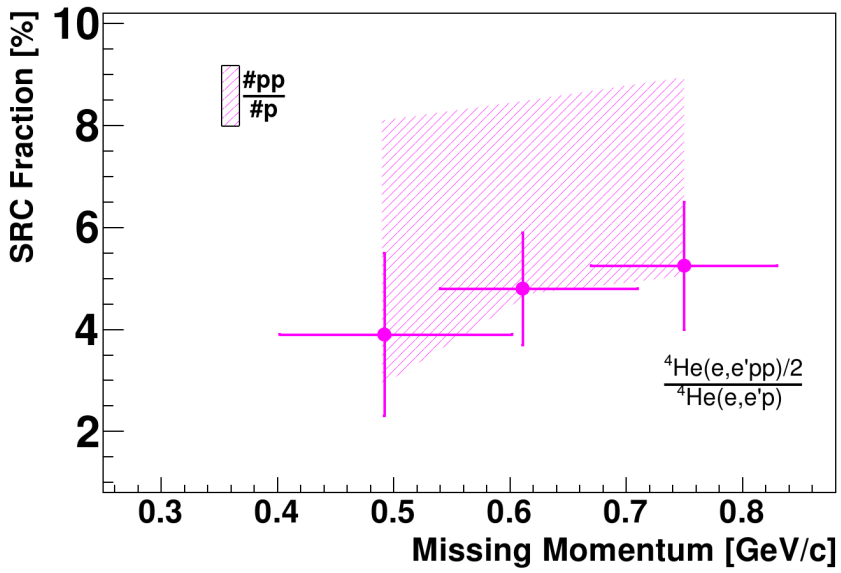


Figure 4.35: $(^4\mathrm{He}(e,e'pp)/2)/^4\mathrm{He}(e,e'p)$ ratio as function of missing momentum (see text about the factor 2). The shaded area represents the ratio corrected for transparency and single charge exchange (see calculation in appendix B).

The large uncertainties in the measured ratios are dominated by statistical uncertainties(see Table 4.6).

| | $(e,e'pn)/(e,e'p)$ | $(e,e'pp)/(e,e'p)$ |
|---|---|---|
| 500 MeV/c | 18% | 42% |
| 625 MeV/c | 21% | 24% |
| 750 MeV/c | 24% | 25% |

Table 4.6: Statistical uncertainties.

In contrast to the statistical uncertainties, most of the systematic uncertainties are small (see section 4.10), except the uncertainty coming from the acceptance correction factor ($\sim 11\%$).

## 4.9 Triple to triple ratio $^4\mathrm{He}(e,e'pp)/^4\mathrm{He}(e,e'pn)$

The triple to double ratios that are presented in the previous section have relatively large systematic uncertainties due to the large extrapolation factor that depends on the CM momentum distribution and to the effects of FSI. The measured $(^4\mathrm{He}(e,e'pp)/2)/^4\mathrm{He}(e,e'pn)$ ratios are independent of these effects (see Figure 4.36 and Table 4.7). This ratio allows direct investigation of the isospin dependence of the nucleon-nucleon pairs without the need to extrapolate the measured ratio.

| | $(^4\mathrm{He}(e,e'pp)/2)/^4\mathrm{He}(e,e'pn)$ |
|---|---|
| 500 MeV/c | $5.45 \pm 2.96$ |
| 625 MeV/c | $8.27 \pm 2.6$ |
| 750 MeV/c | $12.35 \pm 4.3$ |

Table 4.7: Summary of triple to triple ratios.

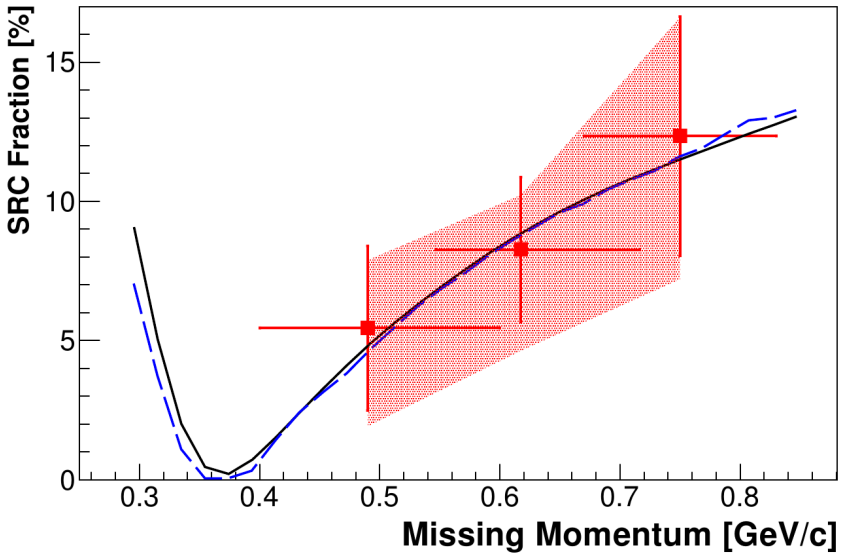


Figure 4.36: $(^4\mathrm{He}(e,e'pp)/2)/^4\mathrm{He}(e,e'pn)$ ratio as function of missing momentum (see text about the factor 2). The shaded area represents the ratio corrected for transparency and single charge exchange (appendix B). Lines represent theoretical predictions of the ratio, see text.

The measurement shows an increase in the measured ratio. The statistics of the measurement are a limiting factor but this increase is supported by the decrease of the relative abundance of the $np$ pairs from almost 100% to $\sim 50\%$. This decrease can indicate the transition between the dominance of the tensor force to the scalar repulsive part of the nucleon-nucleon force because the correlations induced by the tensor force are strongly suppressed in the case of the $pp$ pairs, which are mostly in a $^1S_0$ state.

We calculated the two nucleon knock out process assuming that the virtual photon hits the leading proton and the missing momentum equals to the relative momentum at the pair $p_{\mathrm{miss}} = k_{\mathrm{rel}}$ (PWIA).

We used a calculated ground state momentum distribution using variational Monte-Carlo wave functions derived from a realistic Hamiltonian with two- and three-nucleon potential AV18+UX [68]. As the relative momenta ($k_{\mathrm{rel}}$) increases, the tensor force becomes less dominant, the role played by the short-range repulsive force increases and with it the ratio of $pp/np$ pairs. The solid curve in Figure 4.36 was obtained using the weighted average of the calculations with CM momentum ($Q$) and arbitrary angles between the relative and CM momentum of the pair. The dashed line represents the calculation with fixed CM momentum and $Q = 0$. The weight is based on $Q$, defined in Eq. 4.6:

$$Q = \sqrt{p^2_{\mathrm{cm}_x} + p^2_{\mathrm{cm}_y} + p^2_{\mathrm{cm}_z}} \tag{4.6}$$

where the $p_{\mathrm{cm}_x}$, $p_{\mathrm{cm}_y}$ and $p_{\mathrm{cm}_z}$ are momentum in the $x$,$y$ and $z$ directions and are sampled randomly from distributions with zero mean and with $\sigma = 100 \pm 20$ MeV/c, as described in Section 4.4. We simulated the $Q$ distribution and it is shown in Figure 4.37:

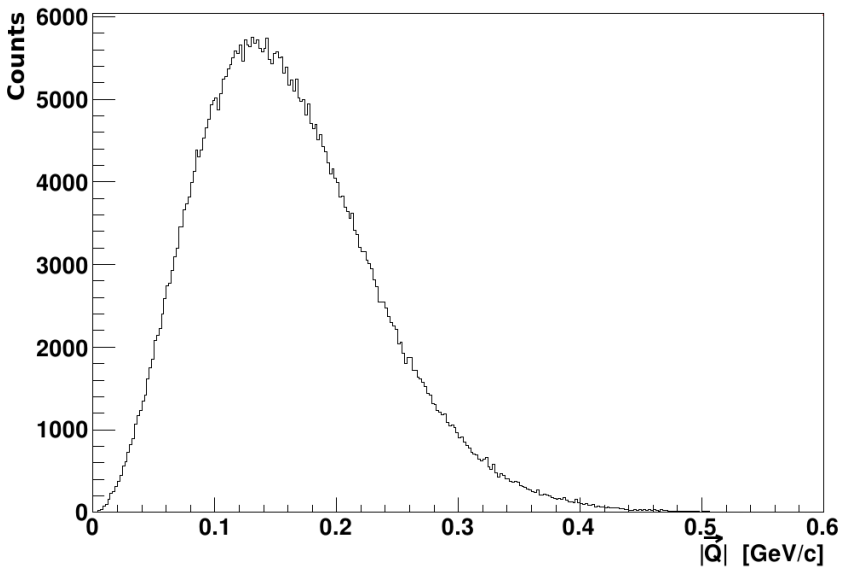


Figure 4.37: Simulated CM momentum distribution.

## 4.10 Experimental Uncertainties

In addition to the statistical uncertainties, there are different sources of systematic uncertainties that affect the results. These include uncertainties arising from acceptance corrections in the triple to double ratios, the cuts applied on the measured distributions, the theoretical constants that are used to correct the measured data, etc. In general, most of these uncertainties are relatively small with respect to the large statistical uncertainties as shown in Table 4.6. In the following we list the main sources of systematic uncertainties in the data and our estimates for their values.

The first uncertainty we discuss is the contamination of the $(e, e'p)$ events with the random background. The fraction of the random $(e, e'p)$ events depends on the width of the cut applied on the coincidence time between the two HRS spectrometers. In the first two kinematical settings, 500 and 625 MeV/c, this contamination was small, of the order of $\sim 1\%$, and for the 750 MeV/c it was $\sim 8\%$. We subtracted the number of random $(e, e'p)$ events based on the measured off time coincidence rates. We took the upper limit of $\sim 8\%$ as the systematic uncertainty due to the random background subtraction.

Second source of systematics uncertainties is due to multiple hits events. In the $(e, e'p)$ channel we had less than 0.5% of the events that had more than one hit in the s2m planes of the HRSs. Due to the smallness of the effect, this correction was ignored and added as a systematic uncertainty. In the $(e, e'pp)$ and $(e, e'pn)$ channels the contribution is larger and the correction is described in section 3.3.6 for BigBite and 3.4.5 for HAND. The uncertainty of the multi hits in BigBite and HAND were included in the efficiency error estimated ( BigBite $73 \pm 1\%$ and HAND $40 \pm 1.4\%$ ) see details in the relevant sections.

The nominal cuts (such as spatial acceptance) on the HRSs data also contributes to the systematic uncertainties. The HRS spectrometers are the principal detectors of Hall A and are well studied [52]. The uncertainties that arise from these cuts are small and similar to these in the previous SRC experiment [33]. We assumed that these cut introduce systematic uncertainties of $\sim 2\%$.

A fourth source for uncertainties is the delta contamination in the $(e, e'p)$ sample. In order to reduce the contamination from $\Delta$ excitation we applied a $\omega - y$ scaling cut. The choice of this cut,

instead of a cut $x_B > 1$ was done based on the previous study that is discussed in [33]. The sensitivity of the $\omega - y$ scaling cut was tested, see Figure 4.38. The uncertainty caused by this cut is $\sim 4\%$. In order to reduce the delta contribution further we applied cut on missing mass of the $(e, e'p)$ reaction, discussed in section 4.6. The remaining fraction of events after the missing mass cut is $\sim 1\%$ for 750 MeV/c kinematics and much less for the 500 and 625 MeV/c settings. .

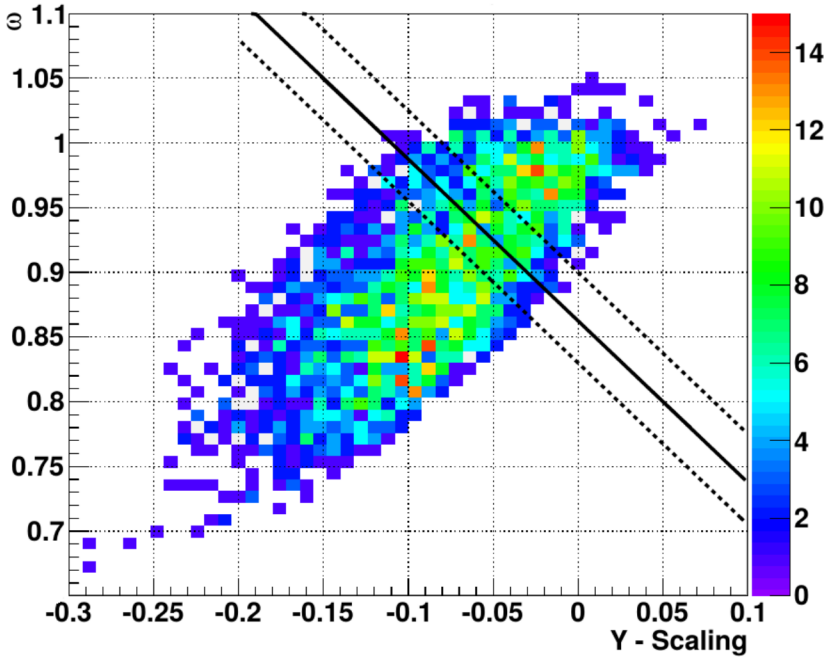


Figure 4.38: The $\omega$ versus $y$ scaling parameter cut (solid line). The dashed diagonal lines represent the sensitivity test for this cut. The data is for the 750 MeV/c kinematics.

Another uncertainty we estimated is due to quasi elastic $(e, e'p)$ events originated from scattering off the cell walls (i.e. $Al(e, e'p)$ events). The position resolution of the HRSs is good enough so that the cut that exclude the target walls eliminated almost entirely this contamination. The remaining uncertainty is $< 3\%$ as described in section 4.1.

Correction of the measured data due to inhomogeneity of the detector acceptance were applied with some uncertainties. In the case of the HRSs we used the nominal cuts which were extensively studied. The momentum range and angular cuts that were used in this experiment for BigBite spectrometer limit the events to the region were the acceptance is homogenius. Only at 500 MeV/c there was a small fraction of events that were lost as can be seen in the Figure 4.39. We estimated that this acceptance cuts introduce systematic uncertainty of 1.5%.

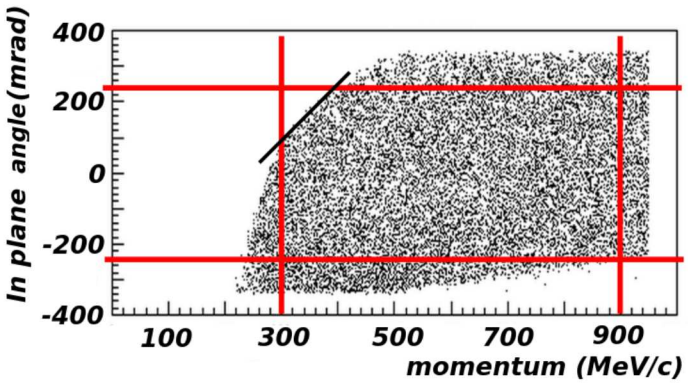


Figure 4.39: BigBite acceptance for in-plane scattering angle $\theta$ versus the momentum of the detected particle. Horizontal red lines represent the angular cuts that were used, while the vertical represent the minimum and maximum possible momentum. The missing area correspond to less than 1.5% for the 500 MeV/c settings. For 625 and 750 MeV/c kinematics we did not expect events lost from this region due to the small acceptance of the HRSs. To be conservative we estimated BB acceptance uncertainties of 1.5% for all setups.

The last and main source of the systematic uncertainty is the acceptance correction factor (relevant only for triple to double ratios). As already discussed in section 4.8, this correction is strongly affecting the extracted ratios. We estimated the correction coefficient based on the CM motion of the pair extracted from the data, see section 4.4. The correction factor is consistent with previous SRC experiment that used the same model for the CM motion [65]. From sensitivity test shown in Table 4.6 we estimate this systematic uncertainty to be $\sim 11\%$.

All the systematic uncertainties described here are summarized in Table 4.8 below.

| Quantity | Uncertainty | $\frac{(e,e'pp)}{(e,e'p)}$ | $\frac{(e,e'pn)}{(e,e'p)}$ | $\frac{(e,e'pp)}{(e,e'pn)}$ |
|---|---|---|---|---|
| Random (e,e'p) events | 8% | √ | √ | √ |
| Multi hits in HRSs | 0.5% | √ | √ | √ |
| Acceptance Cuts | 2% | √ | √ | √ |
| $\omega - y$ scaling cut | 4% | √ | √ | √ |
| Missing mass cut on $(e, e'p)$ | 1% | √ | √ | √ |
| Target walls Contamination | 3% | √ | √ | √ |
| BB acceptance | 1.5% | √ | | √ |
| Acceptance correction factor | 11% | √ | √ | |
| HAND Efficiency | 2.5% | | √ | √ |
| BigBite Efficiency | 1.4% | √ | | √ |
| **Total** | | 14.8% | 14.9% | 10.5% |

Table 4.8: Summary of the systematic uncertainties in the experiment. Total systematic uncertainty for each ratio is presented.

Based on the above discussion, we assume systematic uncertainty for triple to double ratios of 15% and 11% for triple to triple ratios.

The uncertainties for the FSI corrections such as SCX and transparency that were used in this thesis are based on private communication with Ghent group [69] and described in details in Appendix B.

# Chapter 5

# Summary and conclusion

The stability of atomic nuclei is due to a delicate interplay between the long-range attraction that binds nucleons and the short-range repulsion that prevents the collapse of the system. In between, the dominant scalar part of the nucleon-nucleon force almost vanishes and the interaction is dominated by the tensor force, which depends on the spin orientations and the relative orbital angular momentum of the nucleons.

Recent high-momentum-transfer triple-coincidence $^{12}$C$(e,e'pN)$ and $^{12}$C$(p,2pn)$ measurements [11–15] have shown that nucleons in the nuclear ground state form pairs with large relative momentum and small center-of-mass (CM) momentum. In the missing-momentum range of $300-600$ MeV/c, these pairs were found to dominate the high-momentum tails of the nuclear wave functions, with neutron-proton ($np$) pairs nearly 20 times more prevalent than proton-proton ($pp$) pairs, and by inference neutron-neutron ($nn$) pairs. This is due to the strong dominance of the $NN$ tensor interaction at the probed sub-fermi distances [50, 68, 70].

The association of the small $^{12}$C$(e,e'pp)/^{12}$C$(e,e'pn)$ ratio at $(e,e'p)$ missing momenta of $300-600$ MeV/c with dominance of the $NN$ tensor force leads naturally to the quest for increasing missing momenta. This allows the search for pairs at distances in which the nuclear force changes from being predominantly tensor to the essentially unexplored repulsive interaction. We report in this thesis on a simultaneous measurement of the $^4$He$(e,e'p)$, $^4$He$(e,e'pp)$, and $^4$He$(e,e'pn)$ reactions at $(e,e'p)$ missing momenta from 400 to 830 MeV/c. The observed changes in the isospin composition of the SRC pairs as a function of the missing momentum are presented, discussed, and compared to calculations.

The measured $\frac{^4\mathrm{He}(e,e'pN)}{^4\mathrm{He}(e,e'p)}$ ratios are given by the number of events in the background-subtracted triple-coincidence TOF peak corrected for the finite acceptance and detection efficiency of the recoiling nucleons, divided by the number of random-subtracted (double-coincidence) $^4$He$(e,e'p)$ events. These ratios, as a function of $p_{\mathrm{miss}}$ in the $^4$He$(e,e'p)$ reaction, are displayed as full symbols in the two upper panels of Figure 5.1.

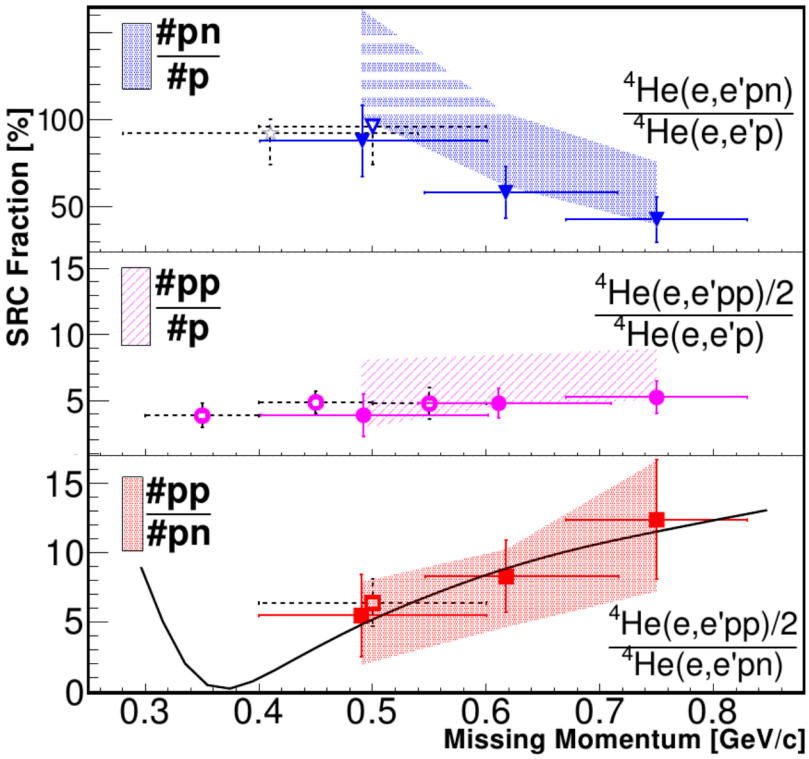


Figure 5.1: Bottom panel: The measured ratios $^4$He$(e,e'pp)/^4$He$(e,e'pn)$, shown as solid symbols, as a function of the $^4$He$(e,e'p)$ missing momentum. Each point is the result of a different setting of the detectors. The bands represent the data corrected for FSI to obtain the pair ratios, see text for details. Also shown are calculations using the momentum distribution of Ref. [68] for pairs with weighted-average CM momentum assuming arbitrary angles between the CM and the relative momenta in the pair (solid black line). The middle panel shows the measured $^4$He$(e,e'pp)/^4$He$(e,e'p)$ and extracted $\#pp/\#p$ ratios. The top panel shows the measured $^4$He$(e,e'pn)/^4$He$(e,e'p)$ and extracted $\#pn/\#p$ ratios. The unphysical region above 100% obtained due to systematic uncertainties and statistical fluctuations is marked by white strips. Ratios for $^{12}$C are shown as empty symbols with dashed bars. The empty star in the top panel is the BNL result [13] for $^{12}$C$(p,ppn)/^{12}$C$(p,pp)$.

Because the electron can scatter from either proton of a $pp$ pair (but only from the single proton of an $np$ pair), we divided the $^4$He$(e,e'pp)$ yield by two. Also displayed in Figure 5.1, as empty symbols with dashed bars, are similar ratios for $^{12}$C obtained from previous electron scattering [14, 15] and proton scattering [13] measurements. In comparing the $^{12}$C and $^4$He data, it is noted that the measured ratios are about equal and very different from the ratios of naive pair counting in these nuclei. The horizontal bars show the overlapping momentum acceptance ranges of the various kinematic settings. The vertical bars are the uncertainties, which are predominantly statistical.

Because we obtained the $^4$He$(e,e'pp)$ and $^4$He$(e,e'pn)$ data simultaneously and with the same solid angles and momentum acceptances, we also directly determined the ratio of $^4$He$(e,e'pp)$ to $^4$He$(e,e'pn)$. In this ratio, many of the systematic factors needed to compare the triple-coincidence yields cancel out, and we need to correct only for the detector efficiencies. This ratio as a function of the missing momentum is displayed in the lower panel of Figure 5.1 together with the previously measured ratio for $^{12}$C [15].

To extract from the measured cross section ratios the underlying pair ratios, corrections for final-state interactions (FSI) were calculated using the Glauber approximation [69]. The pair fraction extracted from the measured ratios with the FSI calculated corrections are shown in Figure 5.1 as

bands. The statistical and systematic uncertainties were treated as independent and combined by simulation to create the width of the one standard deviation bands shown in Figure 5.1. The systematic uncertainties in the correction factor (15% due to finite detector acceptance, $\sim 20\%$ due to FSI) and the statistical fluctuation can explain the extension of the band beyond 100%.

The correction to the ratios due to attenuation of the leading-proton is small. The attenuation of the recoiling nucleon decreases the measured triple/double coincidence ratios. Because the measured $^4$He$(e,e'pn)$ rate is about an order of magnitude larger than the $^4$He$(e,e'pp)$ rate, $^4$He$(e,e'pn)$ reactions followed by a single charge exchange (and hence detected as $^4$He$(e,e'pp)$) increase the $^4$He$(e,e'pp)/^4$He$(e,e'pn)$ and the $^4$He$(e,e'pp)/^4$He$(e,e'p)$ measured ratios.

The two-nucleon momentum distributions were calculated for the ground states of $^4$He using variational Monte-Carlo wave functions derived from a realistic Hamiltonian with Argonne V18 and Urbana X potentials [68]. The solid (black) curve in Figure 5.1 was obtained using the calculations [68] and a weighted average over arbitrary angles between $\vec{k}_{\rm rel}$ and $\vec{K}_{\rm CM}$, and the CM momentum of the pair. The calculation with $K_{\rm CM}=0$, which agrees quantitatively with the Perugia group calculation [18,71], differs little from the average shown in the figure. To compare the calculations to the data in Figure 5.1, we assumed that the virtual photon hits the leading proton and $p_{\rm miss}=k_{\rm rel}$ (Plane Wave Impulse Approximation).

The measurements reported here were motivated by the attempt to study the isospin decomposition of $2N$-SRC as a proxy to the transition from primarily tensor to the short range repulsive, presumably scalar, nucleon-nucleon force. In the ground state of $^4$He [68], the number of $pp$-SRC pairs is much smaller than $np$-SRC pairs for values of the relative nucleon momentum $k_{\rm rel}\sim 400$ MeV/c. This is because the correlations induced by the tensor force are strongly suppressed for $pp$ pairs, which are predominantly in $^1S_0$ state [50,68,70,71]. As the relative momenta increase, the tensor force becomes less dominant, the role played by the short-range repulsive force increases and with it the ratio of $pp/np$ pairs. In our measurement, as the missing momenta is increased beyond 500 MeV/c, the triple coincidence $^4$He$(e,e'pp)/^4$He$(e,e'pn)$ ratio increases, in good agreement with the prediction based on the ratio of $pp$-SRC/$np$-SRC pairs in the $^4$He ground state [68].

The measured triple/double coincidence ratios shed further light on the dynamics. The measured $^4$He$(e,e'pp)/^4$He$(e,e'p)$ ratio reflects a small contribution from $pp$-SRC pairs. These pairs are likely dominated by a scalar repulsive short-range force which is relatively constant over the reported momentum range. The $^4$He$(e,e'pn)/^4$He$(e,e'p)$ ratio clearly shows that the reduction in the $np/pp$ ratio with increasing $p_{\rm miss}$ is due to a drop in $np$-SRC pairs with increasing $k_{\rm rel}$. While $np$-pairs still dominate two nucleon SRC, even at missing momentum of 800 MeV/c, the total fraction of the $(e,e'p)$ cross section associated with scattering from $2N$-SRC pairs drops with increasing missing momentum. This is likely due to an increase of more complex mechanisms allowed by ambiguity between the recoil and knockout nucleons when their momentum difference is not large, and the possible onset of SRC involving more than two nucleons [27]. A definitive understanding of the relative importance of these effects requires exclusive measurements at large missing momentum on heavier nuclei, and a more detailed theoretical study. We hope that the new data presented in the experiment will stimulate such calculations.

One should question to what level the naive interpretation of the data in terms of the ground state nuclear properties is appropriate. Comprehensive calculations, which take into account the full reaction mechanism in a relativistic treatment, as well as additional data with better statistics will allow a more detailed determination of the role played by the elusive repulsive short-range nucleon-nucleon interaction.

# Appendix

## Appendix A: Timing/retiming problem

The electronics was set to record the timing information in a common stop mode for HRSs and HAND TDCs and in common start mode for the BigBite's TDCs. In the previous Hall A experiments, HRSs worked in common start mode using LeCroy 1875 TDCs (for s1 and s2m scintillators) with $\sim 0.1$ ns time resolution. Just before the current experiment all TDCs were changed to LeCroy1877 TDCs that are working in a common stop mode. This change was done because the following experiment needed multi hit capabilities that 1875 did not support. The drawback of this change was reduction of the time resolution to 0.5 ns.

In general, a retiming circuit is utilized in setups where drift chambers are used. The retiming circuit defines a fixed reference in time that is used in the drift chambers to calculate the drift time. The drift time in turn is translated into drift distance.

The trigger supervisor (TS) unit that controls the data taking generates the "Level 1 Accept" (L1A) that is used by all front end electronics as a common stop/start signal. The L1A is generated immediately after the arrival of first physical trigger (T1, T2, T3, T4, T5, T6). This signal is also used as a Veto signal to ignore all additional triggers during the data reading for 1.5 $\mu$sec. The arrival of the triggers to the TS can vary in time due to physical properties such as different path length and momentum of the particle (electron or proton) and this time shift affect the reference time for the drift chambers. In order to remove this jitter in time, a retiming circuit is used to cause the L1A signal to be fixed in time for each detector. For BigBite the reference time for the MWDC is generated by the E plane and for the HRSs it is defined by their s2m plane (the plane that define the time for the trigger). Figure A.1 shows the time flow of the retiming circuit for BigBite.

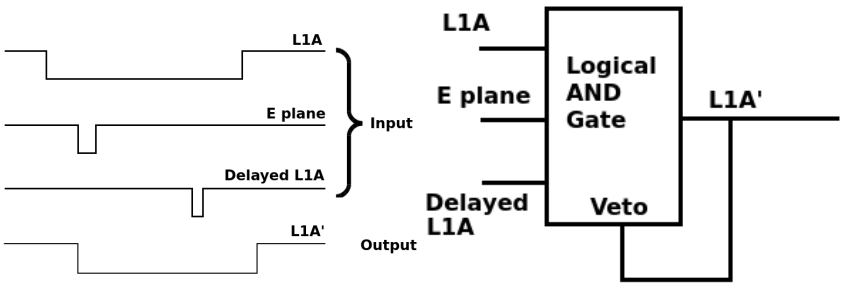


Figure A.1: Retiming circuit diagram for BigBite. The original L1A signal (top line) is retimed by the signal from the E plane bars generate retimed L1A'. If there was no signal in the E plane, the delayed L1A serves as fail safe that make the retimed L1A to be a delayed L1A (this is needed to clear the front end electronics).

The retiming circuit create two point in time were the data is not accessible, when the L1A arrive later than the retimed signal ($E$ plane in Figure A.1) or when there was no retimed signal and the coincidence is done with the delayed copy of L1A. In order to remove events from these regions we apply cut presented in Figure A.2.

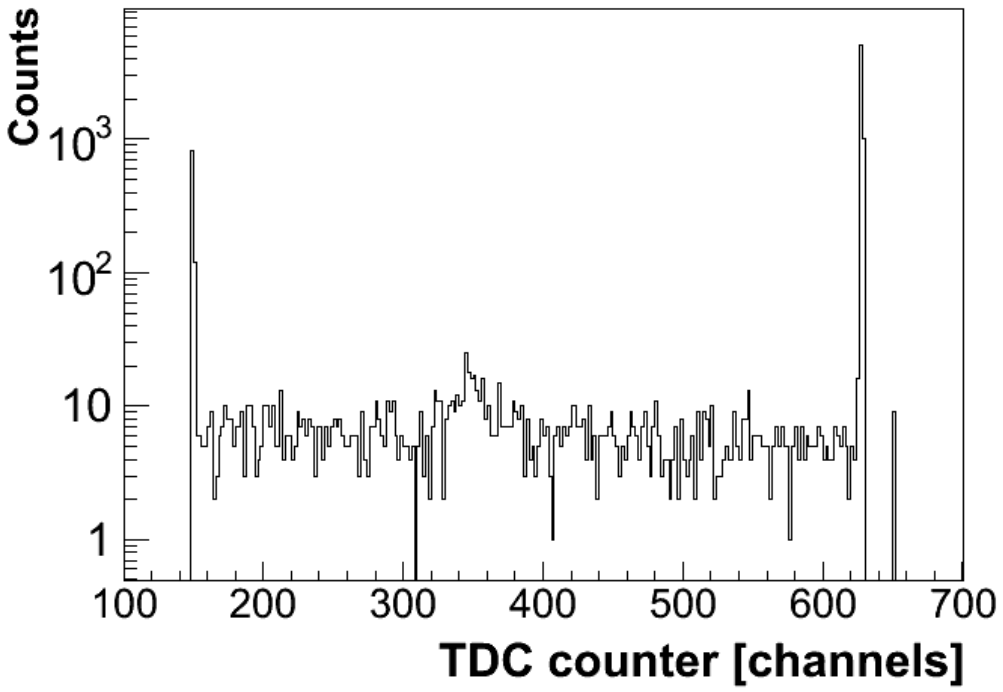


Figure A.2: Recorded retimed T3 signal (arbitrary channels). Two sharps peaks on both ends of the distribution represent cases without T3 signal (right peak) and when the retiming is done on L1A (left peak).

Similar retiming circuits were applied also to the TDCs in the other detectors. This configuration introduced ambiguities in the common stop/start signals. Actually we had 5 different derivative of the main trigger signal.

1) Common stop for the L-HRS TDCs and trigger information (located in the L-HRS hub). This signal was L1A retimed from the strobe signal, while the strobe signal is generated by logical "or" between scintillators in the s1 plane.

2) Common stop for the R-HRS TDCs and some trigger information (located in the R-HRS hub). Similar to the L-HRS but the strobe signal was from the s1 plane of the R-HRS.

3) Common stop for the HAND TDCs (located in the BigBite weldment). This was the L1A generated from the coincidence between s1 and s2m planes in L-HRS. It is actually the signal that should be used for all detectors.

4) Common stop signal in the FASTBUS crate that stores all trigger information for all detector (located in the BigBite weldment). This signal was L1A retimed from BigBite's E plane.

5) Common stop (reference signal) for BigBite's TDCs (located in the BigBite weldment). This was L1A retimed from BigBite's E plane, similar to 4.

The distortion to the timing information due to the different common stop signal is crucial, especially in the neutron case where all the physical quantities dependent on the knowledge of absolute time. The coincidence time, which determined the time difference between the L-HRS and R-HRS,

have a problem because each HRS have different stop signal. In each HRS, we looked at the time difference between the TDCs and the trigger signal that were recorded with the same common stop signal. By looking on this differences, the dependence on the trigger signal is eliminated:

$$CT_{\text{HRSs}} = (HRS_L - L1A_L) - (HRS_R - L1A_R) \tag{A.1}$$

where each group has the same common stop signal:

$$CT_{\text{HRSs}} = (s2m_L - L1A) - (s2m_R - L1A) \tag{A.2}$$

Thus the CT is the relative time between the s2m planes in the left and right HRSs. For the neutron, the TOF calculation was done in a similar manner. The common stop signal in HAND is $L1A$:

$$N_{\text{TOF}} = (HRS_L - L1A_L) - (HAND - L1A) = (s2m_L - L1A) - (HAND - L1A) \tag{A.3}$$

In the BigBite case the problem is more complicated. We had two major problems in BigBite:

1) The timing during the elastic measurements was different from the production runs. During the elastic runs, the common stop signal was identical to the "$L1A$" and during the production it was retimed from the $E$ plane. So, the standard time difference between the BigBite and the L-HRS time does not reproduce the actual TOF. This was solved by using the appropriate combination of various signals.

$TDC_{\text{BB}} = TDC_E - L1A'$: Time information from the BigBite E plane. The start signal $L1A'$ is the retimed $L1A$ signal by the $E$ plane.

$TDC_{\text{HRS}} = L1A'' - s2m$: Time information from L-HRS. It is defined by the s2m plane and retimed by the s1 plane (retiming cause modification of $L1A$ to $L1A''$).

$TDC_{L1A-L} = L1A'' - L1A$: Trigger time information recorded in the L-HRS FASTBUS unit having the common stop signal retimed by the s1 plane (s1 plane of L-HRS).

$TDC_{L1A} = L1A' - L1A$: Trigger time information recorded in the BigBite VME unit having common stop retimed by the $E$ plane. Combination of these timing information eliminate the dependence on the retimed stop/start signals and produce the desired time difference between the E plane and the s2m plane in L-HRS.

$$TDC_E - TDC_{s2m} = TDC_{\text{BB}} + TDC_{\text{LHRS}} + TDC_{L1A} - TDC_{L1A-L} \tag{A.4}$$

2) During the first kinematics (500 MeV/c), half of the data for BigBite was not used because of a wrong settings of the retiming circuit. This data lost in the 500 MeV/c settings is the reason for the relatively large statistical uncertainties of the $(e, e'pp)$ channel.

## Appendix B: Correction for the SCX/Transparency

The measured ratio's reflect the ratio of SRC pairs in the nuclear ground state but is also influenced by FSI (transparency and single charge exchange). Each nucleon that emerges from the scattering process can be absorbed or change its isospin due to an additional scattering. From Ref. [69] we extracted the transparency for the knocked-out and recoil nucleons for our kinematics:

| | TL (leading) | TR (recoil) |
|---|---|---|
| 500 MeV/c | 0.75 | 0.66 |
| 625 MeV/c | 0.752 | 0.7 |
| 750 MeV/c | 0.756 | 0.734 |

Table B.1: Transparency values

Following transparency, the probability for the SCX reaction was estimated. The rough estimate is based on Carbon data. The charge exchange cross section as measured in Ref. [72] is $\sigma = 1.1$ mb and for the Carbon case the probability for SCX is $\approx 2\%$. This probability is scaled for the $^4He$ case using the ratio between the number of nucleons: $\left(\frac{4}{12}\right)^{1/3} \cdot 2 = 1.5\%$ . due to the crude estimate of this probability, we assumed 100% uncertainty for its value. Having the transparency and SCX probability the ground state isospin ratios of $\frac{np}{pp}$ can be calculated from the measured cross section ratio: $R = \frac{^4\mathrm{He}(e,e'pn)}{^4\mathrm{He}(e,e'pp)}$ by solving the following equation:

$$R \equiv \frac{^4\mathrm{He}(e,e'pp)}{^4\mathrm{He}(e,e'pn)} = \frac{2 \cdot pp\sigma_{ep} \cdot T_L \cdot T_R + np\sigma_{en} \cdot P_{\mathrm{SCX}} \cdot T_R}{np\sigma_{ep} \cdot T_L \cdot T_R + 2 \cdot nn\sigma_{en} \cdot P_{\mathrm{SCX}} \cdot T_R)} = \frac{2 \cdot T_L + \frac{np}{pp} \cdot P_{\mathrm{SCX}} \cdot \frac{\sigma_{en}}{\sigma_{ep}}}{\frac{np}{pp} \cdot T_L + 2 \cdot \frac{nn}{pp} \cdot P_{\mathrm{SCX}} \cdot \frac{\sigma_{en}}{\sigma_{ep}}} \tag{B.1}$$

Assuming for the symmetric $^4$He nuclei $\frac{nn}{pp} = 1$,

$$\frac{np}{pp} = \frac{2 \cdot T_L - 2 \cdot P_{\mathrm{SCX}} \cdot \frac{\sigma_{en}}{\sigma_{ep}} \cdot R}{T_L \cdot R - P_{\mathrm{SCX}} \cdot \frac{\sigma_{en}}{\sigma_{ep}}} \tag{B.2}$$

The ratio for electron elastic cross section on proton and neutron, ($\sigma_{en}$ and $\sigma_{ep}$ ) were extracted from Ref. [73] and the value $\frac{\sigma_{en}}{\sigma_{ep}} = 0.37 \pm 0.012$ , for their ratio was used.

We assume uncertainties on transparency of 20% and on SCX of 100% and tested how the ratio varies:

| | Measured $(e,e'pn)/(e,e'pp)$ | $P_{\mathrm{SCX}} = 1.5\%$ | $P_{\mathrm{SCX}} = 2.5\%$ | $P_{\mathrm{SCX}} = 3\%$ |
|---|---|---|---|---|
| 500 MeV/c | $18.3 \pm 10$ | 19.7 | 20.7 | 21.2 |
| 625 MeV/c | $12.1 \pm 3.8$ | 12.6 | 13.0 | 13.2 |
| 750 MeV/c | $8.1 \pm 2.9$ | 8.4 | 8.6 | 8.7 |

Table B.2: The $\#np/\#pp$ ratios. Measured and corrected

From the table above we conclude that there is only weak dependence on $P_{SCX}$.

For the triple to double ratio's we need to solve the two following equations simultaneously:

$$R_1 = \frac{^4\mathrm{He}(e,e'pn)}{^4\mathrm{He}(e,e'p)} = \frac{np \cdot \sigma_{ep} \cdot T_R \cdot T_L + 2 \cdot pp \cdot \sigma_{en} \cdot P_{\mathrm{SCX}} \cdot T_L \cdot T_R}{p \cdot \sigma_{ep} \cdot T_L} = \frac{np \cdot T_R + 2 \cdot pp \cdot \frac{\sigma_{en}}{\sigma_{ep}} \cdot P_{\mathrm{SCX}} \cdot T_R}{p} \tag{B.3}$$

$$R_2 = \frac{^4\mathrm{He}(e,e'pp)}{^4\mathrm{He}(e,e'p)} = \frac{2 \cdot pp \cdot \sigma_{ep} \cdot T_R \cdot T_L + np \cdot \sigma_{en} \cdot P_{\mathrm{SCX}} \cdot T_L \cdot T_R}{p \cdot \sigma_{ep} \cdot T_L} = \frac{2 \cdot pp \cdot T_R + np \cdot \frac{\sigma_{en}}{\sigma_{ep}} \cdot P_{\mathrm{SCX}} \cdot T_R}{p} \tag{B.4}$$

Solution for these two equations give us the actual ratios:

$$\frac{pp}{p} = \frac{R_1 \cdot \frac{\sigma_{en}}{\sigma_{ep}} \cdot P_{\mathrm{SCX}} \cdot T_R - R_2 \cdot T_R}{2 \cdot \left(\frac{\sigma_{en}}{\sigma_{ep}} \cdot P_{\mathrm{SCX}} \cdot T_R\right)^2 - 2 \cdot T_R^2} \tag{B.5}$$

$$\frac{pn}{p} = \frac{R_2 - 2 \cdot \frac{pp}{p} \cdot T_R}{\left(\frac{\sigma_{en}}{\sigma_{ep}} \cdot P_{\mathrm{SCX}} \cdot T_R\right)} \tag{B.6}$$

where $R1$ and $R2$ are the measured ratios.

To solve these equations, we applied the same assumptions as for the ratios extraction discussed before. The results are presented in tables B.3 and B.4.

| | Measured $(e,e'pn)/(e,e'p)$ | $P_{\mathrm{SCX}} = 1.5\%$ | $P_{\mathrm{SCX}} = 2.5\%$ | $P_{\mathrm{SCX}} = 3\%$ |
|---|---|---|---|---|
| 500 MeV/c | $87.6 \pm 15.5$ | 132.7 | 132.6 | 132.6 |
| 625 MeV/c | $58 \pm 12$ | 82.8 | 82.7 | 82.7 |
| 750 MeV/c | $38.9 \pm 9.5$ | 57.8 | 57.9 | 57.8 |

Table B.3: $\#np/\#p$ $(p > p_{miss})$ Values in [%]

| | Measured $(e,e'pp)/(e,e'p)$ | $P_{\mathrm{SCX}} = 1.5\%$ | $P_{\mathrm{SCX}} = 2.5\%$ | $P_{\mathrm{SCX}} = 3\%$ |
|---|---|---|---|---|
| 500 MeV/c | $3.9 \pm 1.6$ | 5.5 | 5.3 | 5.2 |
| 625 MeV/c | $4.8 \pm 1.1$ | 6.6 | 6.5 | 6.4 |
| 750 MeV/c | $4.8 \pm 1.2$ | 6.9 | 6.9 | 6.8 |

Table B.4: $\#pp/\#p$ $(p > p_{\mathrm{miss}})$ Values in [%]

Taking into account the statistical uncertainties and the uncertainties for the FSI as stated above, we simulated the uncertainties for the corrected ratios, shown in Figures B.1 and B.2.

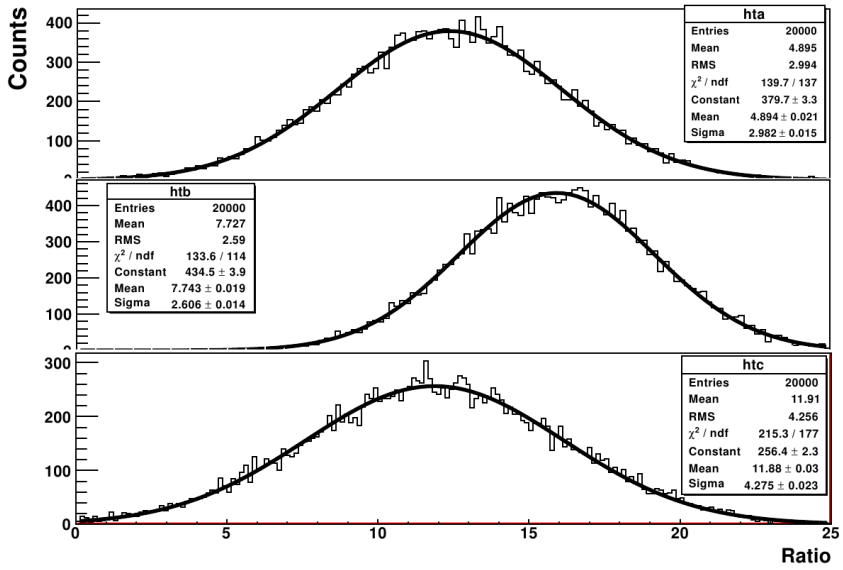


Figure B.1: Corrected ratios for $(e,e'pp)/(e,e'pn)$. From top to bottom: 500, 625 and 750 MeV/c settings.

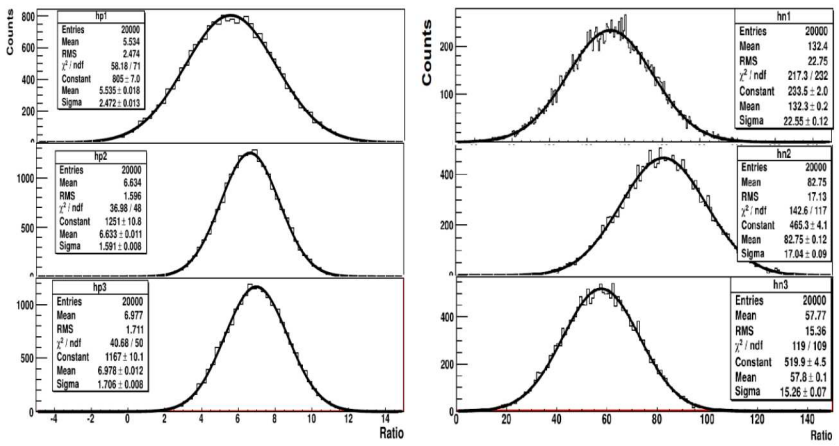


Figure B.2: Corrected ratios for $(e, e'pp)/(e, e'p)$ on the left side and $(e, e'pn)/(e, e'p)$ on the right. From top to bottom: 500, 625 and 750 MeV/c settings.

# Bibliography


[1] J. Chadwick, "The Existence of a Neutron", *Proc. R. Soc. Lond.* **A136** (1932).

[2] G. Mayer, *Phys. Rev.* **74**, 235 (1948).

[3] L. Lapikas, *Nucl. Phys.* **A553** 297c (1993).

[4] R.D. Amado, *Phys. Rev.* **C19**, 1473 (1979).

[5] L.L. Frankfurt, M.I. Strikman, D.B. Day, M. Sargsyan, *Phys. Rev.* **C48**, 2451 (1993).

[6] K.S. Egiyan *et al.*, *Phys. Rev.* **C68**, 014313 (2003).

[7] K.S. Egiyan *et al.*, *Phys. Rev. Lett.* **96**, 082501 (2006).

[8] N. Fomin *et al.*, *Phys. Rev. Lett.* **108**, 092502 (2012).

[9] F. Benmokhtar *et al.*, *Phys. Rev. Lett.* **94**, 082305 (2005).

[10] M.M. Rvachev *et al.*, *Phys. Rev. Lett.* **94**, 192302 (2005).

[11] A. Tang *et al.*, *Phys. Rev. Lett.* **90**, 042301 (2003).

[12] J. Aclander *et al.*, *Phys. Lett.* **B453**, 211 (1999).

[13] E. Piasetzky, M. Sargsian, L. Frankfurt, M. Strikman, and J. W. Watson, *Phys. Rev. Lett.* **97**, 162504 (2006).

[14] R. Shneor *et al.*, *Phys. Rev. Lett.* **99**, 072501 (2007).

[15] R. Subedi *et al.*, *Science* **320**, 1476 (2008).

[16] H. Baghdasaryan *et al.*, *Phys.Rev.Lett.* **105**, 222501 (2010).

[17] T. Hamada and I. D. Johnston, *Nucl. Phys.* **34**, 382 (1962).

[18] C. Ciofi degli Atti, S. Simula, *Phys. Rev.* **C53**, 1689 (1996).

[19] L.L. Frankfurt, M.M. Sargsyan, M.I. Strikman, *Phys. Rev.* **C56**, 1124 (1997).

[20] O. Hen *et al.*, *Phys. Lett.* **B722**, 63 (2013).

[21] J.L. Friedes, *Phys. Rev. Lett.* **15**, 38 (1965).

[22] K.I. Blomqvist *et al.*, *Phys. Lett.* **B421**, 71 (1998).

[23] D.L. Groep *et al.*, *Phys. Rev.* **C63**, 014005 (2001).

[24] M. Sargsian, *Int. J. Mod. Phys.* **E10**, 405 (2001).

[25] P. Stoler, *Phys. Rept.* **226**, 103 (1993).

[26] M. Ungaro *et al.*, *Phys. Rev. Lett.* **97**, 112003 (2006).

[27] L. Frankfurt, M. Strikman, *Phys. Rep.* **76**, 215 (1981).

[28] D.B. Day *et al.*, *Phys. Rev. Lett.* **59**, 427 (1987).

[29] M.V. Zverev, Eli E. Saperstein, *Yad Fiz* **43**, 304 (1986).

[30] C. Ciofi degli Atti, E. Pace, and G. Salme, *Phys. Lett.* **C41**, R2474 (1990).

[31] S. Janssen *et al.*, *Nucl. Phys.* **A672**, 285 (2000).

[32] T. de Forest Jr., *Nucl. Phys.* **A392**, 232 (1983).

[33] P. Monaghan, Ph.D. Thesis, Massachusetts Institute of Technology (2008).

[34] H. Morita and T. Suzuki, *Prog. Theor. Phys.* **86**, 671 (1991).

[35] C. Ciofi degli Atti, E. Pace, and G. Salme, *Phys. Lett.* **B141**, 14 (1984).

[36] Y. Akaishi, *Nucl. Phys.* **A416**, 409c (1984); H. Morita, Y. Akaishi, and H. Tanaka, *Prog. Theor. Phys.* **79**, 863 (1988).

[37] S. Fantoni and V.R. Pandharipande, *Nucl. Phys.* **A427**, 473 (1984).

[38] J.M. Laget, *Few-Body Syst., Suppl.* **15**, 171 (2003); J.M. Laget, *Phys. Lett.* **B609**, 49 (2005).

[39] C.J.G. Onderwater *et al.*, *Phys. Rev. Lett.* **78**, 4893 (1997).

[40] L.J.H.M. Kester *et al.*, *Phys. Rev. Lett.* **74**, 1712 (1995).

[41] C.J.G. Onderwater *et al.*, *Phys. Rev. Lett.* **81**, 2213 (1998).

[42] A. Zondervan *et al.*, *Nucl. Phys.* **A587**, 697 (1995).

[43] D.L. Groep *et al.*, *Phys. Rev. Lett.* **83**, 5443 (1999).

[44] D.L. Groep *et al.*, *Phys. Rev.* **C63** (2001).

[45] K.I Blomqvist *et al.*, *Phys. Lett.* **B424**, 71 (1998).

[46] G. Rosner, *Prog. Nucl. Phys.* **44**, 99 (2000).

[47] J. Arends *et al.*, *Z. Physik* **A298**, 103 (1980).

[48] M. Kanazawa *et al.*, *Phys Rev.* **C35**, 1828 (1987).

[49] J. Golak *et al.*, *Phys. Rev.* **C51**, 1638 (1995).

[50] R. Schiavilla, R.B. Wiringa, S.C. Peiper, J. Carson, *Phys. Rev. Lett.* **98**, 132501 (2007).

[51] M. M. Sargsian, T. V. Abrahamyan, M. I. Strikman, and L. L. Frankfurt, *Phys. Rev.* **C71** , 044615(2005).

[52] J. Alcorn *et al.*, *Nucl. Instrum. Meth.* **A522**, 294 (2004).

[53] R. Shneor, Ph.D. Thesis, Tel Aviv University(2007).

[54] M. Mihovilovic *et al.*, *Nucl. Instrum. Meth.* **A686**, 20 (2012).

[55] R.W. Chan, Construction and Characterization of MWDC, M.Sc. Thesis (2002).

[56] https://coda.jlab.org/wiki/index.php/Main_Page

[57] http://root.cern.ch/drupal/

[58] http://hallaweb.jlab.org/podd/doc/index.html

[59] http://teledynelecroy.com/lrs/dsheets/1877.htm

[60] http://www.caen.it/csite/CaenProd.jsp?parent=11&idmod=785

[61] http://teledynelecroy.com/lrs/dsheets/1881m.htm

[62] J. Czirr, D.R. Nygren and C.D. Zafiratos, *Nucl. Instr. and Meth.* **31**, 226 (1964).

[63] E.S. Smith *et al., Nucl. Instr. And Meth.* **A432**, 265 (1999).

[64] G.F. Knoll, Radiation Detection and Measurement, John Wiley &Sons, Inc. 3rd. ed. (2000).

[65] R. Subedi, Ph.D. Thesis, Kent State University (2007).

[66] R.A. Cecil, B.D. Anderson, R. Madey, *Nucl. Instr. And Meth.* **161**, 439 (1979).

[67] P.E. Ulmer, MCEEP: Monte Carlo for electron-nuclear coincidence experiments, http://hallaweb.jlab.org/publications/Technotes/technote.html (1991).

[68] R.B. Wiringa, R. Schiavilla, S.C. Pieper, J. Carlson, *Phys. Rev.* **C89**, 024305 (2014).

[69] J.Ryckebusch *et al.*, *Nucl. Phys.* **A728**, 226 (2003); W. Cosyn, M.C. Martinez, J. Ryckebusch, *Phys. Rev.* **C77**, 034602 (2008), and W. Cosyn and J. Ryckebusch, private communication.

[70] R.B. Wiringa, R. Schiavilla, S.C. Pieper, J. Carlson, *Phys. Rev.* **C78**, 021001 (2008).

[71] C. Ciofi degli Atti, H. Morita, private communication.

[72] S. Rock *et al.*, *Phys. Rev. Lett.* **49**, 1139 (1982).

[73] SLAC-PUB-5239, November 1991.

[74] I. Korover *et al.*, *Phys. Rev. Lett.* **113**, 022501 (2014).

[75] L. Frankfurt, M. Sargsian and M. Strikman, *Int. J. Mod. Phys.* **A23**, 2991 (2008).

[76] F. Cavanna, O. Palamara, R. Schiavilla, M. Soderberg, R.B. Wiringa, arXiv:1501.01983 [nucl-ex] (2015).

# תקציר


הבנה בסיסית של כוחות הגרעיניים ובמיוחד אינטרקציות בין הנוקלאונים, מציבה אתגר בפני הפיזיקה המודרנית. למרות ההשקעה המחקרית הרבה שניתנה לנושא במהלך המאה ה-20 ומאה ה-21 עדיין קיימות שאלות פתוחות רבות. חישובים בסיסים מודרנים כמו Lattice QCD עדיין רחוקים משיחזור של התוצאות הניסיוניות. אחת השאלות הפתוחות היא ההתנהגות של הכוחות בין הנוקלאונים במרחקים קצרים מרדיוס הנוקלאון. הידע הניסיוני בנושא מוגבל וכמותו ההבנה התאורתית.

זוגות נוקלאונים צמודים במצב יסוד הגרעיני מאופינים על ידי תנע יחסי גבוה בין הנוקלאונים ותנע מרכז מסה נמוך של הזוג (גבוה ונמוך ביחס לתנע פרמי של הגרעין). בניסוים שבהם תנע היחסי של הנוקלאונים הוא בין MeV/c 600 – 300 נמדדו כ 20 יותר זוגות ניוטרון – פרוטון מזוגות פרוטון – פרוטון (וזוגות ניוטרון – ניוטרון). הסיבה היא המרכיב הטנזורי של האינטרקציה בין הנוקלאונים, שבתנע הנמדד הוא הרכיב הדומיננטי. הקשר בין התכונות של הכח הגרעיני לבין ההרכב האיזוספיני של הזוגות הצמודים בגרעין פותח אפשרות ללמוד על הכח הדוחה בין הנוקלאונים ע"י הגדלת התנע היחסי בניסוי.

תיזה הזאת מתארת מדידות בו זמניות של תהליכי פיזור: $^4\mathrm{He}(e,e'pp)$ , $^4\mathrm{He}(e,e'pn)$ ו $^4\mathrm{He}(e,e'p)$ ב $x_B>1$ ו $Q^2\approx 2\ (\mathrm{GeV}/c)^2$ . $Q^2$ הוא האורך של ה 4-וקטור שמתאר את מעבר התנע והאנרגיה בתהליך. $x_B=\frac{Q^2}{2\mathrm{m}\,\omega}$ הוא היחס בין $Q^2$ לפעמיים מסת הנוקלאון ומעבר האנרגיה בתהליך ( $\omega$ ). המדידות בוצעו כאשר תנע החסר בתהליך $^4\mathrm{He}(e,e'p)$ היה בין 400 MeV/c ל 830 MeV/c.

הניסוי בוצע במאיץ האלקטרונים במעבדה הלאומית ע"ש זפרסון בארה"ב. הפצצנו גרעיני הליום עם אלקטרונים באנרגיה של כ $4\,\mathrm{GeV}$ . הניסוי תוכנן לזהות זוגות של פרוטון-פרוטון ופרוטון - ניוטרון קרובים ולקבוע את שכיחותם. האלקטרונים הפוגעים שלפו פרוטון מגרעין ההליום ופרוטון זה נמדד בהתלכדות עם האלקטרון המפוזר ונוקלאון נוסף שרתע בערך בכוון הפוך לכוון התנע החסר (במידה והיה כזה). המדידה רגישה לתחום בו הכוח בין הנוקלאונים משתנה מכוח טנזורי לכוח קצר טווח סקלארי ודוחה. הנתונים שהתקבלו בניסוי משווים בתיזה לחישובים של התפלגויות תנע במצב היסוד של הליום ונדון הקשר לכוח הדוחה בין נוקלאונים שכנים.

TEL AVIV UNIVERSITY
אוניברסיטת תל-אביב
RAYMOND AND BEVERLY SACKLER
FACULTY OF EXACT SCIENCES
SCHOOL OF PHYSICS & ASTRONOMY
הפקולטה למדעים מדוייקים
ע"ש ריימונד ובברלי סאקלר
בית הספר לפיסיקה ואסטרונומיה

# חקר זוגות נוקלאונים צמודים בגרעין באמצעות מדידת התהליכים

$^4\mathbf{He}\left(e,e'pp\right)$ ו- $^4\mathbf{He}\left(e,e'pn\right)$

חיבור זה הוגש כחלק מן הדרישות

לשם התואר "דוקטור לפילוסופיה"

על ידי

איגור קורובר

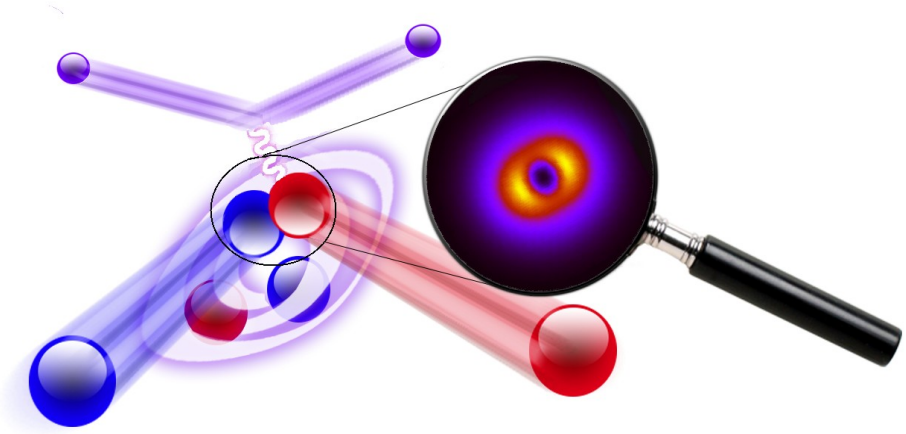

המחקר נערך תחת הנחייתו של

פרופסור אלי פיסצקי

הוגש לסנאט של אוניברסיטת תל אביב

ניסן תשע"ה